

UNIVERSITA' DEGLI STUDI DI NAPOLI  
"FEDERICO II"



DOTTORATO DI RICERCA  
In  
TECNOLOGIE INNOVATIVE PER MATERIALI  
SENSORI E IMAGING

XVIII CICLO

FIELD-EFFECT EXPERIMENTS ON OXIDE  
SUPERCONDUCTING THIN FILMS

**Coordinatore**  
Prof. Ruggero Vaglio

**Candidato**  
Antonio Prigiobbo



# Contents

Introduction.....	6
-------------------	---

## Chapter 1

### Oxides Electronics and Field-effect doping

1.1 Oxides Electronics and Correlated-Electron Technology .....	9
1.2 Perovskite oxides properties.....	11
1.3 Doping effect on perovskite-oxides properties: phase diagram.....	15
1.4 Field effect doping .....	17
1.5 Field effect experiments on High-Temperature Superconductors .....	22
1.6 Hall effect.....	25

## Chapter 2

### Materials

2.1 Strontium Titanate.....	28
2.1.1 Insulating state and dielectric properties.....	28
2.1.2 Doped and reduced STO: metallic and superconducting behaviour.....	31
2.2 $\text{Nd}_{1.2}\text{Ba}_{1.8}\text{Cu}_3\text{O}_7$ .....	38
2.2.1 High Temperature Superconductors phase diagram and Metal Insulator Transition .....	38
2.2.2 $\text{Nd}_{1.2}\text{Ba}_{1.8}\text{Cu}_3\text{O}_7$ thin films: structural and transport properties.....	43

## Chapter 3

### Field Effect on reduced STO surfaces

3.1 Experimental apparatus in Geneva .....	49
3.1.1 Hall effect measurements system .....	49
3.1.2... Dielectric and field effect measurements equipment .....	52
3.2 Hydrogen Plasma reduction.....	53
3.3 Device .....	55
3.4 Characterization .....	57
3.4.1 $R(T)$ .....	58

3.4.2	Magnetic measurements: Hall effect and magnetoresistance.....	59
3.4.3	Magnetoresistance .....	60
3.4.4	Hall effect.....	62
3.4.5	Mobility and thickness .....	64
3.5	Field effect measurements.....	69
3.5.1	Capacitance vs. Applied field.....	69
3.5.2	R (T) vs. $V_g$ .....	70
3.5.3	R vs. $V_g$ at low temperatures.....	72
3.6	Hall effect and field effect .....	74

## **Chapter 4**

### **Field-effect experiments on NdBCO thin films**

4.1	Device realization .....	78
4.2	Experimental apparatus in Naples .....	81
4.3	Field effect on resistivity vs. temperature behaviour.....	83
4.4	Conclusions.....	91
	<b>Conclusions</b> .....	93
	<b>References</b> .....	96



# Introduction

In last decade a lot of interest has been focused on the field of the oxides electronics, in particular possible device application of the transition metals perovskite oxides have been investigated. In fact, these strongly correlated systems show interesting multifunctional properties such as high temperature superconductivity (HTS) in cuprates, colossal magnetoresistance (CMR) in manganites, ferroelectricity in titanates or high dielectric constant. The attention paid to this class of material is mainly due to the possibility of integrating these different properties in a single multilayered structure thanks to the structural compatibility they present, leading to the implementation of new electronic devices.

Moreover, the transport features of the perovskite oxides are strongly influenced by the charge carrier density, as proved by the quite complex phase diagrams describing their behaviour. In some cases even a metal-insulating transition can occur as a function of the doping level. The carrier density was usually varied by doping, i.e. by non isovalent atoms substitution in the unit formula. Indeed, this approach introduces disorder and structural deformations, making difficult the individuation of the role of the carrier density variations.

Recently, field effect approach was successfully employed in order to verify the intrinsic role of the carrier concentration in perovskite oxides and interesting results have been obtained in modulating transport characteristics such as high temperature superconductivity and colossal magnetoresistance. In addition, field effect principle could lead to the realization of an all perovskite electronic switch device, which could be a possible candidate in substituting the Si-based electronic technology. Unfortunately, field effect experiments present some problems related to both the characteristics of the materials employed and the needed experimental set-up. The former consist mainly in the thickness of the layer affected by the electrostatic modulation, governed by the carrier concentration via the Thomas-Fermi screening length (the smaller the carrier concentration, the greater the penetration of the electric field in the material); in the dielectric constant value of the insulating material employed to apply the modulating electric field; in possible interface related problems between the two. The latter are mainly due to the need of monitoring the very little leakage currents that can flow across the dielectric material during the experiment and to the possibility of measuring very high resistance values because of the little carrier concentrations desired to observe substantial electrostatic modulation effects.

In this thesis the results obtained in field effect experiments on very thin superconducting films are reported. The principal aim of the work was acquire more informations about the field effect mechanism on superconductor thin films by studying two different systems characterised by low carrier density and no interface related problems, paying attention to the instrumentation related problems. The work was performed between the *Dipartimento Scienze Fisiche* at the *Univeristà degli studi di Napoli* and the *Département de Physique de la Matière Condensée* at the *Université de Genève*.

In Geneva a STO single crystal field effect device was realised and tested. The interest in the strontium titanate arises from the observation of an insulator-metal transition occurring in it at very low doping levels. In addition, the possibility of integrating in a single device both these transport features and the dielectric characteristics of its undoped state make this material very attractive. A new hydrogen plasma reducing technique was employed to obtain very thin surface doped layers on STO syngle crystals. The characterization of the obtained doped surface layers electronic transport in terms of resistivity, magnetresistance and Hall effect, all as a function of the temperature, was carried out first. Then the field effect response of these thin doped surface regions was studied exploiting the dielectric fatures of the remaining non-doped STO substrate. The low carrier density and the defect free interfaces obtained, at least in principle, promise great modulation effects can be achieved. In order to verify the applying modulating field acts on the carrier concentration, Hall effect and field effect measurements were performed simultaneously.

In Naples, underdoped NBCO very thin films were employed as channels in field effect devices. This compound, a classical example of cuprate superconductors, has shown a dependence of its electronic transport features as a function of the film thickness, presenting even Mott insulating behaviour in thinnest samples. In order to perform field-effect experiments on this material, devices consisting in NBCO thin films deposited on STO substrates and covered by an  $\text{Al}_2\text{O}_3$  thin layer were realised. Thanks to the deposition technique employed, completely in-situ, interfaces between the NBCO films and both the STO substrate and the  $\text{Al}_2\text{O}_3$  layer result of great quality. In this way both the materials could be exploited as dielectric to apply the modulating field across. A great effort was devoted to arrange a masurement set-up capable of measuring high resistance values in order to mainly investigate the electrostatic modulation of the thinnest insulating samples. Finally, in order to achieve information on the effective modulation of the carrier concentration, Hall effect and field effect simultaneous masurements were performed on few insulating samples exploiting the instrumental apparatus in Geneva.

The obtained results are reported in this work as schematically illustrated in the following.

In the first chapter, after a brief and general introduction to the correlated electron technology, the more relevant perovskite oxides features are presented. Then the role of the carrier concentration in determining the perovskite transport feature is illustrated. After an overview on the field effect working principle, where the main parameters affecting the experimental results are highlighted, a brief discussion about the field effect on superconducting materials follows, with particular attention in field effect induced phase transitions. Finally the Hall effect is discussed.

In chapter two the most noticeable properties of the two investigated materials are presented. In the first part of the chapter the features of undoped insulating first and then of doped metallic STO are discussed. In the second part, after a brief discussion about the HTS general phase diagram, structural and electronic properties of NBCO thin films are reported.

In the following two chapters the experimental results are reported. In chapter three, after a description of the available experimental set-up in Geneva, the hydrogen plasma technique employed for the STO single crystals surface reduction is illustrated and the procedure followed to obtain the final devices explained. Then, the results of the electronic transport characterization of the doped surfaces in term of resistance vs. temperature behaviour, magnetoresistance and Hall effect are shown. Finally the obtained field effect experiments results are reported followed by the results of the simultaneous Hall effect and field effect measurements.

In the fourth chapter, the NBCO based device realization is illustrated and the measurement equipment available in Naples discussed. Then the results of the field effect modulation are reported, with particular attention to the IV curves. Finally, the information carried out by the simultaneous Hall effect and field effect measurements performed in Geneva are discussed.

# Chapter 1

## Oxides Electronics and Field-effect doping

### 1.1. Oxides Electronics and Correlated-Electron Technology

Recently, worldwide attention has been focused on the so-called oxide electronics, as promising future alternative to standard silicon electronics. In particular many efforts have been carried out in order to fabricate and analyse epitaxial heterostructures or devices of perovskite oxides. These materials are examples of strongly *correlated electronic systems*, where the electron-electron Coulomb repulsion interaction is strong and electrons are almost localized or barely mobile. Here a naive single-particle approximation (considering a moving electron as an independent particle in the effective medium) does not hold [1]. Moreover, in this class of materials not only charge and spin interactions are of relevance, but even the lattice and orbital ones (Figure 1). These interactions lead to the coexistence of several competing states, as exemplified by the complex phase diagrams these materials present (see sect. 1.3) [2].

Strongly correlated perovskites include compounds presenting different physical properties, such as high temperature superconductivity in cuprates, high  $k$  dielectrics, ferroelectrics in titanates and colossal magnetoresistance in manganites (see sect. 1.2). In addition, thanks to the isostructural nature of these compounds, the possibility of matching materials with different physical properties in the same crystalline structure opens new perspectives for oxide electronics. The recent advance of the fabrication technologies used to prepare thin films and superlattices has begun to produce correlated-electron junctions and atomically controlled layered structures that can be viewed as tailored correlated-electron materials. With use of the Pulsed Laser Deposition (PLD), Molecular Beam Epitaxy (MBE) or laser ablation (laser MBE) methods, thin films can be grown in a layer-by-layer mode for most of perovskite oxides. A straightforward application of this technique is the

fabrication of perovskite superlattices composed of a few-u.c.-thick perovskite-layers with different compositions. The perovskite superlattices can be composed of a variety of combinations, and not

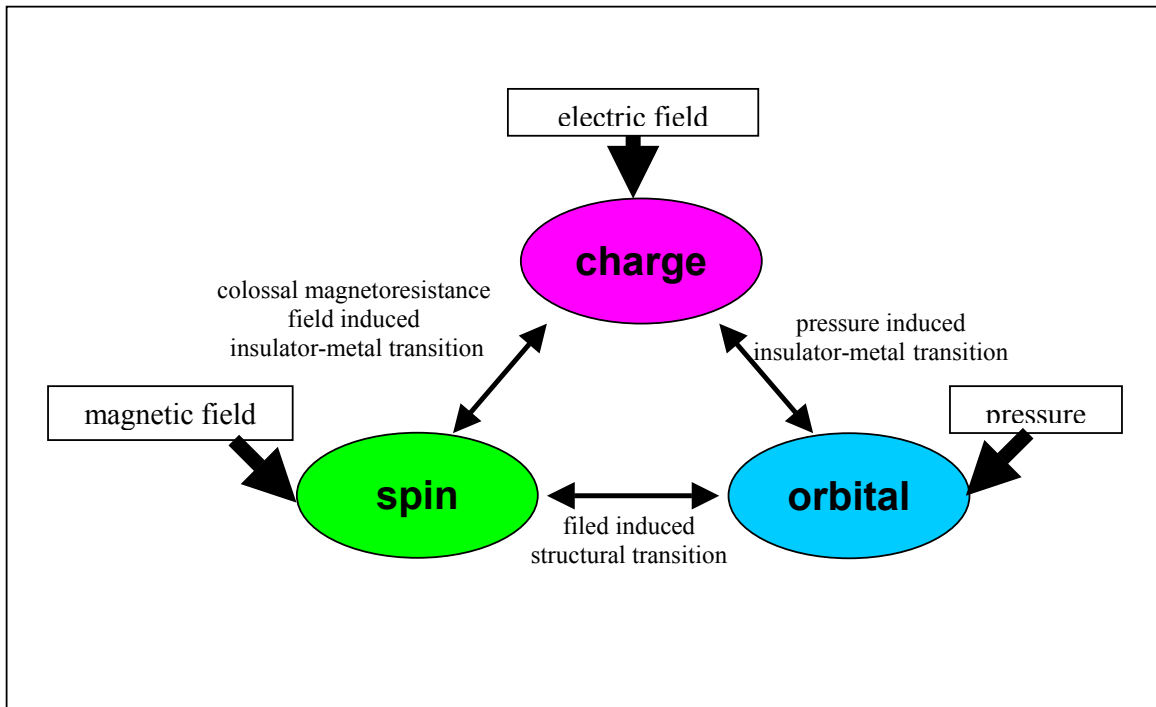


**Figure 1** Spin-charge orbital coupling for correlated electron systems (adapted from [1])

only the charge gap and spin structure, but also the orbital state of the constituent layers play important roles in determining the properties of the superlattices. Superconductor-ferromagnet, ferroelectric-superconductor, ferroelectric-ferromagnet or ferromagnet-antiferromagnet combinations are examples of such hybrid structures (see for example [3]).

Exploiting the mentioned features, a new field using all the attributes of electron, i.e. charge, spin and even orbital, is attracting a growing interest, the correlated-electron technology (CET). The concept of CET is just opposite that of single-electron manipulation: its emphasis is laid on the control of the electronic phase which interacting many electrons can form [1]. The electronic/magnetic phase of a material containing correlated electrons can be controlled in unconventional ways, i.e. conductivity and magnetization can be controlled by magnetic and electric field respectively, and in an ultrafast way (at terahertz frequencies), so CET may provide a seed for a new class of electronics.

Several examples of perovskite oxide devices have already been realized such as ferroelectric memories (FeRAM), field effect transistors (FET), and ferroelectric field effect (FeFET) or spin injection devices. There is a wide range of applications of other perovskite related materials, e.g., as

magnetic sensors, in digital devices, in filters and other microwave components, in varactors, for data storage and magnetic recording devices, as chemical sensors, catalysts and multilayer capacitors and in fuel cells. Motorola Labs has announced that it has built the world's thinnest functional transistor using a class of perovskite materials that will enable future transistors to be exponentially smaller and faster while consuming less power [4]. The new technology enables the development of a transistor with an effective thickness that is initially three-to-four times thinner than those built with today's conventional semiconductor materials.

## 1.2. Perovskite oxides properties

Most compounds with the general formula  $ABO_3$  have the perovskite structure. The unit cell of  $ABO_3$  is represented by the  $A$  ions at the corners of a cube with  $B$  ions at the body centre and the oxygen ions at the centres of the faces (Figure 2). In the perovskite-type oxides, the  $A$  cation is coordinated with twelve oxygen ions, and the  $B$  cation with six. Therefore, the largest number of perovskite-type compounds are described by the general formula  $A^{2+}B^{4+}O_3$ , where the  $A^{2+}$  cations are alkaline-earth ( $AE$ ) ions, cadmium, lead and so on, while the  $B^{4+}$  cations are Transition Metals ( $TM$ ) and some rare-earth ( $RE$ ) ions, which are, in general, smaller than the cations of the  $A$  site.

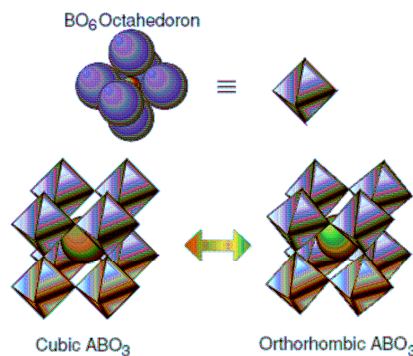


**Figure 2** Perovskite structure  $ABO_3$ . The A ion surrounded by the eight  $BO_6$  octahedra. The tilting of the  $BO_6$  octahedra changes the lattice symmetry from cubic to orthorhombic, teragonal or rhomdohedral [5]

The interest in perovskite oxides arises from the large variety of the noticeable properties they present, which lead to possible alternative to silicon electronics both in materials substitution and in new devices realization as briefly discussed in the following.

Some perovskite oxides, such as SrTiO<sub>3</sub> (STO) and related materials, show a high dielectric constant  $\epsilon$ , on the order of 300 at room temperature and 24000 at liquid helium temperature for STO (see chapter 2). Even if the Si-SiO<sub>2</sub> structure has several superior properties in respect to other dielectric materials, such as electrical stability and the high SiO<sub>2</sub> dielectric breakdown, the reduction in size of the gate oxide on a MOSFET and of DRAM capacitors poses some problems whose solutions seems to lay in finding a substitute dielectric materials with higher dielectric constant  $\epsilon$ . As a matter of fact, reducing the thickness of the dielectric material in a MOSFET or a DRAM capacitor causes a linearly proportional increase in the electric field across the dielectric material if the voltage supplied to the devices remains constant. This increase in electric field makes breakdown a concern in the scaling of dielectrics. Using a dielectric material with a higher dielectric constant may overcome the difficulty, making possible shrinking the effective thickness of a transistor without rapidly increasing the leakage current. This development could enable future integrated circuits to be faster and more powerful. Moreover, a good flat interface is required in MOS structures, otherwise the electric field lines become concentrated wherever a defect is present thereby greatly enhancing the electric field at that point. This defect point therefore becomes the failure point of the dielectric and leads to device breakdown.

Perovskite titanates, such as PbZr<sub>x</sub>Ti<sub>1-x</sub>O<sub>3</sub> (PZT) or BaTiO<sub>3</sub>, show a ferroelectric behaviour, described by the hysteresis curve giving the polarization ( $P$ ) as a function of electric field ( $E$ ) reported in Figure 3. These materials present a non-centrosymmetric atomic unit cell: in this way the dipole moment is switchable with an external electric field [6]. Main ferroelectrics applications are in tunable microwave filters, phase shifters and varactors. They are also suitable materials for computer RAM memories (Fe-RAM). The 2 logical states of the memory are discriminated by the voltage response of a ferroelectric capacitor. The cell is operated by destructive read-out. Unfortunately, repeated polarization reversals cause a degradation of ferroelectric properties, possibly resulting in fatigue failure [7]. Ferroelectric nano-structures are attractive for applications in high-density memory (64 Mbit - 4 Gbit) cells. 3D nanostructure memory cells with the sizes down to 100 nm proved to have two stable polarization states (hysteresis), a necessary property for application in memory cells.

The layered perovskite manganites of general formula RE<sub>1-x</sub>AE<sub>x</sub>MnO<sub>3</sub>, (where  $RE$  is a trivalent rare earth element e.g. La, Pr, Nd etc. and  $AE$  is divalent alkaline earth element e.g. Ca, Ba, Sr etc.) have also drawn considerable attention. In fact, in the mid-1990s they have been discovered exhibiting extraordinary large magnetoresistance, i.e. an almost 100% variation of their electric resistance under magnetic field, namely they show a *colossal magnetoresistance* (CMR), as reported in Figure 4 [8]. This feature has made them attractive for development of magnetic

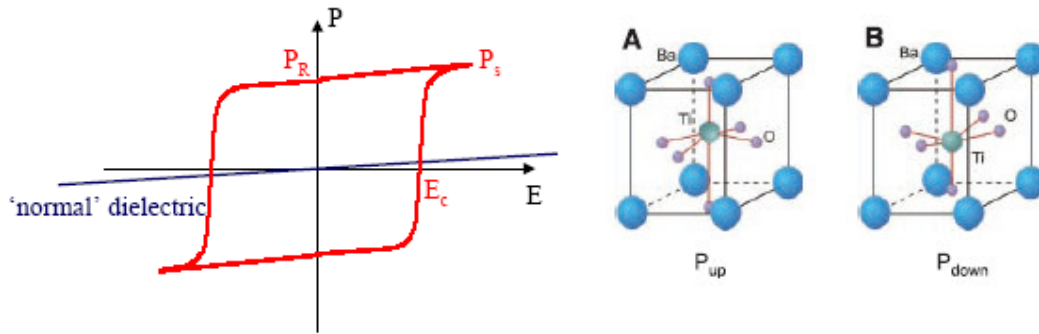


**Figure 3** Hysteresis loop of  $P$  as a function of the applied  $E$  and crystal structure of the perovskite ferroelectric  $\text{BaTiO}_3$  showing up (A) and down (B) polarizations [6]

sensors and reading heads for hard disk drivers with higher areal density (the number of bits/unit area on a disk surface). The problem in utilizing the effect is that, for bulk materials, such high values of MR can only be reached at magnetic fields of several Tesla.

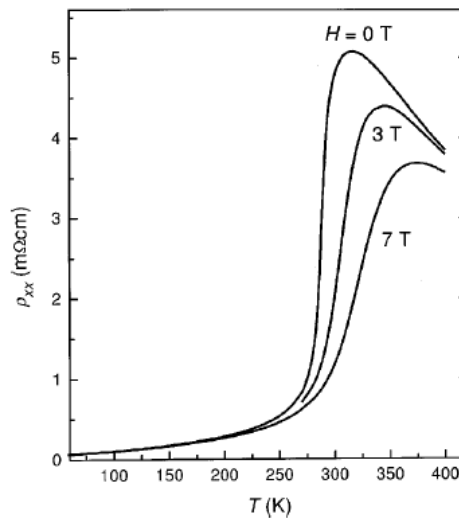


**Figure 4** Temperature dependence of  $\rho(H, T)$  of  $\text{La}_{2/3}(\text{Pb,Ca})_{1/3}\text{MnO}_3$  at various fields  $H$  [8]

Moreover, manganites seem to be excellent candidates for spintronics devices implementation thanks to the CMR effect itself and to the conduction via electrons of only one spin (half-metallic ferromagnetism). Spintronics, or spin-based electronics, is a new technology that manipulates an electron's spin (its orientation up or down), in addition to its charge, to store and transmit information. Spintronics devices, such as spin valve or Magnetic Tunnel Junction (MTJ), are being developed for applications such as ultrasensitive magnetic sensors and magnetoresistive random

access memory (MRAM) [9]. Computers with spintronic memory will be able to store more data in a smaller area, access that data faster, and consume less power than today's semiconductor RAM chips. Potential advantages of the MRAM compared with silicon electrically erasable programmable read-only memory (EEPROM) and flash memory are 1000 times faster write times, no wearout with write cycling (EEPROM and flash wear out with about 1 million write cycles), and lower energy for writing. MRAM data access times are about 1/10,000 that of hard disk drives. In addition, after the electron spins have been aligned, they remain that way until changed by a magnetic field, even if the computer is shut off. This will create an "instant-on" PC that won't require booting up the computer to move hard-drive data into memory.

Perovskite-type BiFeO<sub>3</sub> or BiMnO<sub>3</sub> are ascribed to the new material class of multiferroic where magnetism and ferroelectricity coexist. Multiferroics, sometimes called magnetoelectrics, possess two or more switchable states such as polarization and magnetization. They show a highly reversible switching of electrical polarization using relatively low magnetic fields of 0–2 T. Moreover the combined application of electric and magnetic fields leaves a permanent imprint in the polarization. This 'reversible' polarization switching and memory effect are distinct from the 'non-reversible' rotation of ferroelectric domains by magnetic fields [10].

Cuprates exhibit High Temperature Superconductivity (HTS), thanks to the presence of conducting CuO<sub>2</sub> planes. After the first HTS compound discovered in 1987, several compound have been proved high temperature superconductivity, reaching the highest transition temperature in a Hg cuprate, 135 K at ambient pressure, rising to above 160 K under pressure. HTS have been employed in a large variety of technological fields. Passive microwave circuits, filter banks and cooled preamplifiers for mobile phone base stations, fast digital circuits, AD converters, microprocessors, low noise receivers are only few examples of their possible application in Information and Communication Technology. Several different devices exploiting HTS cuprates properties have been proposed so far as possible substitute to the standard Si-based MOSFET, such as Superconducting base transistors (SBTs), dielectric base transistors (DBTs), vortex flow transistors (VFTs) (see [11] and references therein). In addition, exploiting the magnetic flux quantization feature, the Rapid Single Flux Computation (RSFQ) logic has been proposed as alternative to the standard Si-based transistor technology for very fast processor realization.

### 1.3. Doping effect on perovskite-oxides properties: phase diagrams

It is well established that perovskite oxide materials exhibit complex phase diagrams (structural, electronic and magnetic) as a function of doping, classically achieved by the  $A$  ion substitution. The  $BO_6$  octahedron in a perovskite oxide  $ABO_3$  forms a three-dimensional network. The most important advantage of the perovskite structure is that the  $BO_6$  network is stable for substitutions of the  $A$ -site ion. The  $A$ -site cation is completely ionised in most cases without contributing to the band formation. By this ionization of the  $A$ -site, electrons are left in the oxygen  $2p$  bands and/or the  $TM d$  bands. With this advantage, the nominal number of conduction electrons per unit formula can be controlled by the chemical substitution of an  $A$  ion, leading to the systematic control of the electronic states with this  $ABO_3$  compounds.

As already stressed in sect. 1.1, the strong correlation doesn't allow anymore using the band structure model and associated Fermi liquid description that take account of the properties of ionic insulators, elemental semiconductors and simple metals. Moreover, the electron localization can results in a special type of insulator, frequently called the *Mott insulator* [12]. The mentioned charge, spin and orbital interactions lead to the coexistence and even the competition between different phases, which are strongly influenced by the carrier concentration. Part of the filling control and the bandwidth control researches are summarized in a schematic phase diagram shown in Figure 5, where the role of the electron-electron repulsion  $U$  is shown. The four thin lines, which connect the  $B$ -site  $TM$  cations, correspond to  $A = Y^{3+}$ ,  $La^{3+}$ ,  $Ca^{2+}$  and  $Sr^{2+}$ .  $\Delta$  is the charge transfer energy between the  $TM 3d$  band and the oxygen  $2p$  band. Simple band calculations with the local density approximation show all the materials in Figure 5 with a partially filled d-electron band (so except

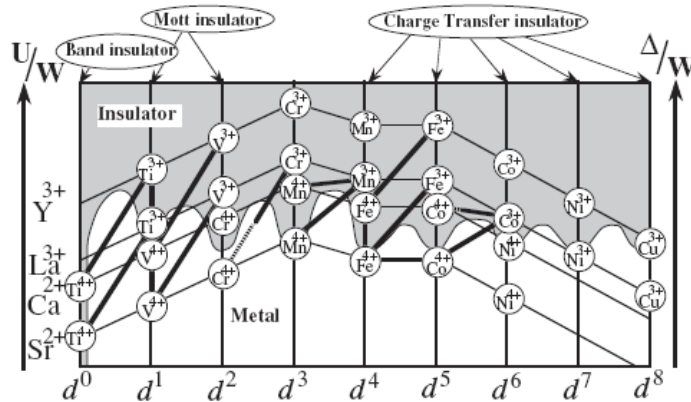


**Figure 5** Schematic phase diagram of  $ABO_3$  for  $A=Y^{3+}$ ,  $La^{3+}$ ,  $Ca^{2+}$  and  $Sr^{2+}$ .  $U$  is the electron-electron repulsion energy;  $W$  is the one-electron bandwidth and  $\Delta$  is the charge transfer energy between the  $TM 3d$  band and the oxygen  $2p$  band

for the  $3d0$  band insulator) should be metallic [5]. However, several compounds in the shaded area are insulating, because of electronic correlations leading to the opening of a direct gap in the 3d band (Mott–Hubbard insulators) or an indirect gap between the oxygen 2p band and the upper Hubbard band (charge transfer insulators) [15]

The effect of doping on the transport properties of oxides perovskites has been widely studied in the past. So now it's well known that the high- $\epsilon$  dielectric STO may become semiconducting or metallic if doped with Nb or La or if the oxygen content is deviated from the stoichiometric value (see chapter 2). Again, quite complex phase diagrams have been carried out from systematic studies, in particular for both HTS and CMR manganites, in which different electrical behaviours can be obtained as a function of the temperature and the doping. In Figure 6 examples of manganite (A), superconductors (B), ruthenates (C) and Co oxides (D) are reported.

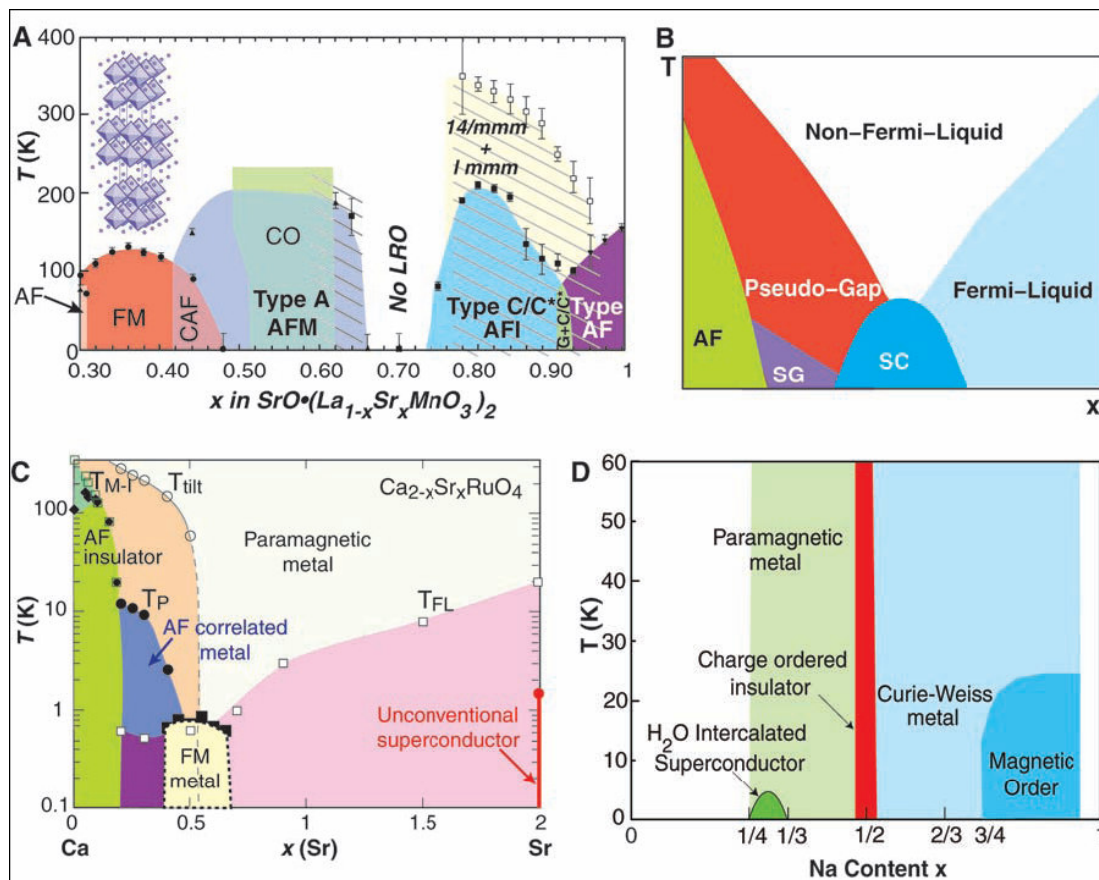


**Figure 6** (A) Temperature versus hole density phase diagram of bilayer manganites, including several types of antiferromagnetic (AF) phases, a ferromagnetic (FM) phase, and even a globally disordered region (no LRO); (B) Generic phase diagram for HTS. SG stands for spin glass; (C) Phase diagram of single layered ruthenates evolving from a superconducting (SC) state to an AF insulator; here  $x$  controls the bandwidth rather than the carrier density; (D) Phase diagram of Co oxides with SC, charge-ordered (CO), and magnetic regimes [2]

As shown in the phase diagrams reported, the main effect of doping on the perovskites oxides behaviour acts via the variation of the carrier concentration. This arises as the crucial parameter that governs the transport properties of strongly correlated systems. But doping by atoms substitution, as described above, leads to the introduction of disorder and lattice structural deformations too, which could also influence the materials response. Electrostatic field effect experiments, by which controlled and reversible tuning of the carrier concentration can be achieved, can overcome this problem making possible the study of the intrinsic role of the carrier concentration. In addition a modulation of the carrier density on the edge of the phase boundary based on the field effect approach is the fundamental idea of a correlated electron device. In next sections the main features and even related problem of such a technique are discussed, with particular emphasis on superconductors materials.

## 1.4. Field effect doping

The basic principle of field effect consists in applying a transversal electric field using a *gate electrode* to a thin film (*channel*) across a dielectric material (*gate insulator*) deposited on it. In this way charge carriers in the channel are attracted or repelled at the interface with the gate insulator, creating a thin accumulation or depletion layer (depending on the carrier charge and the applied field polarization). This results in a variation of the channel resistance between two electrodes, namely *source* (S) and *drain* (D). The MOSFET (Metal Oxide Semiconductor Field Effect Transistor), the basic element of the integrated consumer electronics on Very and Ultra Large Scale of Integration (VLSI and ULSI) works on this principle. Here the channel is a doped Si film between two heavily doped-Si regions that act as source and drain electrodes, while a SiO<sub>2</sub> layer is the gate insulator (Figure 7).

It's worth noticing that a stack structure is needed to exploit the field effect, i.e. a MIS (Metal Insulator Semiconductor in case of MOSFET) structure, and that in the discussion above we implicitly assumed the gate insulator deposited on the channel. But another possibility to create the stack structure arises if the thin film under test is deposited on a dielectric substrate that can be employed as gate insulator at the same time, as shown in Figure 8.

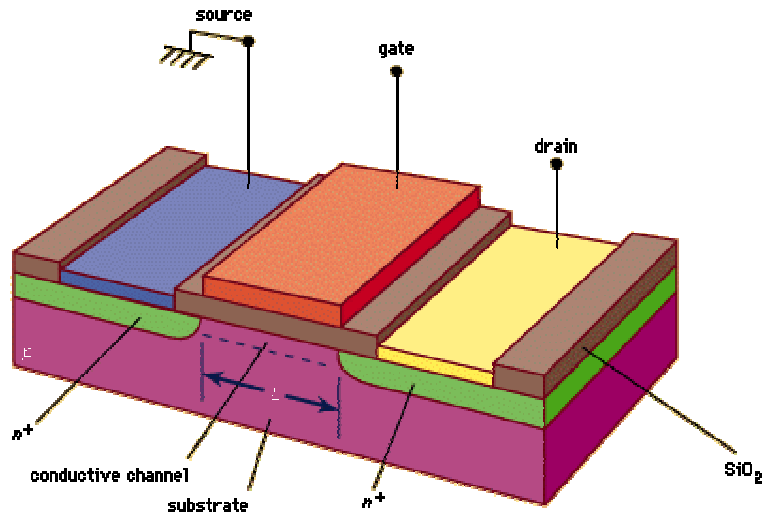


**Figure 7** Schematic cross sectional view of a MOSFET

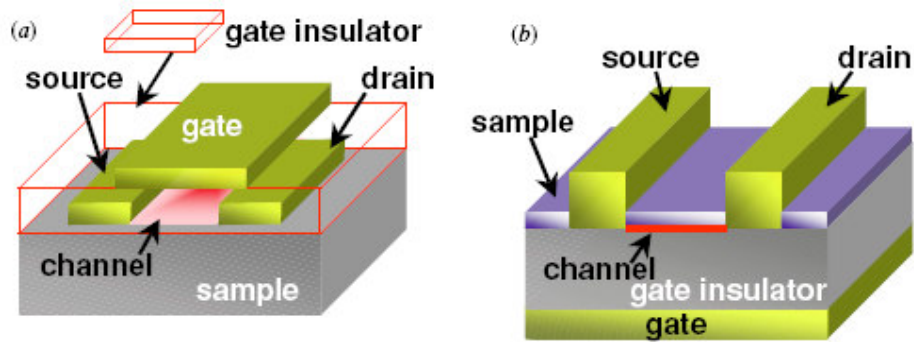


**Figure 8** Schematic FET structures: (a) a thin film of gate insulator is deposited on the surface of the sample and (b) a thin film of a sample is deposited on the surface of a dielectric crystal [5]

Field effect approach has been followed in the past not only to realise new switching devices, but also to study the actual effect of the carrier concentration variation on strongly correlated systems with no disorder introduction due to the ions substitution [5,15].

In 1998 Newns and coworkers first proposed a field-effect based device made entirely of oxides materials. More in detail they proposed a Mott Transition Field Effect Transistor (MTFET) where

the channel consists of a Mott insulator, in particular they used a cuprate underdoped HTS in its insulating phase. The aim of this device was to exploit the charge accumulation due to the appliance of the transverse field in order to induce an insulator-metal transition in the channel [13]. It is believed, for instance, that the Mott transistor has the following advantages: (1) no extended intrinsic length scale, enabling theoretical scalability to extremely small length scales, e.g. 10 nm channel length and (2) broad compatibility with computer engineering switching requirements.

Even if the basic working principle of a FET device is quite simple, several technical difficulties arise when field effect experiments take place in order to verify the actual modulation of the transport features of the channel.

The characteristic width of the accumulation or depletion layer is given by the electrostatic screening length  $\lambda_{el}$ , which in the semiclassical, metallic limit is the Thomas–Fermi length:

$$\lambda_{el} = \sqrt{\frac{\epsilon_s \epsilon_0 E_F}{6\pi n e^2}} \quad (1.1)$$

Here  $\epsilon_s$  and  $\epsilon_0$  are the dielectric constants of the channel and vacuum, respectively,  $E_F$  is the Fermi energy,  $e$  is the elementary charge and  $n$  is the carrier concentration of the channel. In standard metallic systems,  $\lambda_{el}$  is extremely short, a fraction of an atomic diameter, because of the high carrier concentration, and thus negligible field effects are found. In low-carrier-density systems, larger screening lengths and field effects are expected, which are reasons why standard transistors are made with semiconductors rather than metals. Moreover, in order to achieve substantial carrier modulation ultrathin drain–source channels so that the absolute number of carriers is small allowing large relative changes in their total number. Because the carrier modulation occurs in an interfacial layer, it is also advantageous to use very thin channels to avoid shunting phenomena between the field effect modulated layer and the rest of the channel. It's worth noticing that in the classical Thomas–Fermi model the carrier densities change abruptly from some large external value to zero at the interfaces of the insulator. However, the real charge density goes essentially to zero (except for a small amount of penetration by quantum tunnelling) in the gate insulator. However, the carrier densities must be continuous across the interface, resulting in significant differences in classical and quantum carrier profiles. The average spatial extent of the charge in the sample is much larger when calculated quantum mechanically than classically [5].

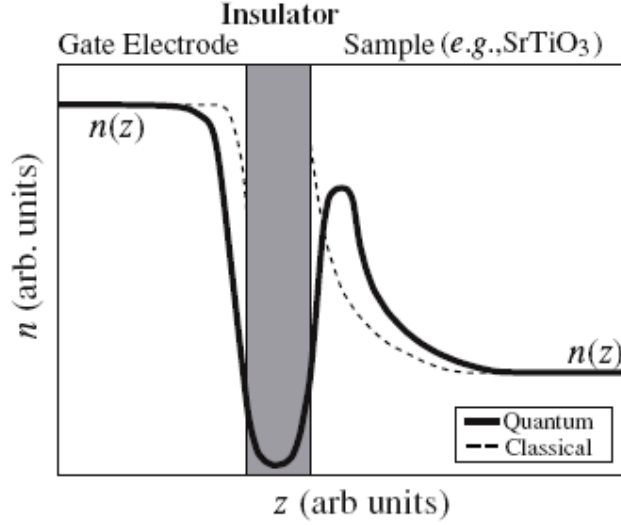


**Figure 9** Schematic of classical (dashed lines) and quantum (solid lines) carrier density profiles through an ideal MIS structure [5]

Another way to achieve large modulation of the carrier density is to apply extremely large electric fields across the gate insulator, increasing its dielectric polarization, limited by the breakdown field  $E_{BD}$ . The maximum polarization  $P_{max}$  that can be induced in a dielectric can be expressed as

$$P_{max} = \int_0^{E_{BD}} \epsilon_0 [\epsilon(E) - 1] dE \quad (1.2)$$

where  $\epsilon_0$  is again the vacuum dielectric constant and  $\epsilon(E)$  the small-signal dielectric constant at an applied bias field  $E$ . The same concept can be seen in a different way in order to highlight the gate insulator layer requirements. At a fixed applied gate voltage  $V_g$ , the areal charge density  $\sigma$  induced in a dielectric layer of thickness  $t$  can be expressed as

$$\sigma = \int_0^{V_g} \frac{\epsilon_0 \epsilon_r(V)}{t} dV \quad (1.3)$$

where  $V_g < E_{BD}t$ . So high- $\epsilon$  dielectric materials with a high breakdown field should be used as gate insulator. Even its thickness could be reduced in order to induce greater areal charge densities, but in this way, for a fixed applied voltage, a greater field is setted within the dielectric and the

breakdown field can be reached more easily. Moreover leakage currents through the insulator must be much smaller than the DS current, ideally absent, in order to avoid their effect on the variation of the channel resistance. Finally, the density of localized interface states in the dielectric must be small compared with the modulated carrier density.

In standard MOSFET devices, the universal gate dielectric is  $\text{SiO}_2$ , an excellent insulator with low leakage that is chemically stable and virtually free of interface states characterised by a breakdown field  $E_{\text{BD}}=10\text{MVcm}^{-1}$  and a dielectric constant  $\epsilon_r=3.9$ . There the gate induced carrier density in the channel is  $10^{11}\text{--}10^{12}/\text{cm}^2$  [14]. But in an all-oxide FET device with a strong correlated system as channel a greater variation of the areal charge density has to be induced to obtain a substantial channel behaviour modulation. Figure 10 shows the zero temperature behaviour of some of the materials discussed so far as a function of their sheet charge density. SO, to change the carrier density by 50% in a 1-nm-thick oxide superconductor with  $4\times 10^{21}$  holes  $\text{cm}^{-3}$ , for example, requires sheet charge densities or polarizations of  $30\ \mu\text{Ccm}^{-2}$ , an order of magnitude larger than what can be achieved in standard FETs

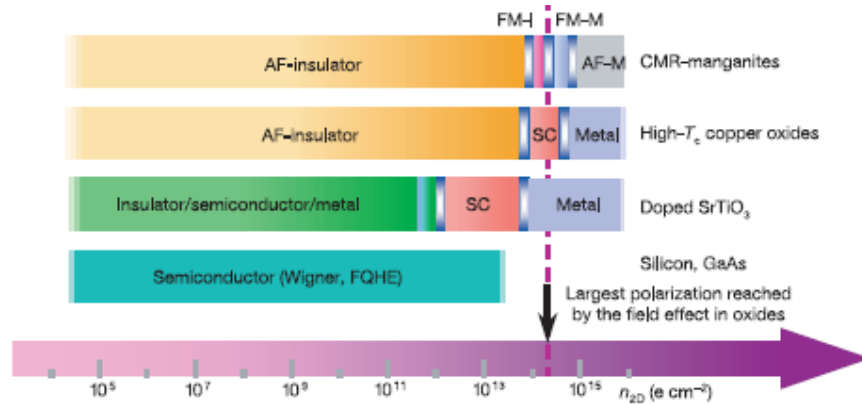


**Figure 10** The zero temperature behaviour of various correlated materials as a function of the sheet charge density [15]

Exemplars of the dielectric thin films used so far to carry out the electrostatic carrier doping to the perovskite TM oxide are  $\text{SrTiO}_3$ ,  $\text{Al}_2\text{O}_3$ ,  $\text{CaHfO}_3$  and  $\text{MgO}$  (see [5] and references therein). Moreover, it should be noted that there have been a number of studies of the *ferroelectric* field effect (FeFET) in complex oxides using a ferroelectric thin film as a gate insulator [16, 6,15 and references therein]. In those FeFET, the field effect is due to the polarization of the ferroelectric material. Therefore, the carrier density of the materials cannot be controlled continuously by the applied gate electric field. But the converse is that there exists no gate leak current, and thus authentic electrostatic carrier-doping effects are observed.

## 1.5. Field effect experiments on High-Temperature Superconductors

The field effect approach has been applied to study a wide class of materials, but most field-effect work on complex oxides has focused on high temperature superconductors.

The high- $T_c$  superconductors are doped charge transfer insulators (see sect.1.3), and the role of carriers is depicted in the temperature–doping phase diagram sketched in Figure 11. The parameter  $x$  stands for the doping level, which is roughly proportional to the number of ‘free’ electrical carriers in the system. At low doping levels, the system is an antiferromagnetic insulator owing to strong electronic correlations. As the doping level is increased, superconductivity appears, with the transition temperature  $T_c$  following a roughly parabolic dependence on  $x$ . The high  $T_c$  copper oxides are composed of  $\text{CuO}_2$  sheets separated from each other by atomic barrier called “block layers”. The  $\text{CuO}_2$  sheet is originally insulating because of the large correlation effect, while

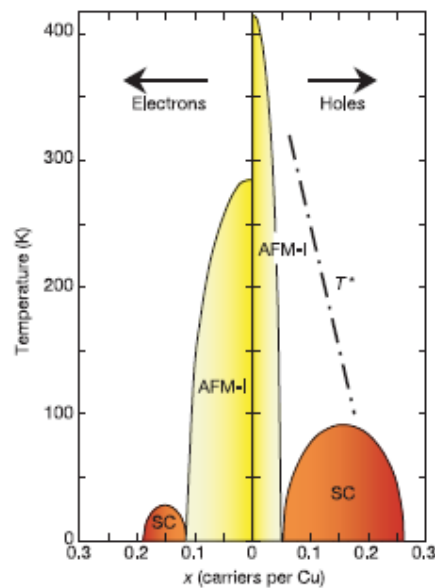


**Figure 11** Phase diagram of the high- $T_c$  superconductors. The electron-doped material represents  $\text{Nd}_{2-x}\text{Ce}_x\text{CuO}_{4-y}$ , and the hole-doped system represents  $\text{YBa}_2\text{Cu}_3\text{O}_{7-\delta}$ . The insulating, antiferromagnetic phases (AFM-I) are drawn in yellow, and the superconducting phases (SC) are in orange [15].

possessing one conduction electron (or hole) per Cu site. This is a typical example of the Mott insulator. The high-Tc superconductivity emerges upon the filling-controlled Mott transition, namely, as soon as the charge of the ionic block layer, or equivalently the change in the bandfilling (number of conduction electrons), cause the Mott transition. However, the strong antiferromagnetic correlation, originated in the Mott-insulating CuO<sub>2</sub> sheets, clearly subsists in the metallic state and this has been believed to be most relevant to the mechanism of high-Tc superconductivity

Field effect experiments have also been performed in classical superconductors since the sixties [17], but HTS are much more interesting for this kind of investigation thanks to their lower carrier densities (on the order of 10<sup>21</sup> cm<sup>-3</sup>). In fact, as the pair potential of a superconductor is a function of the Cooper pair density, all superconducting properties in the field-penetrated layer depend on the applied electric field if  $\lambda_{el}$  (1.1) is at least comparable to the coherence length:

$$\lambda_{el}(T) \geq \xi(T)$$

and in high-Tc superconductors,  $\lambda_{el}(T)$  is of the order of 0.5–1 nm, so this condition is generally fulfilled. Indeed, numerous experiments, which are preferably performed with ultrathin high-Tc films to maximize the ratio of the penetration depth to the film thickness, have confirmed the existence of large field effects in the high-Tc cuprates (see[11] and references therein). The principal results lays in the shift of the transition temperature towards higher values if carrier are added by applying the transverse field to the HTS thin film and vice versa [18, 19].

There has been some debate on whether the electric field effect in YBa<sub>2</sub>Cu<sub>3</sub>O<sub>7-x</sub> is due to oxygen diffusion rather than to redistributions of mobile charge carriers, which of course would be detrimental to device applications. But subsequent experiments have revealed that large electric field effects are a general property of the high-Tc cuprates, in contrast with their low-Tc counterparts, for which  $\lambda_{el}(T) \ll \xi(T)$ ; and the field effects are only marginal [20].

Recent ferroelectric field-effect experiments on underdoped thin films of NdBa<sub>2</sub>Cu<sub>3</sub>O<sub>7-δ</sub> have also correlated quantitatively changes in Tc with changes in the carrier concentration produced by the field effect. This result is just an example of the importance of the field-effect approach as tool to better comprehend the effective role of carrier concentration in cuprates with no disorder introduction due to the chemical doping [21].

Moreover, at low doping levels, near the superconductor–insulator phase boundary, field-effect tuning of the carrier density should induce a reversible insulator–superconductor phase transition. Such superconducting switching behaviour is appealing from both a fundamental perspective and for potential applications. Recently experimental evidences of such transitions have been observed

by Ahn and coworkers in 1999 [16] and by Parendo and coworkers in 2005 [22]. In the former case ultrathin  $\text{GdBa}_2\text{Cu}_3\text{O}_{7-x}$  (GBCO) films have been studied by the FeFET mentioned in previous section. It's worth mentioning that in this work the possibility offered by perovskite oxides of multi-function integration has been exploited. In fact the field effect was performed by poling a  $20\text{\AA}$  thick ferroelectric  $\text{Pb}(\text{Zr}_x\text{Ti}_{1-x})\text{O}_3$  (PZT) film grown epitaxially on the GBCO film [see 16 for more details]. The GBCO film different behaviours as a function of the applied field are reported in Figure 12(a). While the lower curve shows a typical superconducting behaviour, the upper one corresponding to carrier depletion in the thin film under test due to the ferroelectric polarization, shows an insulating behaviour. In Figure 12(b) the results obtained by Parendo on ultrathin  $10,22\text{\AA}$  amorphous bismuth (*a*-Bi) are reported. Here the film under test normally shows an insulating behaviour, while a superconducting transition is induced by applying a positive gate voltage. In this work, in order to overcome the difficulties related to preparing high quality cuprate films with thicknesses on the order of the electrostatic screening length and chemically doped so that they are near a phase boundary, an homogeneously disordered ultrathin film have been chosen. In addition, an STO single-crystal served as both the substrate and the gate insulator. Yet, the authors have showed the increasing of the transition temperature as long as the applied gate voltage increases.

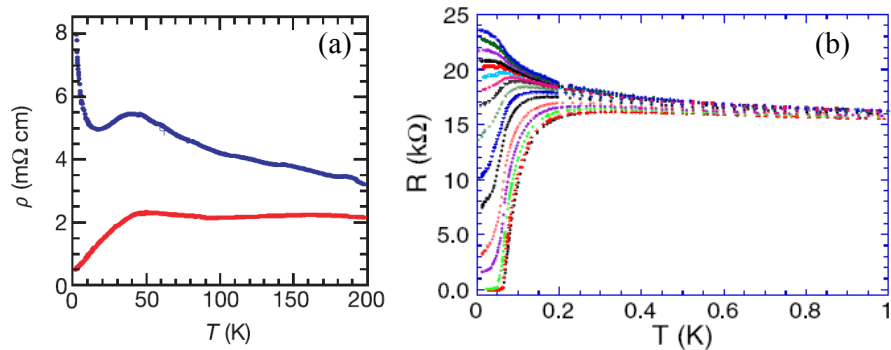
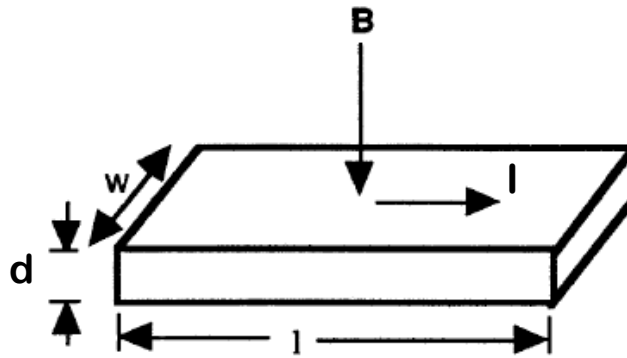


**Figure 12** (a) Resistivity versus temperature of a PZT/ $20\text{\AA}$  GBCO/ $72\text{\AA}$  PBCO heterostructure; in the upper curves holes have been depleted from the system [16]; (b)  $R(T)$  as a function of  $V_G$  for a  $10.22\text{\AA}$  thick *a*-Bi film; from top to bottom, gate voltages are 0, 2.5, 5, 7, 8, 9.6, 11, 12.5, 14.5, 17, 19.5, 24, 28, 33, 38, and 42.5 V [22]

## 1.6. Hall effect

As well known, the Hall effect experiments are powerful tool to characterize electrical transport features of materials. When a magnetic field  $B$  is applied at right angles to the direction of current  $I$  flowing in a conductor, an electric field resulting from the force on a charge moving in a magnetic field is created in a direction perpendicular to both. The resulting measured voltage is the Hall voltage,  $V_H$ .



In the framework of the Fermi liquid theory the Hall voltage can be expressed as:

$$V_H = R_H \frac{IB}{d} \quad (1.4)$$

where  $d$  is the sample thickness and  $R_H$  is the Hall coefficient. Assuming only one kind of charge carrier is present in the sample under test:

$$R_H = \frac{1}{nq} \quad (1.5)$$

where  $n$  is the carrier concentration and  $q$  the elementary charge. Thus carrier sign and concentration in a conductor can be derived by Hall effect measurements. Even information about the carrier mobility  $\mu$  can be obtained by such measurements. In fact, remembering the definition of conductivity for a simple conductor:

$$\sigma = \mu nq \Rightarrow \mu = \frac{\sigma}{nq} = \frac{R_H}{\rho} \quad (1.6)$$

The mobility is a key parameter in determining the feat of a material as possible substitute of silicon in ULSI electronics. As a matter of fact in Si-based MOSFET performances such as Ion/Ioff ratio or the transconductance are governed by the quantity K defined as

$$K = \frac{1}{2} \mu C_{ox} \left( \frac{W}{L} \right) \quad (1.7)$$

where  $C_{ox}$  is the areal capacitance of the gate insulator and  $w$  and  $l$  are the width and the length of the channel, respectively.

The Hall coefficient is generally constant with temperature, but in HTS it shows a dependence as  $1/T$  over a wide temperature range. The cotangent of the Hall angle, defined as the inverse mobility divided by the magnetic field in a simple metal, is expressed as:

$$\cot(\theta_H) = \frac{\rho_{xx}}{\rho_{xy}}$$

where  $\rho_{xx}$  and  $\rho_{xy}$  are the longitudinal and Hall resistivity respectively.

Hence, performing field effect and Hall effect experiments at the same time would leading to the observation of the actual modulation of carrier density in field effect or better comprehend the actual role of the carrier concentration in the Hall response in cuprates. Such a study has been carried out by Gariglio and coworkers performing FeFET on epitaxial PZT/NdBa<sub>2</sub>Cu<sub>3</sub>O<sub>7- $\delta$</sub>  ferroelectric/superconducting heterostructures. They found that changing the carrier concentration electrostatically induces a constant relative change in the resistivity and inverse Hall constant as a function of temperature, pointing to a resistivity and Hall constant that are both inversely proportional to a temperature independent carrier density [23]. It's worth highlighting that in this work an increase of the slope of  $\cot(\theta_H)$  was observed in correspondence of a decrease of the carrier density, while in chemical doping the slope of  $\cot(\theta_H)$  generally decreases with decrease in doping levels, the difference due to the absence of structural changes or disorder. Again, field effect approach helped to focus on the exact role of carrier concentration.



# Chapter 2

## Materials

In this chapter the characteristics of the materials studied in next chapters by the field effect approach are discussed. The chapter is divided into two parts. In the first one the strontium titanate features, both in its stoichiometric insulating state (sec. 2.1.1) and in the doped or reduced metallic state are summarized (sec. 2.1.2); the very low temperature superconducting properties are discussed too. In the second part of the chapter, after a brief description of the classical high temperature superconductors phase diagram and the related transport features (sec. 2.2.1), the main structural and transport characteristic of  $\text{Nd}_{1.2}\text{Ba}_{1.8}\text{Cu}_3\text{O}_7$  thin films are discussed (sec. 2.2.2).

### 2.1. Strontium Titanate

#### 2.1.1. Insulating state and dielectric properties

Strontium titanate ( $\text{SrTiO}_3$  or STO) is a well known band insulator and one of the most studied perovskite oxides. In its normal state, it has a  $d_0$  configuration electron because of the presence of  $\text{Ti}^{4+}$  ions and it's characterized by a band gap of about 3,3eV [24].

STO has a cubic perovskite structure at high temperatures, shown in Figure 13, and undergoes a transition around 100K to a tetragonal state. Its perovskite crystal structure made it an usual substrate for epitaxial growing of other perovskite oxides and actually a large variety of STO-based heterostructures have been realised. STO has a lattice mismatch of only 1-2% with high-Tc superconductors and is compatible with film growth of these materials. For these reasons,  $\text{SrTiO}_3$  films are used in high-Tc heterostructures such as field-effect samples and superconducting quantum interference devices (SQUID's). Also of great technological interest are STO films grown on silicon, as the combination of STO's high polarizability and resistivity with a standard semiconductor makes STO a suitable candidate for VLSI devices such as dynamic random access memories (DRAM's).

Owing to their high dielectric constant and breakdown strength, strontium titanate and related perovskites are promising candidates for such applications. The maximum dielectric polarization

that can be withstood by an insulating layer is a critical parameter limiting not only the performance of field-effect devices based on high- $T_c$  superconductor heterostructures, but also the quality of capacitors in very large-scale integration (VLSI) memory cells.

In contrast to other materials in which comparable dielectric polarization can be obtained,  $\text{SrTiO}_3$  is not ferroelectric but remains paraelectric down to the lowest temperatures due to quantum fluctuations.

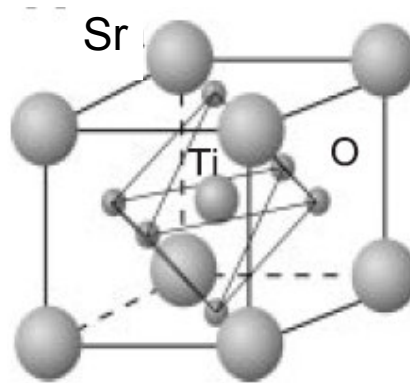


**Figure 13** STO cubic perovskite unit cell at high temperatures

In recent years, a renewed interest has been devoted to STO thanks to its large dielectric constant, mainly at low temperatures where, in the paraelectric phase, it can reach even the order of  $10^4$ , namely it saturates at a value of about 24000 [25, 26, 27].

Measurements of weak-field permittivity carried out by Saifi and Cross [26] on 400 $\mu\text{m}$  thick samples are reported in Figure 14(a). These permittivity measurements from room temperature down to 100K follow a modified Curie-Weiss law. Below 90K the dielectric constant deviates from the Curie-Weiss law. It's worth noticing that the virgin crystal gives the highest weak-field dielectric constant, which is irreversibly lowered after the application of an electric field. Similar results have been carried out by Christen and coworkers [27]. In their study they show simultaneously the temperature and the field dependence of the dielectric constant of STO single crystals, as reported in Figure 14(b), but they assumed a temperature dependence  $\epsilon(T)$  following a Curie law with a Curie temperature in the range of 30-36K between room temperature and about 60K. Moreover they observed a variation of the  $\epsilon$  low temperature value as a function of the film thickness.

$$\varepsilon = \frac{C}{T - T_C}$$

All the reported results show a typical feature of the STO dielectric constant, for both single crystals and thin films. Its value decreases as long as higher fields are applied to the samples and under high fields it presents a maximum in its temperature dependence at non-zero temperature, with the temperature at which this maximum occurs shifting toward higher values with increasing fields.

$E_{BD}$  of single-crystal STO has been measured by Barret. At 4,2K,  $E_{BD} = 4 \times 10^7$  V/m is found for samples with thicknesses ranging from 0,25 to 0,5mm.

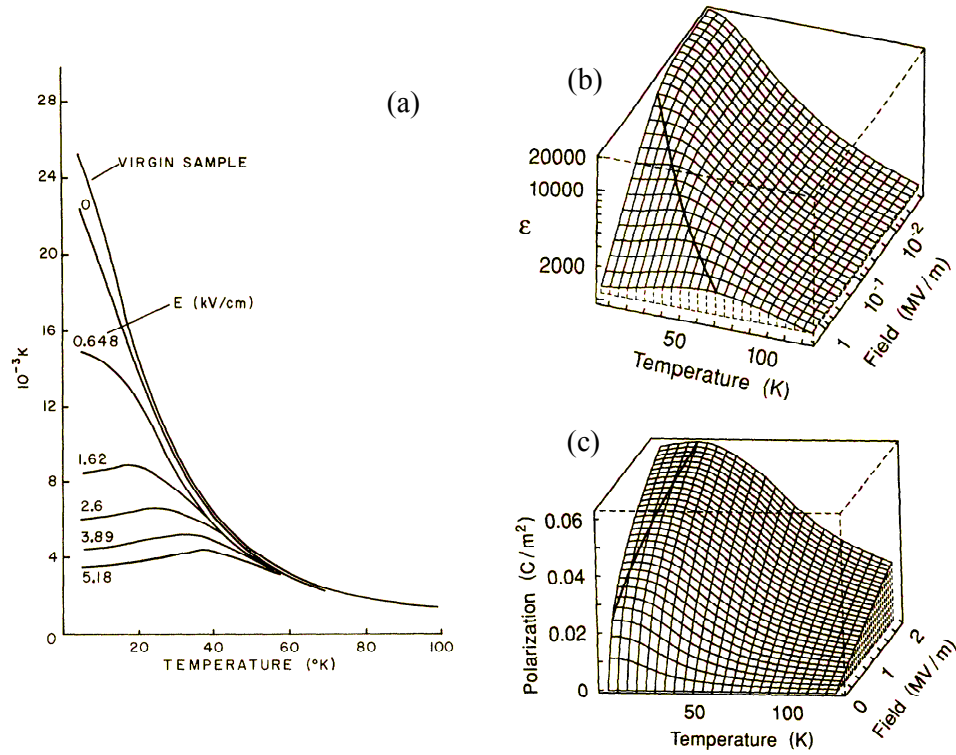


**Figure 14** STO dielectric constant dependence on temperature and applied field (a) after [26] and (b) after [3]; in (c) the achievable polarization resulting from data in (b)

In order to reach a greater polarization, very thin film could be used. But unfortunately, a dependence of the low temperature  $\varepsilon$  values on the film thickness was observed, i.e.  $\varepsilon$  decreases as long as thinner films are considered. As an example, the measured  $\varepsilon$  on 300nm thick STO films as a function of the temperature and for different applied electric fields is reported in Figure 17 [28].

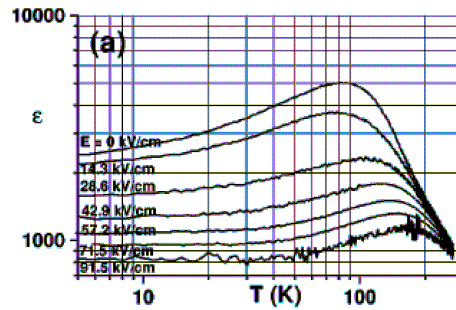


**Figure 15** Temperature and field dependence of the dielectric constant  $\epsilon$  measured on 300nm thick STO films [6]

Although  $\epsilon$  in thin films is significantly smaller ( $300 < \epsilon < 600$ ) than for single crystals ( $\epsilon > 24000$  at low fields) [29], small voltages applied across a film several thousand angstrom thick can produce very high electric fields, whereas in thicker dielectric crystals, the high voltages needed for these same fields could lead to breakdown via avalanche process. On the other hand, in pulsed laser deposition or sputtering grown films the termination layer cannot be controlled, and at a few hundred nanometers thickness, the surface roughness can be enough to prevent the growth of connected ultrathin films on top, whereas with single crystals, atomically flat surfaces can be obtained with uniform  $\text{TiO}_2$  termination after surface treatment.

In order to overcome this trade-off between maximum applicable field and thickness, a procedure to mechanically reduce a single crystal thickness have been proposed by Nakajima and coworkers [30]. This procedure have been used by Matthey and coworkers [31] in field-effect experiments on high  $T_c$  superconductors, but the zero-field value of the dielectric constant is found to be about 12 500 at 4.2 K and the maximum value obtained for the break-down field ( $E_{bd}$ ) is 10 times lower than values measured at low temperature on  $\text{SrTiO}_3$  thin films, probably due to cracks occurred during the grinding process.

### 2.1.2. Doped and reduced STO: metallic and superconducting behaviour

Electron doping is known to transform insulating  $\text{SrTiO}_3$  into a metallic state. The transition from insulating to metallic behaviour in this material occurs at an extremely small critical density of electron doping (around  $10^{18} \text{cm}^{-3}$ ), which is several orders of magnitude below the typical values

found for substituted transition metal oxides. This unusual behaviour has been related to the high dielectric constant. [32]

Doping can be achieved by altering any of the three sublattices, namely, those of strontium, titanium and oxygen: La substitution at the Sr site ( $\text{Sr}_{1-x}\text{La}_x\text{TiO}_3$ ), Nb at Ti sites and variation of the stoichiometric oxygen content are the most commonly employed ways to obtain doping. In particular, the latter can in principle lead to n-type conductors by removing oxygen atoms, or that's the same by introducing oxygen vacancies in the lattice, and even to p-type conductors by adding extra oxygens as schematically reported in Figure 16 [39]. Here both the p- and n- type are reported as a function of the defect concentration (in arbitrary units) versus the oxygen partial pressure used during a thermal doping process.

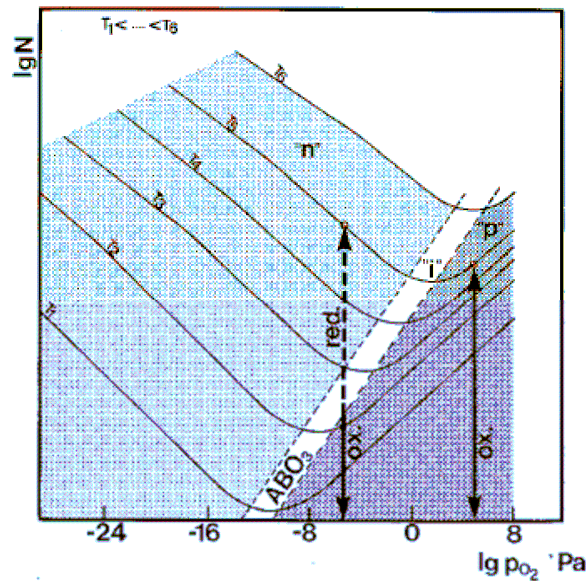


**Figure 16** Chemistry diagram for SrTiO<sub>3</sub> with the concentration of defects (in arbitrary units) versus partial pressure of oxygen in Pa. The arrows denote the effect of in-situ heating and cooling of the samples [39]

Doped STO generally shows a typical metallic behaviour, with the resistivity decreasing as long as the temperature is lowered, with resistance residual ratio (RRR) on the order of more than  $10^3$ , and high low temperature Hall mobility values. In Figure 17 the resistivity vs. temperature behaviour is reported for both Nb-STO and STO<sub>3-δ</sub> [35]. The non-metallic behaviour obtained for too lightly reduced samples, with a carrier concentration on the order of  $10^{17}\text{cm}^{-3}$ , is also shown. *Ab initio* band structure calculations performed by Shanthi and sarma in 1998 [24] explained this metallic behaviour as an almost rigid shift of the Fermi energy toward the conduction band, as reported in Figure 18, where the calculated band structure of stoichiometric SrTiO<sub>3</sub> and reduced SrTiO<sub>2,875</sub>, i.e.  $\delta=0,125$ , are compared.

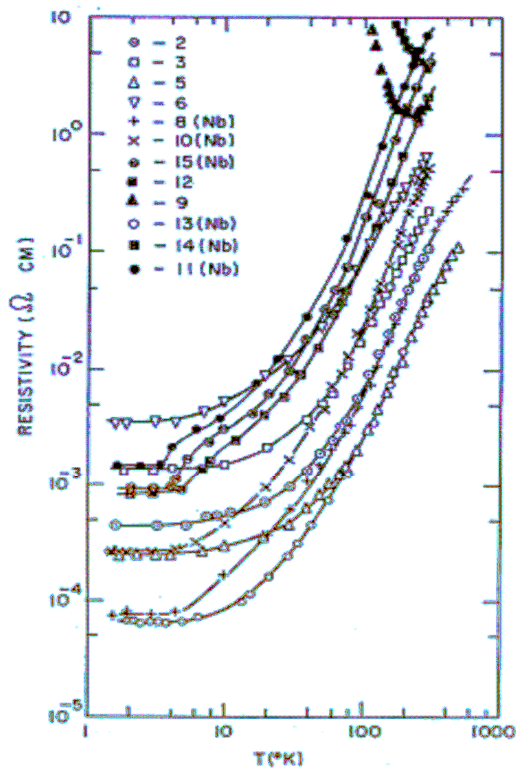


**Figure 17** Temperature dependence of the resistivity for both Nb-doped and reduced SrTiO<sub>3</sub> [35]

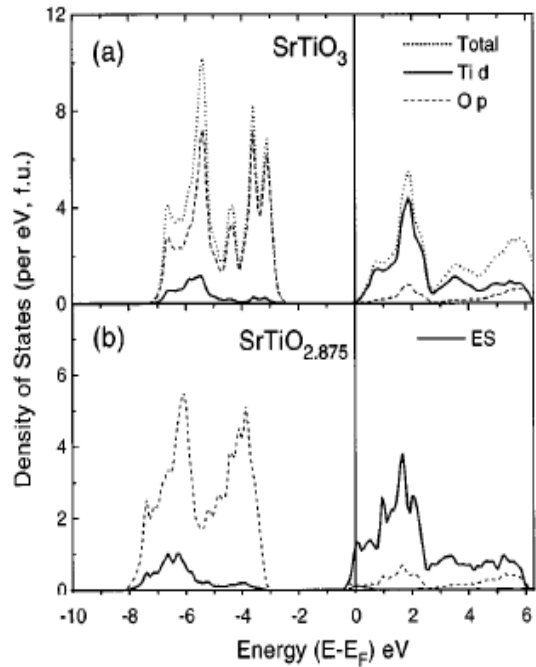


**Figure 18** DOS for stoichiometric STO and reduced STO<sub>2.875</sub>

The carrier concentration were usually obtained by Hall effect measurements, assuming a simple band model for the expression of the Hall coefficient. In Figure 19 the results of such measurements on the same samples whose resistivity is reported in Figure 17, are reported. In the intermediate doping range, the Hall coefficient increases by approximately a factor of 2 between 300 and 100K. This suggest that on oxygen vacancy in SrTiO<sub>3</sub> forms a doubly charged donor center. In the most heavily doped samples, both of the energy levels of the donor center are in the conduction band due to overlap and screening effects, and the Hall coefficient is independent of temperature [35].

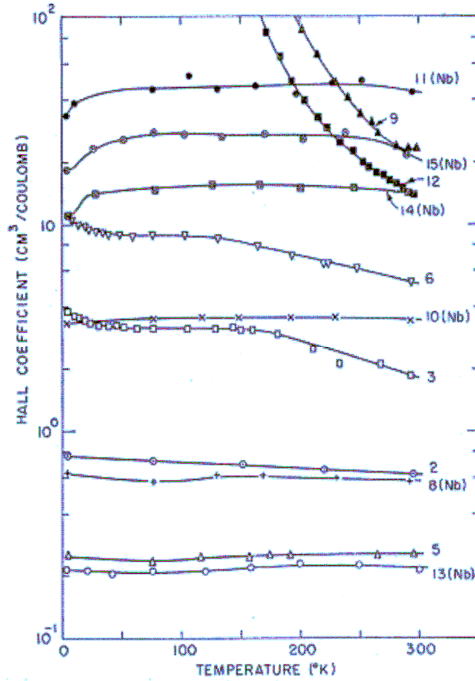


**Figure 19** Temperature dependence of the Hall coefficient for the same samples of Figure 17

It's worth mentioning that after Hall effect measurements the actual role of dopant atoms could be verified. In such a way a different effect of doping obtained by atoms substitution and by oxygen content variation was observed. In case of La substitution, it has been found that there is exactly one delocalized electron doped for every atomic substitution of Sr by La in  $\text{Sr}_{1-x}\text{La}_x\text{TiO}_3$ ; in other words, there are  $x$  number of electrons per Ti site in this series [24]. In Nb-doped STO, Nb atoms go into a Ti site and become  $\text{Nb}^{5+}$  ions, giving up an electron. But only some added Nb doping atoms act as effective donors, the ratio between the latter and the former strongly depending on the growth conditions. This could be explained by considering that Nb may go in a different site, e.g. interstitial or Sr site, with no successful doping effect [33]. Indeed, in the case of oxygen content doping, following the defect chemistry, for each removed oxygen two electrons are expected to become available for the electric conduction, i.e.  $\text{SrTiO}_{3-\delta}$  is expected to have  $2\delta$  number of electrons doped for every formula unit. Hall measurements suggest that there are only  $\delta/2$  number of conduction electrons in  $\text{SrTiO}_3$  for larger values of  $\delta$  ( $\approx 0.28$ ). Thus 75% of the doped electrons do not appear as charge carriers or contribute to the conduction process in such cases. The discrepancy between the number of charge carriers found experimentally, and that expected on the basis of the chemical formula, tend to decrease with decreasing  $\delta$  or nonstoichiometry: increasing  $\delta$  the number of

electrons per unit formula decreases [24]. This is probably due to the clustering of oxygen vacancies, as verified by studying the band structure of  $\text{STO}_{3-\delta}$  samples for different  $\delta$  carried out by Shanthi and Sarma [24]. They show that increasing  $\delta$  vacancy clustering seriously distorts the bottom of the conduction band, making it impossible to describe the evolution of the DOS even approximately within the rigid-band model. Several configurations of the vacancy clustering lead to the formation of localized midgap states in  $\text{SrTiO}_{3-\delta}$ . Thus only a part of the electrons doped contributes to the conduction process, with a sizable portion being trapped by the vacancy clusters.

A feature of doped STO of great technological interest is its high low temperature mobility values that can reach even the order of  $10^4 \text{cm}^2/\text{Vsec}$ , as shown in Figure 20 after [35]. Here, the temperature dependence of the electron mobility is reported. At room temperature the mobility is limited by lattice scattering, while in the temperature range from 150 to 300K, it is very nearly independent of the electron concentration and approximates a powerlaw temperature dependence of the form:

$$\mu_H = 2,9 \times 10^7 T^{-2,7} \text{cm}^2 / \text{V sec} \quad (1.1)$$

Below 150K, the mobility is dependent on the carrier concentration and becomes independent of temperature at low temperatures where the samples become statistically degenerate. The obtained relationship between low temperature mobility values and carrier concentration is reported in Figure 21. Here a clear difference between Nb-doped STO and  $\text{STO}_{3-\delta}$  is also evident: the former presents mobility values a factor of 4 larger than the latter. It's worth to mention the good agreement between the data reported by Tufte [35] and by Frederikse [34] for reduced samples. This agreement leads to consider the relationship between mobility and carrier concentration as a general feature of  $\text{STO}_{3-\delta}$ .

Reduction was achieved by heating the samples at  $900^\circ\text{C}$  or higher in vacuum or large period of time. The samples surfaces were mechanically polished. The reduced samples begin to reoxidize in air at temperatures above 500K giving rise to non reversible increases in the resistivity. However, there is no problem with high-temperature measurements in air on niobium-doped samples [35]

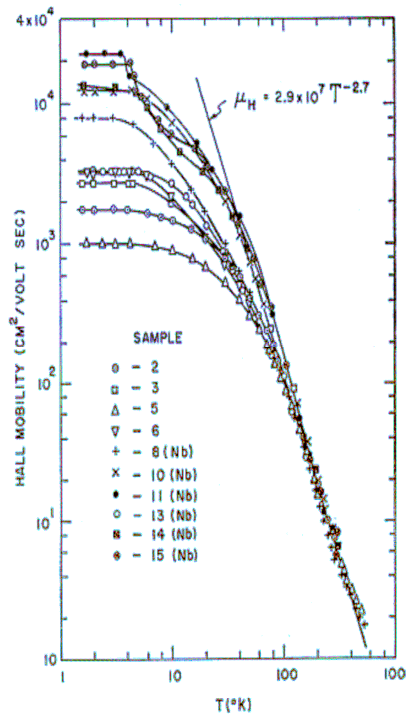


**Figure 20** Temperature dependence of (a) the Hall coefficient and (b) of the mobility for Nb-STO and  $\text{STO}_{3-\delta}$  [35]

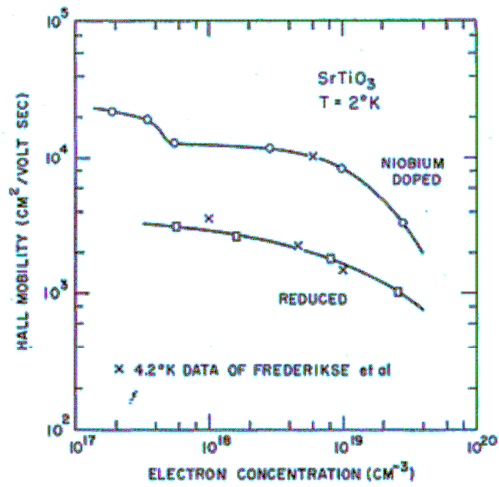


**Figure 21** Relationship between low temperature mobility and carrier concentration for Nb-doped STO and  $\text{STO}_{3-\delta}$ [35]

Doped or reduced STO has also shown a superconducting transition at very low temperatures ( $T_c < 0.3\text{K}$ ), with a dependence of the  $T_c$  similar to that of high temperature superconductors.

Superconducting behaviour was observed in reduced strontium titanate. Extreme type II superconductivity was observed. The reduced samples were prepared from single crystals of  $\text{SrTiO}_3$  and subsequently lapped and cleaned to remove surface material. [36]

The superconducting transition temperature of reduced  $\text{SrTiO}_3$  has been measured as a function of the electronic carrier concentration over three orders of magnitude, i.e. from  $10^{18}$  to  $10^{21}$  carriers/cm<sup>3</sup>. The transition temperature exhibits a maximum ( $T_{cm}=0.3\text{K}$ ) in the range of the carrier concentration investigated at a concentration of about  $10^{20}\text{cm}^{-3}$  [37, 38].

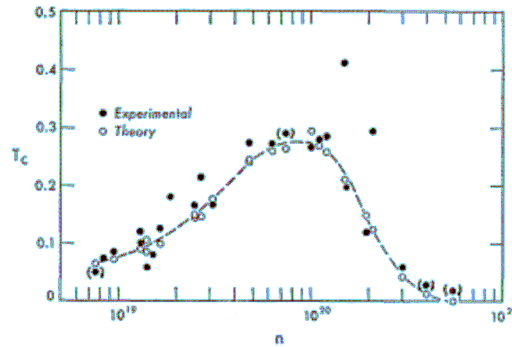


Figure 22 Critical temperature vs. carrier concentration for reduced  $\text{STO}_{3-\delta}$  [38]

The structural character of  $\text{SrTiO}_3$  single crystals allows for a transition to metallic conductivity under reducing conditions which have been hitherto considered to introduce oxygen vacancy defects in the dilute limit and to result in only semiconducting behaviour. However, this metallic state is shown to break down using prolonged reduction as a result of a self-healing phenomenon which decreases dramatically the density of initially introduced vacancy defects and related charge carriers [32]. Moreover the near-surface region of  $\text{SrTiO}_3$  extending several tens of nm into the bulk of material develops chemical inhomogeneities after standard thermal treatment (usually employed as reducing process) and a non-perovskite phase has been observed on its surface [39]. Since the phenomena related with the surface region are of special relevance for the technological application and in particular for the integrability with other perovskite materials, new reducing methods could be investigated. In chapter 3 a new surface reduction technique based on a hydrogen plasma will be illustrated and the transport characteristics of the obtained reduced samples will be discussed. In addition, field effect response of such reduced surfaces will be reported too.

## 2.2. $\text{Nd}_{1.2}\text{Ba}_{1.8}\text{Cu}_3\text{O}_7$

### 2.2.1. High Temperature Superconductors phase diagram and Metal Insulator Transition

As already stressed in the previous chapter, perovskite HTS cuprates, i.e. the  $RE\text{Ba}_2\text{Cu}_3\text{O}_{7-\delta}$  family, are a classical example of strongly correlated systems.  $\text{YBa}_2\text{Cu}_3\text{O}_{7-\delta}$  and  $\text{NdBa}_2\text{Cu}_3\text{O}_{7-\delta}$  are typical examples of such compounds. They present a layered structure, i.e. their cell is formed by three perovskite units superimposed along the  $c$  axis, as shown in Figure 23 [40]. A tetragonal structure ( $a = b \neq c, \alpha = \beta = \gamma = 90^\circ$ ) results.  $c \approx 12\text{\AA}$ ,  $a = b \approx 4\text{\AA}$  are typical axis lengths for such a unit cell. As will be briefly discussed in the following, most of the transport properties of these compounds are governed by the  $\text{CuO}_2$  planes evidenced in Figure 23 where, the Cu atoms are linked with 5 oxygen atoms forming the  $\text{BO}_6$  octahedra discussed in sec. 1.x

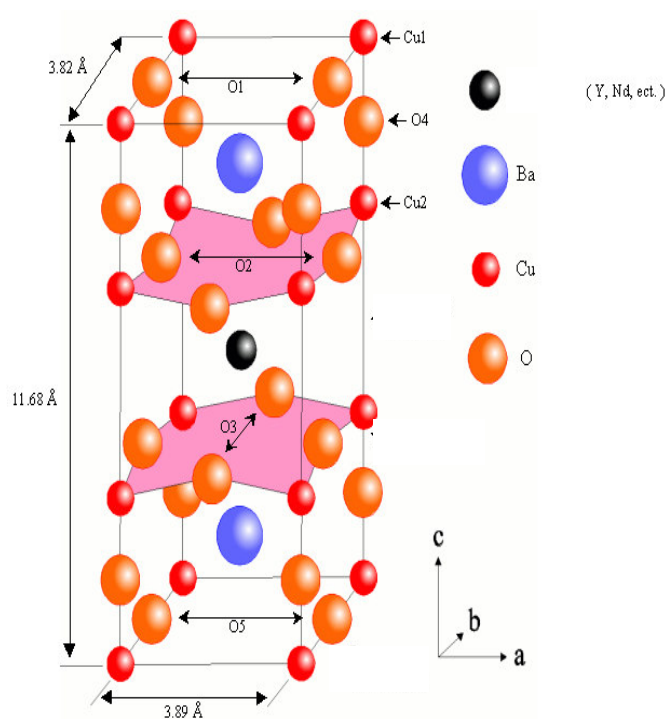


**Figure 23** The unit cell of a perovskite HTS cuprate [40].

It is well known the HTS show an astonishing general phase diagram in which their transport features, and in particular the transition temperature, are reported as a function of the doping level  $x$ , as already mentioned in the first chapter. A general example is reported in Figure 24.

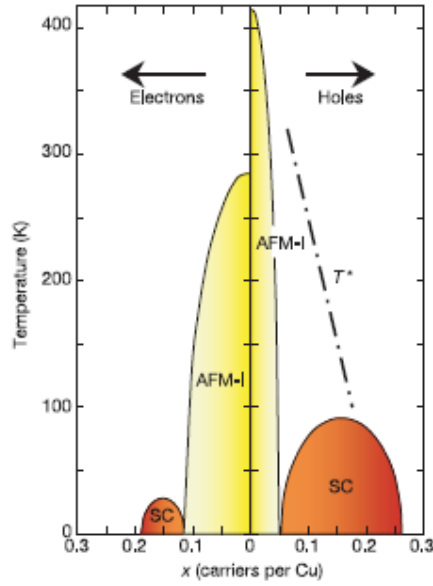


**Figure 24** Phase diagram of the high- $T_c$  superconductors. The electron-doped material represents  $\text{Nd}_{2-x}\text{Ce}_x\text{CuO}_{4-y}$ , and the hole-doped system represents  $\text{YBa}_2\text{Cu}_3\text{O}_{7-\delta}$ . The insulating, antiferromagnetic phases (AFM-I) are drawn in yellow, and the superconducting phases (SC) are in orange [41]

At  $x=0$  the so-called *parent compound* with general formula  $\text{REBa}_2\text{Cu}_3\text{O}_6$  is obtained. Here, in the  $\text{CuO}_2$  planes Cu atoms are characterized by an oxidation  $\text{Cu}^{2+}$ , and present a  $3d^9$  electronic configuration with totally filled 3d orbitals. Under the Neel temperature ( $T_N$ ), a long range antiferromagnetic order arises, i.e. the Cu sites spins are ordered as shown in Figure 26 and the system is insulating (yellow zone). By doping, the compound becomes metallic first and then superconducting. Doping is usually obtained adding extra oxygen atoms ( $\text{REBa}_2\text{Cu}_3\text{O}_{7-\delta}$ ) or by substituting trivalent atoms by bivalent atoms ( $\text{RE}_{1+x}\text{Ba}_{2-x}\text{Cu}_3\text{O}_{7-\delta}$ ). In the former case, the extra oxygens ions attract electrons from the  $\text{CuO}_2$  planes or, that's the same, the  $\text{CuO}_2$  planes gain holes, while in the latter an extra hole is added to the  $\text{CuO}_2$  planes for each atom substituted. In both cases the planes become metallic and at low temperatures the antiferromagnetic order disappears and the superconductivity arises (orange zone). As long as the doping level increases, the transition temperature increases for a while, reaches a maximum at a fixed  $x$  value (optimally doped compound) and then decreases again. The role of doping on the transport features of a  $\text{REBa}_2\text{Cu}_3\text{O}_{7-\delta}$  compound is clearly shown in Figure 25, where the sheet resistance vs. temperature behaviour of  $\text{Y}_y\text{Pr}_{1-y}\text{Ba}_2\text{Cu}_3\text{O}_{7-x}$  is reported as a function of the yttrium content  $y$  [42]. It's worth noticing that the transition occurs when the sheet resistance become less than the quantum resistance  $R_Q = h/4e^2 = 6.45\text{k}\Omega$ .

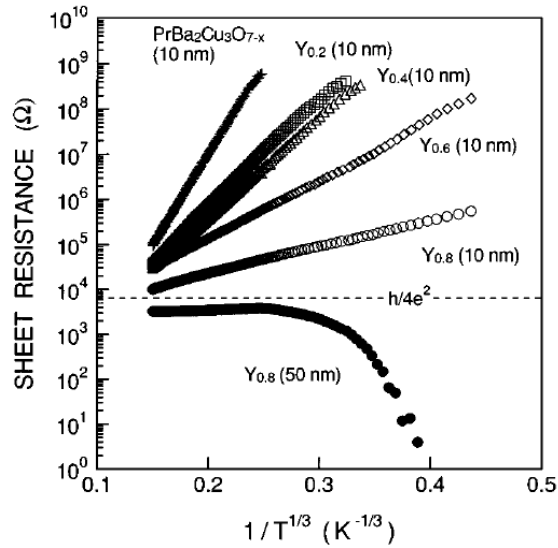


**Figure 25** Temperature dependence of the sheet resistance for  $Y_yPr_{1-y}Ba_2Cu_3O_{7-x}$  ( $y=0$  to  $0.8$ ) thin films [42].

The role of doping in determining the phase transition in cuprates can be understood within the Mott theory and considering the effect of the electronic correlation, as briefly discussed in the following. In crystals, the overlapping of the atomic orbitals leads to the formation of the bands. In TM oxides, and thus in HTS cuprates, the valence and conductance bands width is determined by the overlapping of  $d$  atomic orbitals. Since  $d$  states are localised on a length scale of the same order

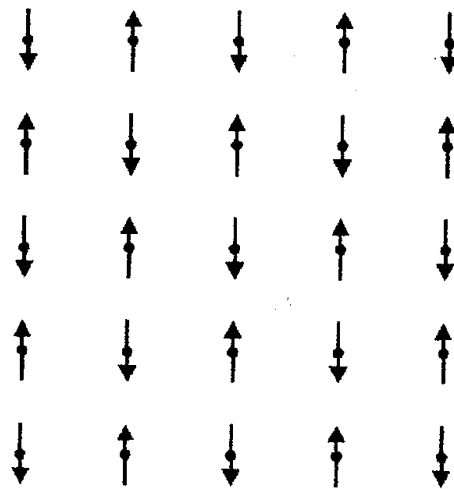


**Figure 26** Spin antiferromagnetic order on Cu site in a  $CuO_2$  plane

of the lattice parameter, the resulting bandwidth is little if compared with the metals bands. Hence, the Coulomb repulsion between same orbital electrons is very strong in this orbitals and its value is relevant if compared with the little bandwidth. In Mott model, if no interaction is considered, a single band arises from the overlap of the  $d$  orbitals and the Fermi energy lies within this band, making the electrical conduction possible. But, the Coulomb repulsion has to be considered and in the Mott theory its effects consists of a band split in two subbands, the higher completely empty and the lower completely filled, as sketched in Figure 27. In this case the system acts as an insulator.

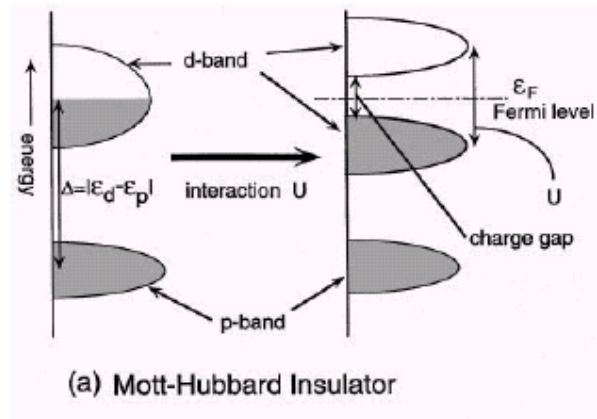


**Figure 27** First the  $d$  band is partially filled and the Fermi energy lies within it; Coulomb repulsion splits the band in two subbands: the higher is completely empty and the lower is completely filled

The Variable Range Hopping (VRH) is the mechanism governing the transport properties of the insulating samples, i.e. electrons can 'jump' between adjacent sites, as schematically sketched in Figure 28. The resistivity versus temperature behaviour for such conduction mechanism can be described as:

$$\rho = \rho_0 \left( \frac{T}{T_0} \right)^{2p} \exp \left( \frac{T_0}{T} \right)^p \quad (1.1)$$

where  $\rho_0$  is a constant,  $p$  is equal to  $1/4$ ,  $1/3$ ,  $1/2$  for 3D-Mott, 2D-Mott and Efros-Schloskii models, and  $T_0$  is a characteristic temperature related to the localization length.

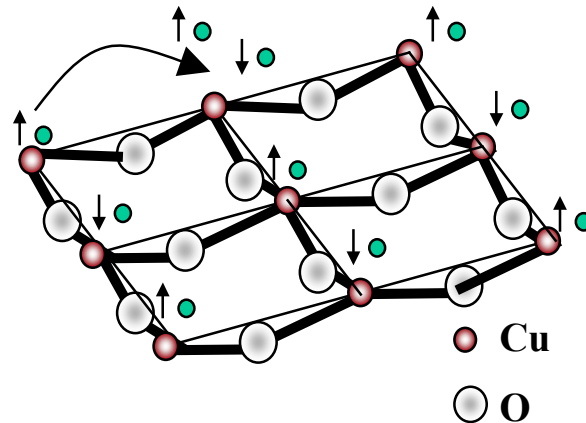


**Figure 28** VRH mechanism in  $\text{CuO}_2$  planes sketch: the arrows indicate the electrons spin

In the Hubbard model for the Mott theory, the metal-insulator transition is governed by the relation between the Coulomb repulsion energy  $U$ , the hopping energy  $t$  and the  $d$  band filling as sketched in Figure 29. In a completely empty ( $n=0$ ) or completely filled ( $n=2$ ) band the system acts as an insulator. But in  $n=1$  case the eventuality of a MIT (metal insulator transition) is governed by the  $U/t$  ratio. In the so-called Bandwidth-Control MIT (BC-MIT) as long as the bandwidth decreases,  $U$  increases and the system becomes insulating. Whereas if the band filling is varied, i.e. the number of electrons is varied for example by doping the compound, a Filling Control MIT (FC-MIT) takes place: the system (for a fixed bandwidth, i.e. for a fixed  $U/t$ ) is a metal until  $n$  reaches  $n=1$ . HTS phase diagrams are clear examples of filling controlled MIT.

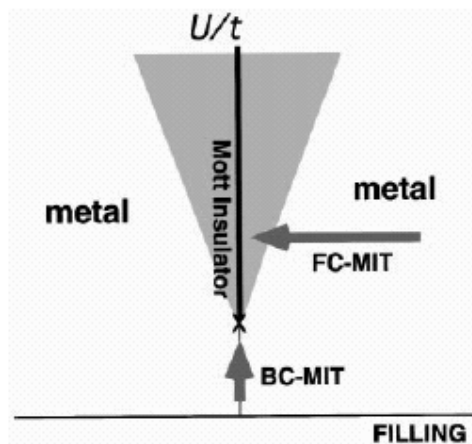


**Figure 29** Hubbard model for Metal-insulator phase diagram; shaded region represent the Mott insulating phase

### 2.2.2. $\text{Nd}_{1.2}\text{Ba}_{1.8}\text{Cu}_3\text{O}_7$ thin films: structural and transport properties

In this section the structural and transport properties of NBCO thin films, on which field effect experiments have been performed, are discussed.

As already stressed in sect. 1.x, very thin films with very flat surfaces must be employed in field effect experiments. But superconducting features in very thin cuprates epitaxial films are strongly influenced by the film structure and thickness. If a sample thickness is decreased reaching few u.c., mismatch (disuniformity) at the interface between the film and the substrate can seriously modify the film structure resulting in strain phenomena. The latter can modify the sample transport features and even its transition temperature.  $\text{Nd}_{1.2}\text{Ba}_{1.8}\text{Cu}_3\text{O}_7$  films used as channels in this work were deposited on STO (100) single crystals using the high oxygen pressure diode sputtering from a single target substrates. The substrates were etched in order to clean and reconstruct the terrace structure. The deposition consisted of three phases: pre-sputtering, in which a Ar- $\text{O}_2$  mix cleans the target surface with no material deposition; the actual deposition at high temperature (about  $900^\circ\text{C}$ ) ; the annealing, by which the deposited film is oxygenated: in this way the obtained tetragonal phase can be turned in the orthorhombic and superconductive one. The main deposition parameters are reported in Table 1. X-rays diffraction measurements on a 120nm thick film (bulk sample) show the good alignment between the NBCO film and the STO substrate and the epitaxial growth of the film (Figure 30).

	$\Phi(\text{O}_2)$ [slm]	$\Phi(\text{Ar})$ [sccm]	I [mA]	V [V]
Presputtering	6.38	10.0	150	286
Sputtering	6.90	10.0	150	279

**Table 1** Main parameters values for the  $\text{Nd}_{1.2}\text{Ba}_{1.8}\text{Cu}_3\text{O}_7$  deposition

The good surface quality of the deposited films was checked by AFM measurements: the results show the typical terrace structure with a maximum roughness of two u.c. on a 120nm thick film. The actual film thickness has been determined by Bragg diffraction measurements. AFM measurements were performed on a 8u.c. thick film too. They prove the good surface flatness with a 1u.c. maximum roughness. The results are reported in Figure 31.

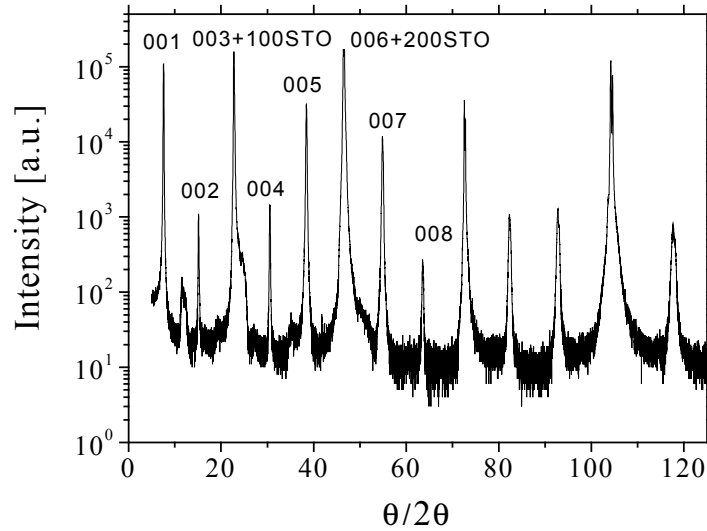


**Figure 30** X-rays analysis of a 120nm thick sample: the correspondence between the (0,0,n) NBCO peaks and the (0,0,l) STO substrate peaks prove the good epitaxial growth of the film.

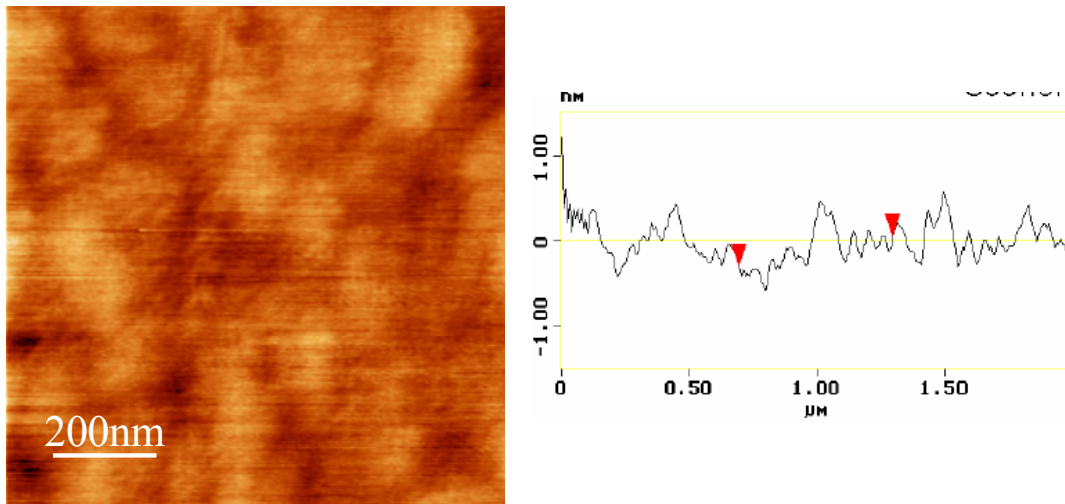


**Figure 31** (a)AFM image and (b) roughness profile on a 8u.c. thick sample

The transport features of the deposited  $\text{Nd}_{1.2}\text{Ba}_{1.8}\text{Cu}_3\text{O}_7$  films were characterized in term of resistivity vs. temperature behaviour. The measurements have been carried out by a conventional four-probe technique. As shown in Figure 32(a), it's evident the influence of the film thickness on the  $\rho(T)$  behaviour. 110u.c. thick films are characterized by a critical temperature of 63–65 K. These samples are on the underdoped side of the phase diagram. As long as the thickness decreases, the transition temperature decreases too and for thickness lower than 8u.c. film show a typical insulating behaviour. In Figure 32(b) it's shown that for these samples too the superconducting

transition occurs when the sheet resistance is lower than the quantum sheet unit  $R_Q$ , as reported for YPrBCO in Figure 25.

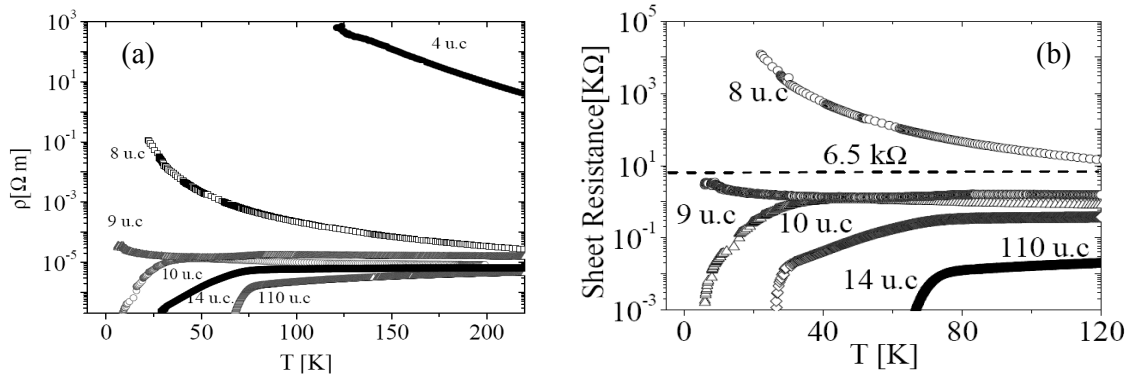


**Figure 32** (a)Resistivity and (b)sheet resistance temperature behaviour as a function of the films thickness. In (b) the quantum resistance unit is shown as reference.

So, a relation between film thickness and carrier concentration can be thought. In particular the carrier concentration seems decreasing as long as the film thickness decreases. Seebeck effect experiments were performed on some selected samples in order to gain information about the possible changes in the number of holes per  $CuO_2$  plane as a function of the thickness. In fact it is well known that the Seebeck effect in high  $T_c$  cuprates is related to the number of holes per  $CuO_2$  plane,  $p_{pl}$ , independent from the analyzed compound. In particular, the absolute value of  $S(T)$  exhibits a strong systematic decrease with  $p_{pl}$ : the room temperature value  $S_{290}$ , that is a convenient parameter, falls nearly exponentially with the number of holes. Many cuprates, despite the different combinations of constituent atoms, stoichiometries, and number of  $CuO_2$  superconducting layers, follow this general trend so closely that a universal correlation between  $S$  and  $p_{pl}$  was established by Orbetelli *et al.* 24

The  $S$  versus  $T$  plots as a function of different film thickness are reported in Figure 33. The absolute value of the Seebeck effect increases as the film thickness decreases This suggests that by decreasing the film thickness the number of holes per  $CuO_2$  planes progressively diminishes.

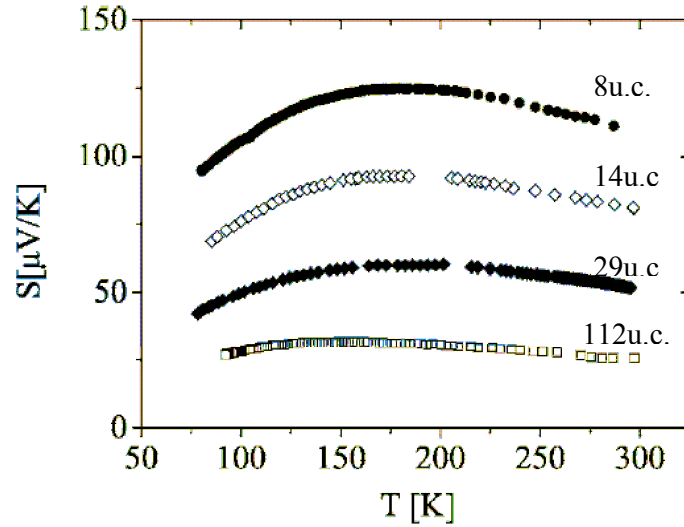


**Figure 33** The measured temperature dependence of the Seebeck effect coefficient for different thickness samples []

Employing phenomenological expression reported in [], the number of holes per  $\text{CuO}_2$  planes have been evaluated for the samples characterized by Seebeck effect measurements. The result are shown in Figure 34 where the position on the  $\text{Nd}_{1.2}\text{Ba}_{1.8}\text{Cu}_3\text{O}_7$  phase diagram is reported. For the 112 u.c. film,  $p_{\text{pl}}$  is 0.097, on the underdoped side of phase diagram. Then, at decreasing thickness,  $p_{\text{pl}}$  diminishes down to 0.065 for the 14u.c. film. For the 8 u.c. film,  $p_{\text{pl}}$  is about 0.045, that is in agreement with the Mott-insulating behavior of the resistivity.

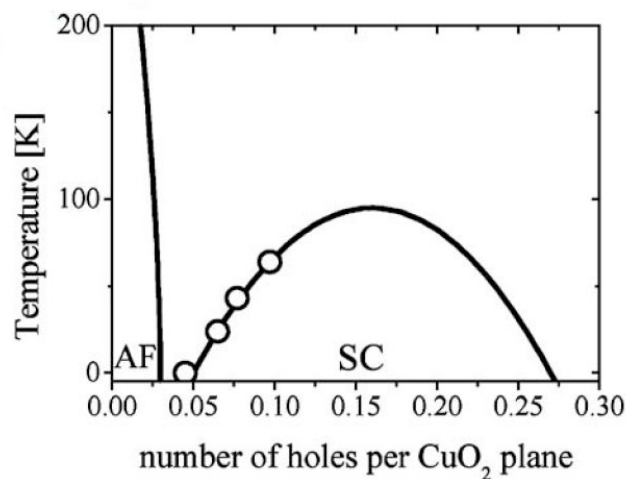


**Figure 34** Evaluated holes per  $\text{CuO}_2$  plane in different thickness  $\text{Nd}_{1.2}\text{Ba}_{1.8}\text{Cu}_3\text{O}_7$  films []

Hence,  $\text{Nd}_{1.2}\text{Ba}_{1.8}\text{Cu}_3\text{O}_7$  thin films seem to be ideal candidates for field-effect experiments on HTS cuprates thanks to the matching of crucial parameters highlighted in the first chapter. Indeed, they

show structural match with STO substrates that can be used as gate insulator; a very good surface flatness that allows a good interface with a possible insulating layer deposited on them; a low carrier concentration consenting to observe huge field effect. In chapter 4 the realization of a device exploiting  $\text{Nd}_{1.2}\text{Ba}_{1.8}\text{Cu}_3\text{O}_7$  thin films as channels and the results of field effect experiments on it will be reported.



## Chapter 3

### Field Effect on reduced STO surfaces

In this chapter the results of field effect experiments on  $\text{SrTiO}_{3-\delta}$  hydrogen plasma reduced surfaces are reported. This activity has been run at the *Département de Physique de la Matière Condensée* in Geneva, where I was guest of the prof. Triscone's group. After a brief description of the instrumental apparatus utilised (sec. 3.1), the working principle of the hydrogen plasma reduction procedure and the realization of the devices to investigate are discussed (sec. 3.2 and 3.3). Then the results of the characterization of the obtained reduced surfaces are reported in term of  $R(T)$  behaviour, Hall effect and magnetoresistance measurements (sec. 3.4) and Field Effect experiments (sec. 3.5). Finally, in order to verify the actual effect of the transversal field on the  $\text{STO}_{3-\delta}$  charge carriers, simultaneous Hall effect and Field effect measurements results are shown too (sec. 3.6).

#### 3.1. Experimental apparatus in Geneva

In Geneva two measurements set-up were available: dielectric and field-effect measurements apparatus and a Hall effect equipment. They're described in the following.

##### 3.1.1. Hall effect measurements system

The Hall effect equipment consists of a dewar where a magnetic field can be applied, the related controllers, all provided by Oxford Instruments, and the electric measurement instrumentations, as shown in Figure 35.

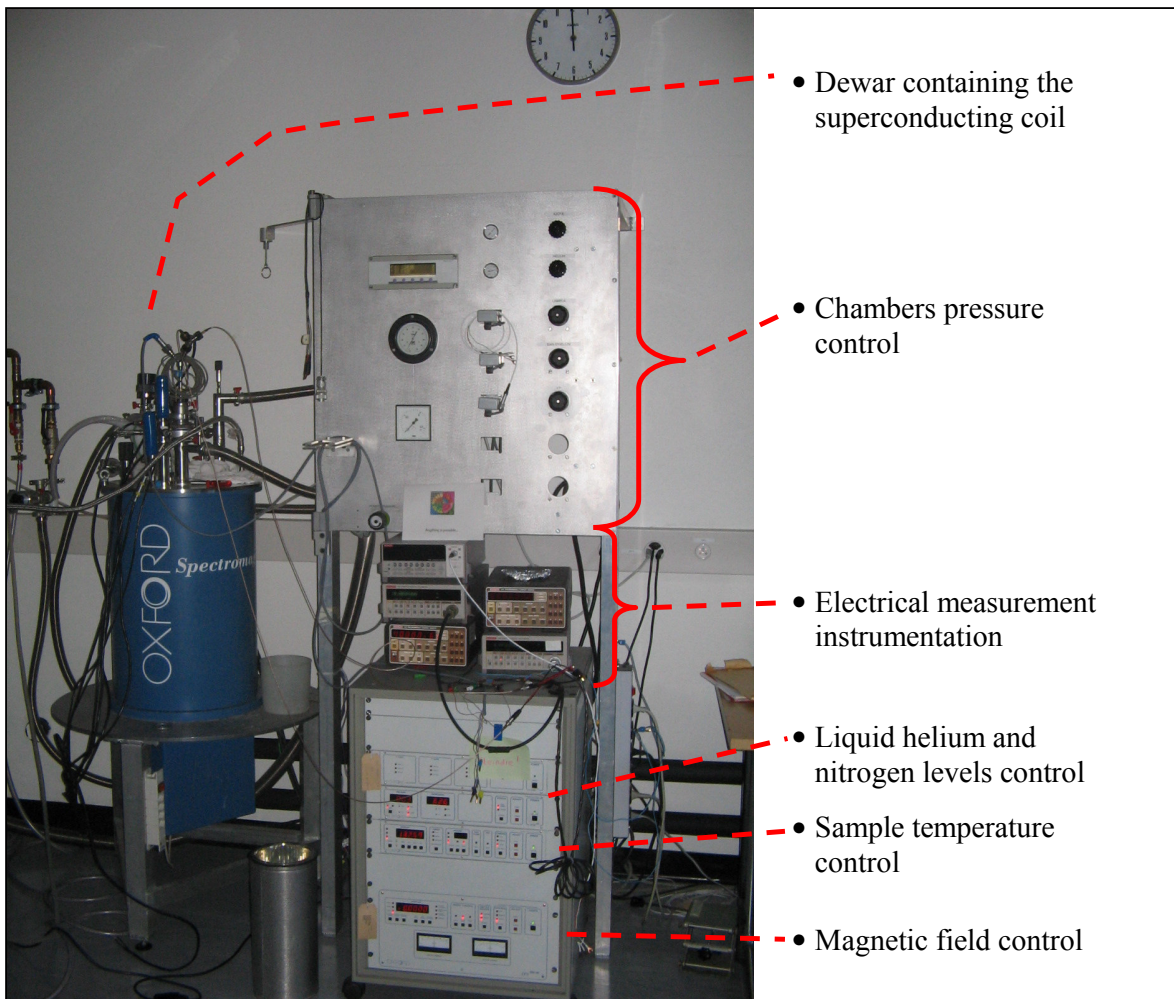


**Figure 35** The Hall effect measurement equipment: the dewar containing the superconducting magnet is shown on the left side, while on the right side the dewar chambers pressure control, the electric measurements instrumentation and the temperature and magnet controllers are shown.

In the dewar, the magnetic field it's applied by a superconducting coil dipped in a liquid helium bath. In order to achieve a good thermal isolation between the helium bath and the external environment, the system consists of 5 chambers, as schematically shown in Figure 36. From the external to the inner one there are a vacuum chamber, a liquid nitrogen bath, another vacuum chamber and finally the helium liquid bath in which the superconducting coil is dipped. The samples are placed in the magnetic field by introducing a sample holder in a further chamber. The latter is linked to the liquid helium bath via a valve, whose behaviour is described below.

The control system is composed of three elements and allows controlling the cryogenics liquids levels, the sample temperature and the magnetic field strength. The cryogenics liquids levels are monitored by a resistance sensor for the helium and a capacitance sensor for the nitrogen. For the latter an automatic refilling procedure from an external dewar starts when the nitrogen level is

found lower than a fixed value. The system allows fixing the sample temperature thanks to a heater resistance placed within the sample holder and the valve above-mentioned that controls a helium gas flux from the helium bath. Both the heater and the gas flux can be controlled on the temperature control panel manually or automatically if a temperature value is fixed to be reached. The temperature stability is guaranteed with an accuracy of the one per thousand.

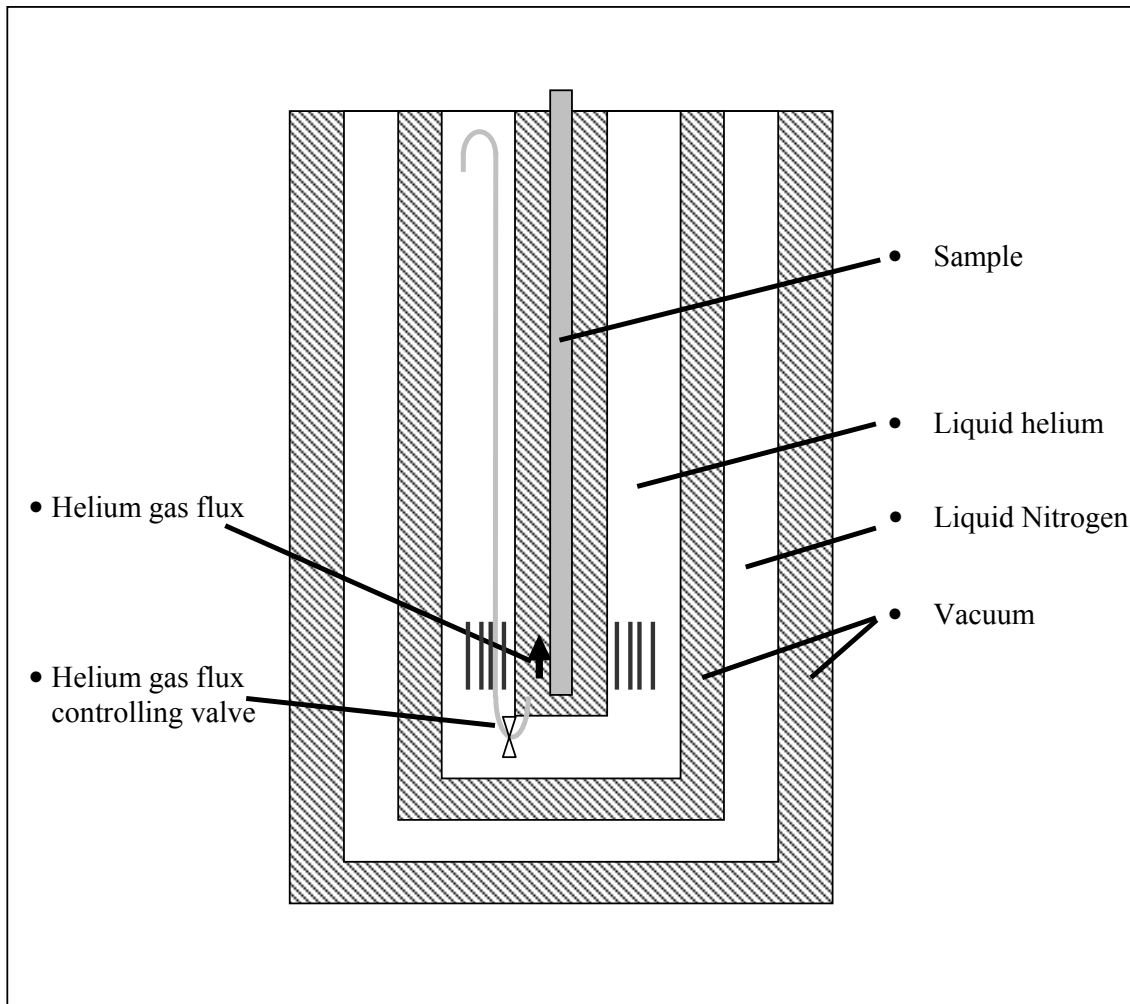


**Figure 36** Schematic cross-section view of the dewar containing the superconducting coil.

The Hall effect measurements related instrumentation consists of a current supplier and a voltmeter, both provided by Keithley. In order to achieve information on the effect of the applied transverse field on the channel carriers concentration and mobility, a Keithley source-meter has been added to apply the gate voltage and monitor the leakage current within the gate insulator.

Even if the described system allows achieving a maximum field of 9 Teslas, only a 4 Teslas maximum field has been utilized in our measurements. Thanks to the above-mentioned features,

this system has been utilized to perform Hall effect and magnetoresistance measurement on samples at different fixed temperatures.

The measurements have been performed with a classical four probes technique remote controlled by a LabView software, which allowed to control the flowing current value, the magnetic field strength, the sample temperature and even its stability, as better described in next sections.

### **3.1.2. Dielectric and field effect measurements equipment**

The dielectric and field-effect measurement station consists of an LCR-meter, a voltage supplier (KEPCOO), a temperature controller, a current supplier (Keithley) and a voltmeter (Keithley), as shown in Figure 37. In order to obtain information about the leakage currents through the gate insulator, even the Keithley source-meter has been sometimes utilized here.

The LCR meter has been utilized to measuring the capacitance of the gate insulator. Even if this instrument allows setting the excitation amplitude and frequency, we always performed these measurements by applying a 1V and 1kHz excitation signal. The combination of this instrument with the voltage supplier allows performing capacitance measurements at different applied gate voltages, with a maximum of 200V.

The field effect measurements have been performed by applying the gate voltage by the Keepco supplier. The latter is actually a power supply, but we were able to limit its current output and so to avoid leakage current through the gate insulator. Unfortunately, the minimum current we could monitor was on the order of the microampere, well above the required nanoampere sensitivity required for the leakage currents observation. In order to enhance this feature, the Keithley sourcemeter mentioned in the previous section has been sometimes used on this station too: in this way any leakage currents could be monitored during the measurements with an accuracy of the order of the tenth of nanoampere.

Here also the measurements have been performed with a four probes technique, with the current provided by the Keithley current supplier and the voltage signal measured by the Keithley voltmeter.

The sample temperature was monitored by a Lakeshore temperature controller, which ensures an accuracy of the hundredth of degree. Unfortunately, the temperature stability was not ensured by remote controlling feedback.

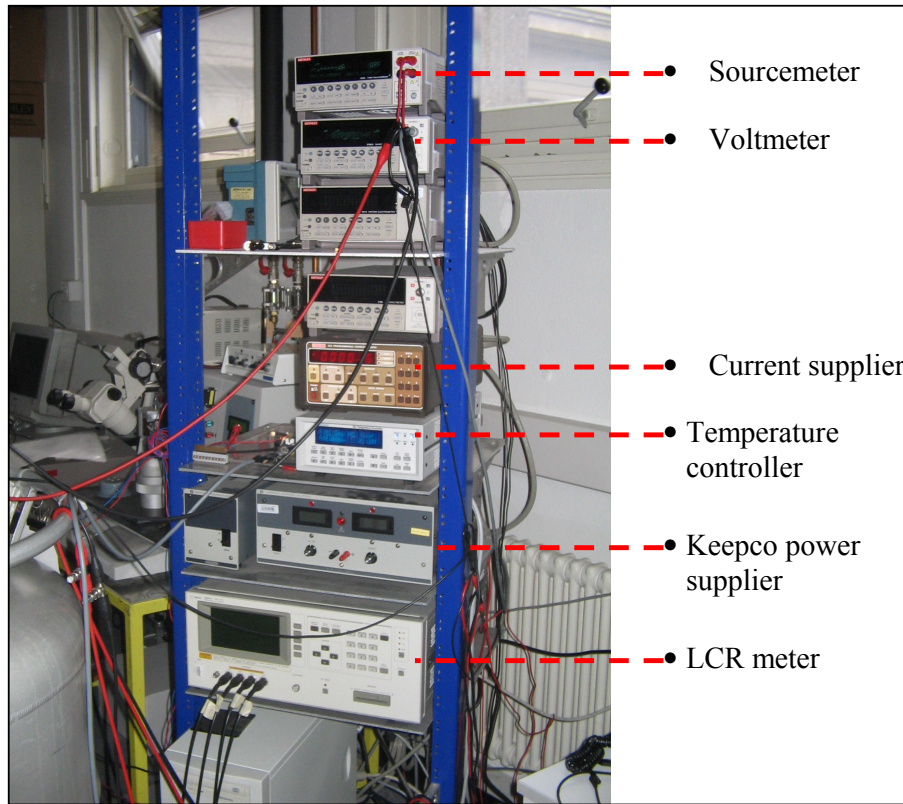


**Figure 37** Dielectric and field effect measurements apparatus

### 3.2. Hydrogen Plasma reduction

The idea behind the utilization of the plasma is the creation of a very reactive gas environment, often enclosed in a vacuum system. Surfaces in contact with the plasma experience interactions which may result in sputtering (momentum transfer to surface atoms), chemical reactions caused by highly reactive radicals, low-energy ions and electrons created in the plasma and desorption due to heating by the impingement of particles (e.g. recombination processes or electron bombardment).

Plasma cleaning, employing hydrogen as reactive gas, has been used for many years. Hydrogen discharge cleaning of vacuum vessels for particle accelerators and magnetic fusion devices is a well-known technique in the field of nuclear and particle physics for the removal of light impurities from stainless steel and other metallic materials. The restoration and conservation of archaeological artefacts, the removal of the oxide layer from the liquid solder surface in flip-chip solder bonding and the substitution of flux for soldering electronic boards are other applications. Thin film and semiconductor technologies are other potential areas for hydrogen plasma cleaning. In silicon technology, in particular, cleaning procedures that lead to ultraclean surfaces, lowering the thermal

budget of the wafer and reducing the bombarding energy of particles involved in plasma processing, are challenges for the production of advanced semiconductor devices. The plasma was also used to remove native oxide and hydrocarbons from the wafer surface at temperature between 100 and 400°C [43].

In this work, the hydrogen plasma has been employed to remove superficial oxygen ions on STO commercial substrates: in this way oxygen vacancies are introduced into the STO lattice obtaining a  $\text{STO}_{3-\delta}$  layer on the surface of the STO crystals themselves with no atom substitution and with no thermal treatment. This “cleaning effect” is essentially obtained by chemical reactions between the substrate surface and hydrogen (plasma chemical cleaning).

The employed system, shown in Figure 38, is based on a low-energy argon-hydrogen gas discharge (d.c. type, hot filament). Since the process has been performed in an ultra-high vacuum environment, an additional load lock (1) was necessary to allow substrate transfer to the cleaning module (2) without breaking the vacuum. The module contained a substrate holder (3), which was usually grounded. The plasma source (4) consisted of a heated filament (5) placed in a separate cavity (6). An orifice connected the cavity to the chamber; the working gas, argon, and the reactive gas (hydrogen) were fed into the cavity at (7).

The hydrogen gas was provided by the apparatus shown in Figure 38(c): starting from deionised water, an electrochemical reaction takes place, producing hydrogen and oxygen gases; the latter was discharged in the environment, while the former was collected and provided to the plasma chamber at a selectable fixed pressure.

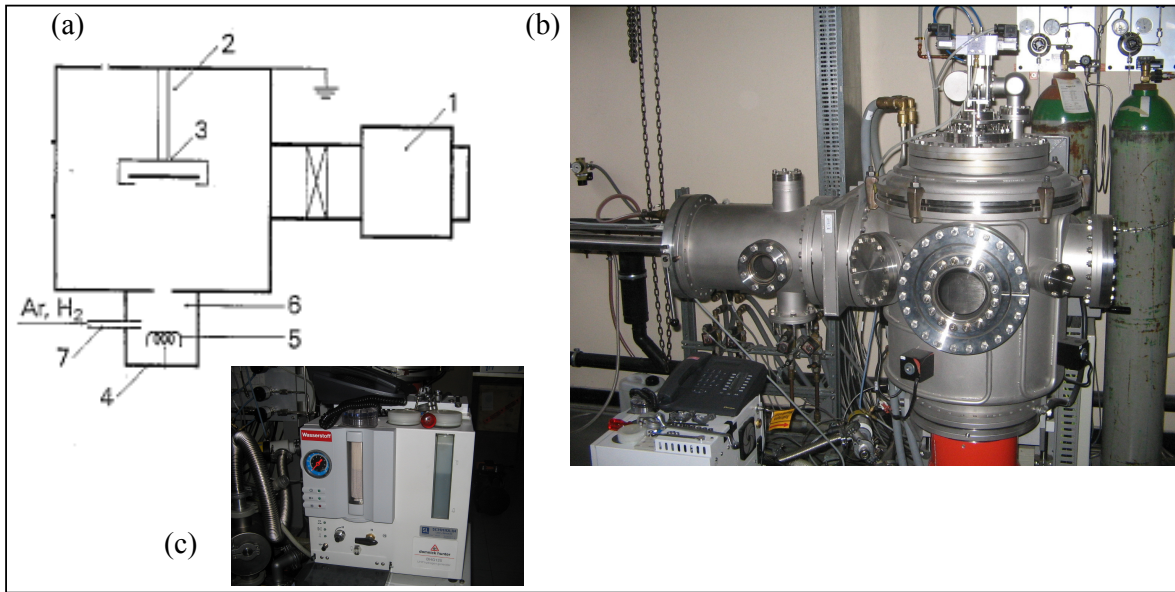


**Figure 38** The hydrogen plasma system: (a) schematic layout (see text for more details) and (b) the employed system; in (c) the hydrogen gas provider is also shown.

The gas discharge was established by applying a potential between the heated filament and ground. For voltages of 20-30 V, electron currents between 10 and 100A were obtained. The ion current increases with the discharge current and the ratio between  $\text{ArH}^+$  and  $\text{H}_3^+$  changes, as shown in Figure 39. The ion mass spectrum at a discharge of 20A is also shown in the inset of Figure 39: the dominant peak is  $m/e=41$ , which is attributed to  $\text{ArH}^+$ .  $\text{H}_3^+$  is less intense and only a very small amount of  $\text{H}_2^+$  is detected.  $\text{H}^+$  is also detectable and increases for higher discharge currents [43].

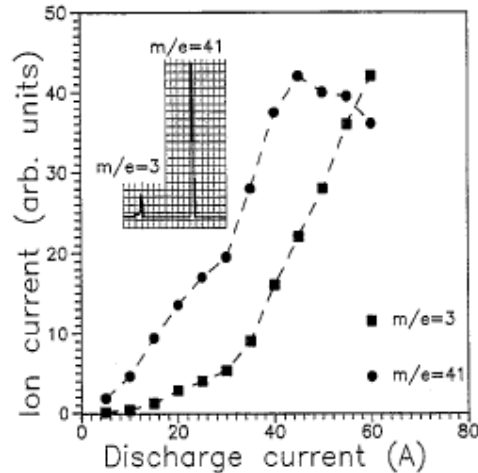


**Figure 39** The positive ions current as a function of the discharge current. In the inset the ion spectrum at a discharge current of 20A is shown

The whole cleaning procedure consisted of substrate exposure to the plasma for only a few minutes. Volatile hydrogen compounds are formed during the cleaning procedure and pumped away. The etch rates could be increased by increasing the discharge current. However, higher discharge currents promote the incorporation of hydrogen into the substrate [43], which may results in dielectric loss peaks [44].

Finally, it's worth noticing that while the usual thermal treatment introduces non-perovskite phases at the substrate surface [45], the STO reducing plasma cleaning technique doesn't affect the lattice structure [46].

### 3.3. Device

The reduced STO surfaces were obtained on STO commercially available single crystals. Both  $500\mu\text{m}$  and  $100\mu\text{m}$  thick crystals have been utilised: in particular the latter have been employed in field effect experiments.

The procedure followed to obtain the final devices starting from the single crystals is schematically shown in Figure 40. A standard photolithographic technique has been utilized to realize a four-probe technique path on the surface of the STO crystals (1,2). A negative mask has been used so, after the developing step of the photolithographic process, only the desired path results photoresist-free. In this way only this path will be interested by the plasma cleaning procedure (3), which removes oxygen ions from the crystals surface thanks to the reaction of the  $\text{ArH}^+$  and  $\text{H}^{3+}$  species present in the plasma with the surfaces themselves. After the plasma reduction, the crystals are dipped in an acetone bath in order to remove the residual photoresist layer. The final device is shown in (4), while in (5) a cross-sectional view of a field effect device is shown. The final devices were then bonded by a wire-bonding machine.

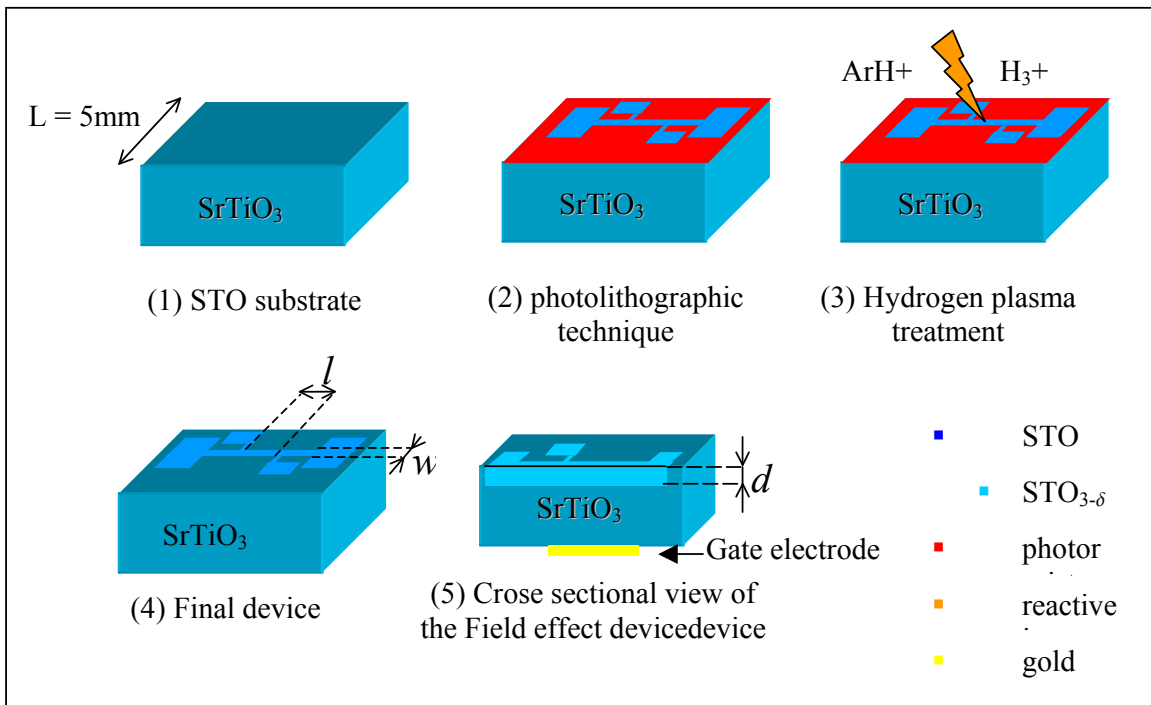


**Figure 40** Procedure to obtain the final  $\text{STO}_{3-\delta}$ -STO single crystal device

Unfortunately the thickness  $d$  of the actually reduced region is a priori unknown, but an estimation has been carried out by the Hall effect measurements, as described in the following sections.

Several samples have been reduced by the method described. The discharge voltage and current have been maintained fixed at 25V and 50A, respectively: in this way the discharge energy is low enough to ensure only chemical reactions take place on the samples surface, with no sputtering

phenomena, as stressed above. The plasma conditions, such as the hydrogen, argon and nitrogen fluxes and the exposure time, were varied for different samples, as summarised in Table 1. There, even the measured chamber total pressure is reported.

sample	sample	H <sub>2</sub> flux [sccm]	Ar flux [sccm]	N <sub>2</sub> flux [sccm]	p [mbar]	time [min]
B	H141004	26,20	25,2	1324	6,3 E-3	5,00
D	H081104	26,20	25	1322	6,3 E-3	5,00
I	H260105	50,0	25,2	1322	8,7 E-3	5,00
L	H270105	26,2	57,7	1322	1,2 E-2	5,00
O	H100205	50,0	57,5	1322	11,5 E-2	5,00
P	H210205	26,2	25	1322	6,3 E-3	5,00
Q	H220205	49,1	60,1	1322	1,6 E-2	10,00

**Table 2** Hydrogen plasma parameters for different realized and characterized devices

### 3.4. Characterization

In order to perform measurements on the reduced surfaces obtained, the samples have been fixed on plastic chips with gold pads. The electric contact between the chip and the surfaces has been realized by wire-bonding technique, that is aluminium thin wires have been soldered by ultrasonic vibrations between the gold pads on the chips and the reduced islands obtained on the samples surface. All the samples had shown a several dozens k $\Omega$  contact resistances (ranging from 20 to even 70k). The contacts with the wires linked with the instrumentations have been realized by soldering the wires ends on the gold pads on the chips.

The samples have been characterized in term of R(T) behaviour, Hall effect and magnetoresistance effect in the Hall effect equipment shown in Figure 35. By these measurements, informations about the carrier mobility and the reduced region thickness have been carried out. Finally field effect measurements have been performed and then, in order to achieve information about the actual effect of the transverse field on the carrier features, such as concentration and mobility, Hall effect and field effect measurements have been performed at the same time.

### 3.4.1. R (T)

The samples described above have been characterized in term of resistance versus temperature first. The resistance has been measured by the standard four probe technique, with a fixed current of  $10\mu\text{A}$  flowing in the photolithographically patterned path. The current inversion method has been employed in order to eliminate spurious thermoelectric effects on the voltage signals.

The reduced STO regions show, as expected, a metallic behaviour. In Figure 41(a) the measured typical behaviour is reported for sample H141004. In this figure, repeated R(T) measurements are shown to introduce another common feature of our samples: the high temperature resistance increases as long as time flows. More in detail, Figure 41(a) shows the R(T) behaviour for sample H141004 after 24, 96 and 288 hours. One possible explanation could be the absorption of environmental oxygen on the samples surface, but the observation of the same increase of the room temperature resistance in an helium controlled atmosphere, shown in Figure 41(b) for sample H081104 at  $T=296\text{K}$ , leads to discard this possibility or, at least, to consider other mechanisms as major responsible of this increase. Actually, since between the reduced surface region and the STO substrate there are no physical barriers, the diffusion of the surface induced oxygen vacancies toward deeper layers of the STO samples could be thought as the explanation of this phenomenon.

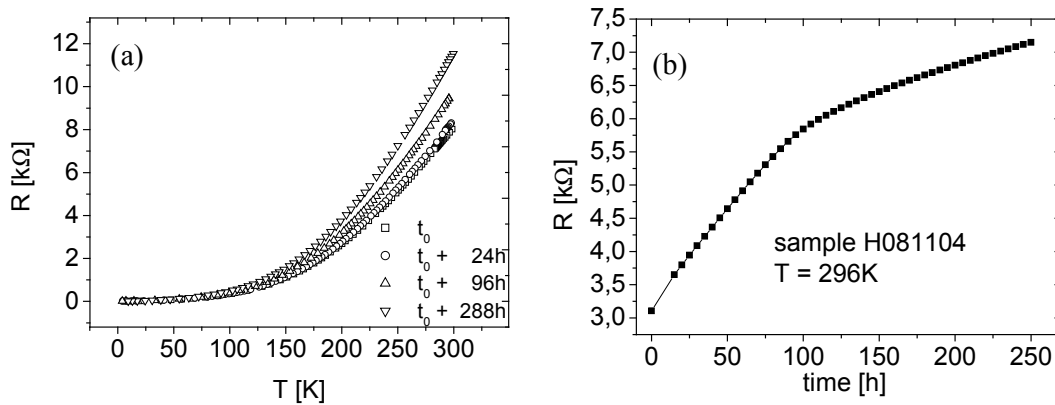


**Figure 41** Typical resistance vs. temperature behaviour of hydrogen plasma reduced  $\text{STO}_{3-\delta}$  surfaces: (a) different R(T) curves obtained at different measurement times are shown for sample H141004; (b) the room temperature resistance increase vs. time for sample H081104 in a helium atmosphere

Since the thickness of the reduced regions obtained by the plasma cleaning is unknown, as already highlighted in previous section, a comparison between resistivities of samples obtained with different plasma conditions is not suitable.

It's worth noticing that the different  $R(T,t)$  curves observed at different times all overlap if normalized in the  $\rho(T)/\rho(296K)$  way, as shown in Figure 42(a). Again, even if different samples  $R(T)$  curves are normalized in such a way, they also overlap for a large temperature range, as shown in Figure 42(b). Only at low temperatures light differences are observable, as a signature of different residual resistivity due to the different defects amounts introduced by the different amounts of the oxygen vacancies induced by the plasma treatment.

The good metallicity of our samples is also visible by considering their Residual Resistivity Ratio, on the order of  $10^3$  as deducible after the normalized resistivity curves in Figure 42. These results are in good quantitative agreement with those reported in [47, 48] for thermally reduced  $STO_{3-\delta}$ .

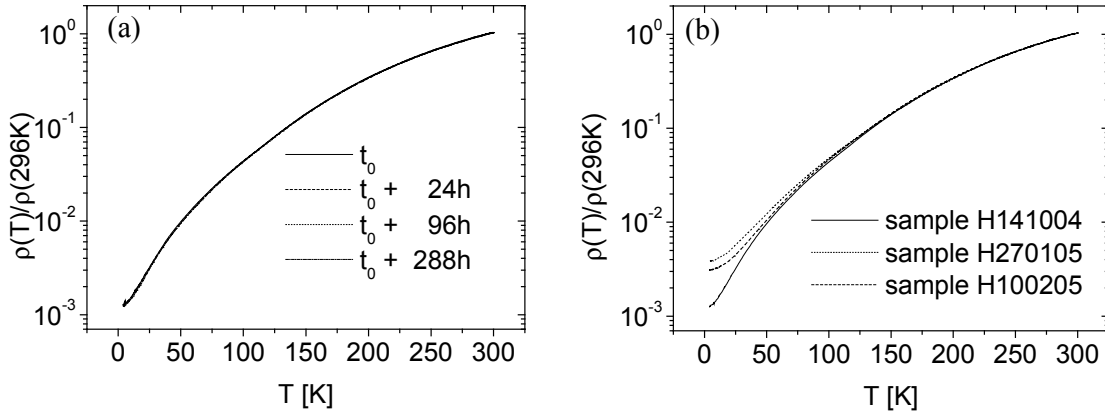


**Figure 42**  $\rho(T)/\rho(296K)$  normalized curves for (a) the same curves shown in Figure 41, all obtained on sample H141004 and (b) for samples reduced with different plasma conditions (see Table 2).

### 3.4.2. Magnetic measurements: Hall effect and magnetoresistance

After the  $R(T)$  behaviour verification, magnetic measurements at different temperatures have been performed on our samples in the Oxford system described in section 3.1. We were able to carry out Hall effect and magnetoresistance results at the same time, by employing the procedure described in the following. The samples, fixed on the same chips described in the previous section, have been placed on the system sample holder and then introduced in the dewar. In this way the magnetic field results applied to the sample in a perpendicular way.

For each selected temperature, whose stability was ensured by the temperature controller, the magnetic field has been spanned starting from 0T to a maximum of 4T, then from 4T to  $-4T$  and

finally from  $-4T$  to  $0T$  again, with a number of field steps controlled by a LabView controlling software. At each magnetic field step, a four-probe resistance measurement, the same utilized for the  $R(T)$  measurements, has been performed. Since the measured voltage contains together the Hall and the magnetoresistance effects related signals, a symmetrization and anti-symmetrization procedure has been applied. More in detail, assuming an even and odd behaviour as a function of the magnetic field for the magnetoresistance and the Hall effect signal respectively:

$$\begin{aligned} V_{MR}(B) &= \frac{V(B) + V(-B)}{2} \\ V_H(B) &= \frac{V(B) - V(-B)}{2} \end{aligned} \quad (3.1)$$

where  $V(B)$  is the measured voltage as a function of the magnetic field,  $V_H$  is the Hall effect voltage and  $V_{MR}$  is the magnetoresistance effect related voltage. In Figure 43 an example of such a derivation is shown: in particular the measured voltage  $V$ , the related magnetoresistance  $V_{MR}$  and Hall effect  $V_H$  signals for sample H260105 at  $T=5K$  are reported.

In the following subsections the results of this analysis on the samples of Table 2 are reported.

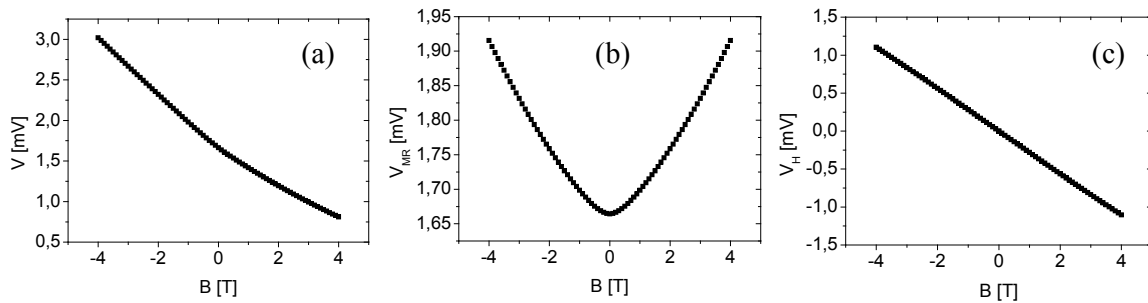


**Figure 43** An example of the results obtained by following the method described by the (3.1): starting from (a) the voltage  $V$  measured as a function of the applied magnetic field the magnetoresistance  $V_{MR}$  (b) and the Hall effect  $V_H$  (c) related signals are derived.

### 3.4.3. Magnetoresistance

In Figure 44 the per cent magnetoresistance effect for different samples is reported in the form of  $\Delta\rho/\rho = (\rho(4T) - \rho(0T))/\rho(0T)$ . No relevant effect is visible cooling the samples from room temperature down to about  $100K$ . At lower temperatures the magnetoresistance effect starts rising

and it reaches its maximum at 15K; then a little decrease is observable for lower temperatures. The behaviour's change around 100K could be thought as a signature of the STO substrate phase

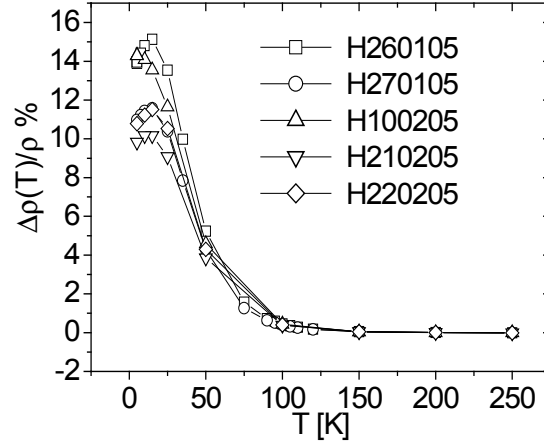


**Figure 44** Per cent magnetoresistance effect for samples reduced with different plasma conditions

transition from the cubic to the tetragonal phase: so the introduction of the oxygen vacancies in the reduced regions is not followed by a structural deformation of the original STO lattice.

It's worth observing the dependence of the resistance variation as a function of the field. In the weak magnetic field limit, the magnetoresistance can be expressed as:

$$\frac{\Delta\rho}{\rho} = \mu^2 H^2 f(\zeta) g(p) h(K) \quad (3.2)$$

where  $f(\zeta)$ ,  $g(p)$  and  $h(K)$  depend on the degree of degeneracy, the scattering mechanism and the shape of the energy surfaces, respectively [49]. The weak-field limit is set by  $\mu H \ll 10^8$ , where  $\mu$  is carrier mobility and  $H$  the magnetic field in gauss. So, because of the high values reached by the carrier mobility at low temperature, as will be discussed in next section, the limit is still valid only for field weaker than about 1T. Behind the weak-field limit a saturation effect is expected on the resistance variation versus the magnetic field, but no such a saturation has been evidenced in our field even at higher fields and at lower temperatures. Instead, it's interesting noticing that the observed resistance variations on the magnetic field follow a quadratic dependence at T=100K, while for lower temperatures the power dependence decreases, reaching a  $H^{1.8}$  and  $H^{1.6}$  dependence law at T=50K and T=5K, respectively, as shown in Figure 45.

In order to achieve more informations on the time dependence observed in the R(T) behaviour, the magnetoresistance effect measurements have been also repeated at different times: no relevant

variations have been detected except at low temperature, as shown in Figure 46 for sample H220205.

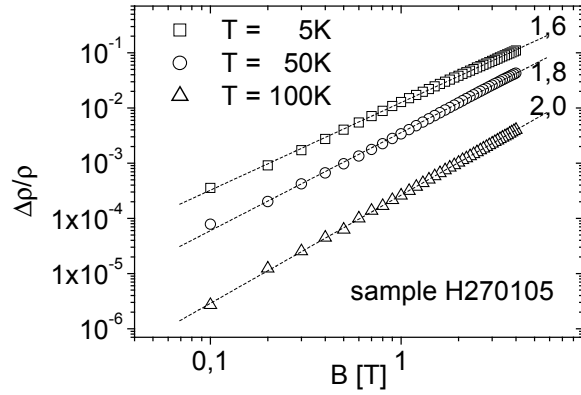


**Figure 45** Magnetic field dependence of the relative resistance variation in logarithmic scale for sample H270105. The slope values of linear fits are also shown

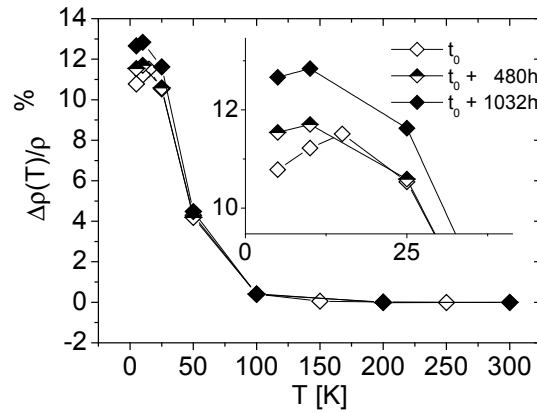


**Figure 46** Time variation of the magnetoresistance effect observed on sample H220205

### 3.4.4. Hall effect

The Hall effect measurements have been performed as described above at different temperatures and for different plasma conditions reduced samples. In our analysis a single band metal model is assumed for the evaluation of the Hall coefficient  $R_H$ , i.e.

$$R_H = \frac{1}{nq} \quad (3.3)$$

where  $n$  and  $q$  are the carrier concentration and the elementary charge, respectively. Moreover, since, as already stressed, the reduced region thickness is unknown, the Hall coefficient  $R_H$  is reported in a thickness normalized way first, i.e.  $R_H/d$  is shown. The Hall coefficient has been evaluated starting from the Hall voltages deduced in the way described in section 3.4.2: a linear fit led to the evaluation of the slope of the curves representing the Hall voltage dependence on the magnetic field. By dividing this slope by the current value,  $R_H/d$  has been obtained, i.e. starting from the Hall voltage expression:

$$V_H = \frac{1}{nq} \frac{IB}{d} = \frac{R_H}{d} \cdot IB \quad (3.4)$$

where  $I$  is the value of the current flowing in the sample,  $B$  the applied magnetic field and, as usual,  $n$ ,  $q$  and  $d$  are the carrier concentration, the elementary charge and the reduced region thickness, respectively.

In Figure 47, the temperature dependence of  $R_H/d$  for different samples is reported. The Hall coefficient it's almost always linear in temperature and only at low temperatures a slight increase is present. It's worth noticing that even if a quantitative comparison with analogue results obtained on other ways reduced  $\text{STO}_{3-\delta}$ , namely thermally reduced, is still not possible for the dependence on the reduced regions thickness, a good qualitative agreement is observable with the results reported in [47].

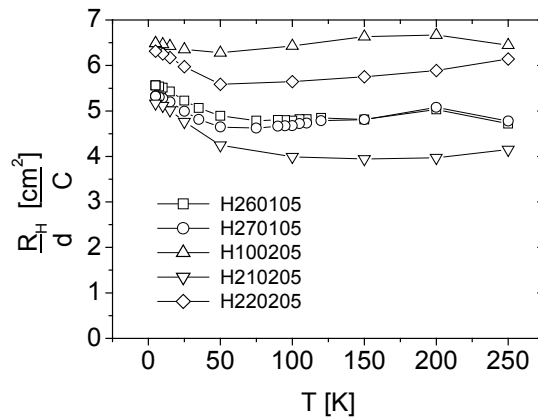


**Figure 47** Hall coefficient normalised to the thickness versus temperature for the samples of Table 2

The Hall measurements also have been repeated different times, as shown in Figure 48 for sample H220205. The  $R_H/d$  quantity increases in time, but at this stage it's not still possible to distinguish between a carrier concentration and a thickness variation.

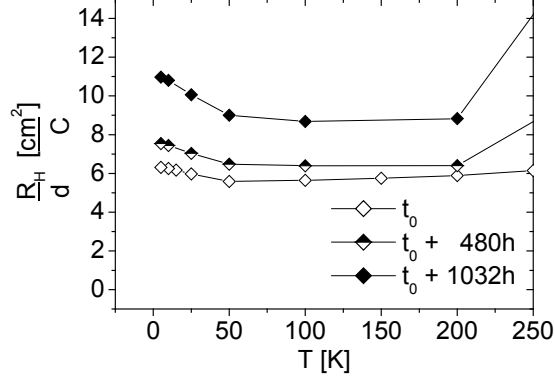


Figure 48 Time variation of the measured Hall coefficient on sample H220205

### 3.4.5. Mobility and thickness

The carrier mobility  $\mu$  is usually derived by combining the resistivity and Hall coefficient measurements results: in fact, starting from the definition of the conductivity for a single band metal:

$$\sigma = \mu nq \Rightarrow \mu = \frac{\sigma}{nq} = \frac{R_H}{\rho} \quad (3.5)$$

where  $\sigma$  represents the conductivity,  $\rho = 1/\sigma$  the resistivity and the Hall coefficient has the form reported in (3.3).

As often repeated, we don't know the actual resistivity and Hall coefficient values because of the unknown thickness values of the obtained  $\text{STO}_{3-\delta}$  regions in our samples, but the carrier mobility evaluation is still possible thanks the following observation:

$$\mu = \frac{\sigma}{nq} = \frac{R_H}{\rho} = \frac{R_H/d}{\rho/d} \quad (3.6)$$

In Figure 49 the mobility evaluated by utilising (3.6) is shown as a function of the temperature for different samples. The mobility follows with a very good agreement the data reported in [47].

From room temperature down to about  $T=80\text{K}$ , the law  $\mu \propto T^{-2.7}$  holds, while for lower temperatures different saturation values are reached by the mobility, as a signature of the different carrier concentration of our samples. In any case, the obtained hydrogen plasma reduced surfaces save the  $\text{STO}_{3-\delta}$  feature of a high mobility value at low temperature, on the order of  $10^3 \text{ cm}^2/\text{Vs}$ .

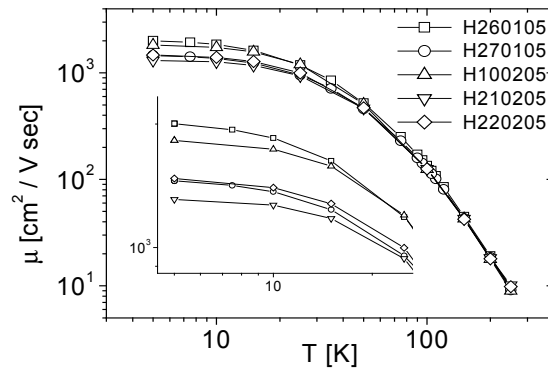


**Figure 49** Carrier mobility as a function of the temperature for the samples of Table 2

After the data obtained, an estimation of the carrier concentrations and of the reduced regions thickness is possible by utilising the data reported in [47, 50], shown in Figure 50. Because of the good agreement between the two data sets, the shown experimental relationship between the mobility and the carrier concentration can be thought as a typical feature of the  $\text{STO}_{3-\delta}$ , independent of the reducing method. So, assuming this relationship valid for our samples too, the carrier concentrations reported in Table 3 have been obtained. These values are still in good agreement with the data reported in literature.

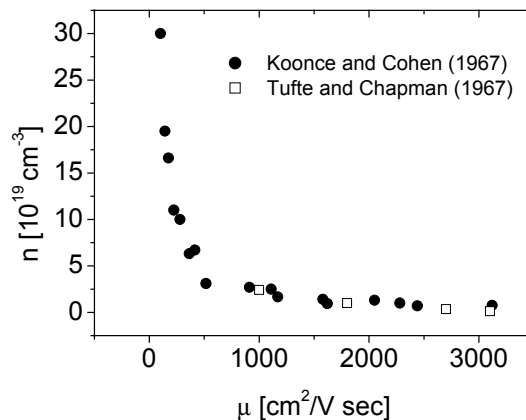


**Figure 50** Experimental relationship between the carrier mobility and concentration after [47] and [50]

In Table 3, an estimation of the thickness of the STO<sub>3-δ</sub> surfaces obtained is reported too. These values have been obtained by substituting the previous obtained  $n$  in the  $R_H/d$  data. Finally, after the obtained thickness' evaluation, the Hall coefficient  $R_H$  can be deduced.

sample	$\mu$ [cm <sup>2</sup> /Vsec]	$n$ [cm <sup>-3</sup> ]	$d$ [nm]	$R$ [ $\Omega$ ]	$R_H$ [cm <sup>3</sup> /C]
H260105	$2 \cdot 10^3$	1,3E19	98	33,3	$5,5 \times 10^{-5}$
H270105	$1,4 \cdot 10^3$	1,5E19	92	43,9	$4,9 \times 10^{-5}$
H100205	$1,8 \cdot 10^3$	1,3E19	70	42,6	$4,5 \times 10^{-5}$
H210205	$1,3 \cdot 10^3$	1,6E19	99	66,1	$5,1 \times 10^{-5}$
H220205	$1,5 \cdot 10^3$	1,5E19	69	51,4	$4,3 \times 10^{-5}$

**Table 3** Mobility, carrier concentration and thickness values

After the repeated Hall effect measurements reported in Figure 48, an evaluation of the time variation of carrier mobility and concentration as well as of the thickness of the reduced region have been carried out. In Figure 51 the different values of the mobility evaluated for the sample H220205 are shown. No great variations are observable, except a slight decrease at very low temperatures.

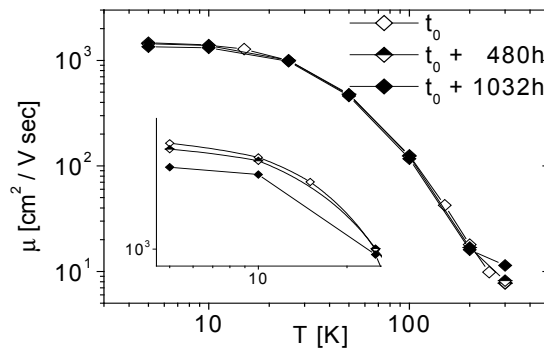


**Figure 51** Time variation of the carrier mobility evaluated on sample H220205

By applying the procedure described above, it's now possible verifying if the time variations observed until now can be thought as due to a variation of the intrinsic transport features of the plasma reduced STO or if the supposed hypothesis of the oxygen vacancies diffusion within the

substrate lattice mechanism is the responsible of such time variations. It's worth noticing that since the oxygen vacancies doping profile is unknown, the values of carrier concentration and reduced region thickness have to be thought as average values.

Starting from the carrier mobilities reported in Figure 51, the carrier concentrations and reduced region thicknesses shown in Figure 52 (a) and (b) were obtained. The deduced Hall coefficient is also shown in Figure 52(c).

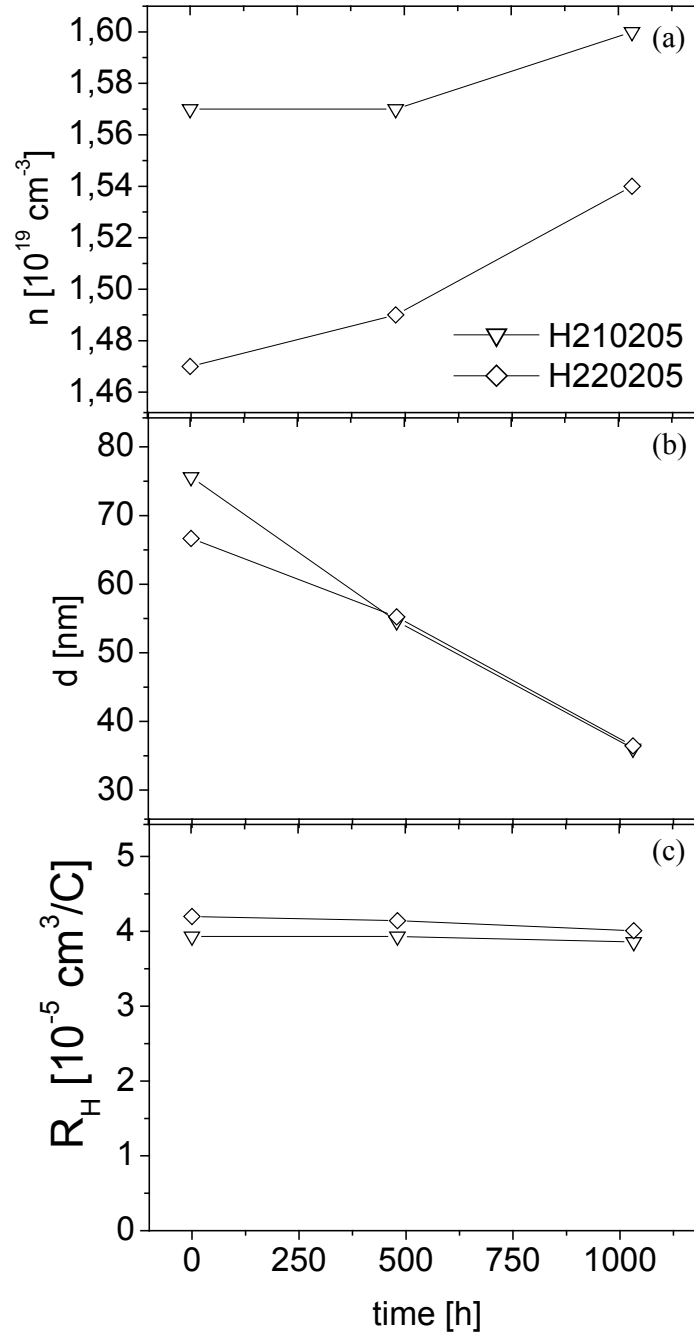


**Figure 52** Time evolutions of the carrier concentration (a), the thickness of the reduced region (b) and of the Hall coefficient obtained by repeated Hall measurements on samples H210205 and H220205.

To better comprehend the meaning of the time variation observed, we can start from the Hall coefficient  $R_H$  and the carrier concentration. Both the samples show a slight increase of  $n$ , whose amount doesn't affect too much  $R_H$ . So a constant carrier concentration can be assumed and the increase observed will be understood below.

The thickness variation seems to be more dramatic and in contrast with the oxygen vacancies diffusion mechanism already mentioned as a possible explanation of the room temperature resistance increase (see section 3.4.1). In fact, if such a process is assumed, the oxygen vacancies responsible of the metallic behaviour of the  $\text{STO}_{3-\delta}$  layers can be thought "expanding" within the STO substrate and, consequently, the doped layer thickness is expected to increase, even if an average value is considered.

But this line of reasoning implicitly assumes a linear relationship between the number of vacancies introduced and the number of charge carriers present in the sample: in a simple defect model each vacancy is assumed to induced two free electrons in the STO lattice because of the charge difference between an oxygen atom O present in the STO lattice itself and the oxygen ion  $\text{O}^{2-}$  removed by any method: so in  $\text{STO}_{3-\delta}$ ,  $2\delta$  electrons for every formula unit are expected. Moreover, when the vacancies migrate toward bottom layers, the number of carrier assumed fixed, an increase of the thickness is expected.

But that's not the case. Previous studies showed that in the  $\text{STO}_{3-\delta}$  system the number of free electrons per unit formula varies with  $\delta$ : the greater the number of vacancies induced, i.e. the greater  $\delta$ , the smaller the number of free electrons for unit formula responsible of the conduction [<sup>51</sup> and reference therein].

So, the oxygen vacancies diffusion leads to an increase of the charge carriers, i.e. electrons, as observed in our system. In addition, by this explanation the difference between the  $n$  increase observed in the two samples can be understood if the different plasma conditions employed for the two samples reduction are considered (Table 2): sample H220205 has been prepared with both greater  $\text{H}_2$  and Ar fluxes, over the double exposure time. In this way, more vacancies are expected to be induced in the lattice, so more vacancies are expected to migrate thanks to the diffusion process and, finally, a greater difference in the carrier concentration is expected to be observed due the greater difference between  $\delta$  and the actual free carriers per unit formula.

In this framework the meaning of the thickness reported in Figure 52(b) has to be reconsidered. Since the values found for it were derived by the Hall coefficient values,  $d$  is not the actual doped layer thickness anymore, even if with the average meaning introduced above. It can be rather thought as a measure of an "equivalent layer" thickness obtained assuming a false linearity between the oxygen vacancies present and the electrons responsible of the conduction.

### 3.5. Field effect measurements

After the characterization reported in previous sections, obtained on 500 $\mu\text{m}$  thick STO samples, field effect measurements have been performed on 100 $\mu\text{m}$  thick STO crystals by employing the experimental equipment described in section 3.1.2. The  $\text{STO}_{3-\delta}$  surface layers were reduced by the same plasma conditions of sample H081104, i.e.  $\text{H}_2$  flux = 26,2sccm, Ar flux = 25sccm, exposure time=5min (see Table 2). Before the reduction, a gold pad approximately 100nm thick and with the same channel width and length, i.e.  $w=600\mu\text{m}$  and  $l=500\mu\text{m}$ , has been deposited on the back of STO substrate by sputtering, as shown in Figure 40(5), as gate electrode.

#### 3.5.1. Capacitance vs. Applied field

The realised devices have been characterized in term of capacitance versus temperature for different applied gate voltages, by employing the LCR meter introduced in sec. 3.1.2. The measurements have been performed by applying a 1V and 1kHz oscillating signal between the current contantc on the sample and the gate electrode. After these measurements an extimation of the dielectric constant  $\epsilon_r$  of the STO substrate was possible, assuming a flat and parallel capacitor model:

$$C = \epsilon_0 \epsilon_r \frac{S}{d} \quad (3.7)$$

where  $S$  and  $d$  represent the capacitor area and thickness, respectively, and  $\epsilon_0$  the vacuum dielectric constant. In our case the area is determined by the channel length and width, while for the thickness the entire STO crystal thickness has been considered: in fact, after the results reported in Table 3, the  $\text{STO}_{3-\delta}$  layer can reach the maximum thickness of 100nm, which represent the 0,1% of the entire crystal. So negleting it, a negligible error is introduced.

In Figure 53 the measurements results and the following  $\epsilon_r$  evaluation are shown for applied gate voltages of 0V and 100V. The results are in good agreement with literature data [see for example <sup>52</sup>]. Slight difference in the low temperature dielectric constant values, on the order of a factor lesser than 2, can be thought as results of the errors introduced by neglecting the  $\text{STO}_{3-\delta}$  layer thickness and by assuming the capacitor area as the channel area, since fringing field are of corse present.

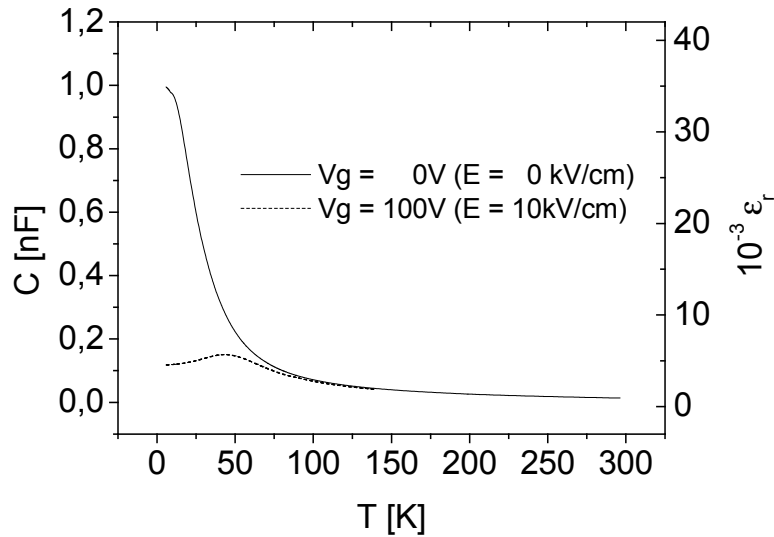


**Figure 53** Capacitance measurements and dielectric constant evaluation on 100µm thick STO crystals

In any case the reported results confirm that no relevant structural changes are introduced in the STO substrate lattice by the plasma cleaning procedure. Moreover, the assumption that no hydrogen was incorporated in the lattice during the plasma procedure keeps hold and, if any, no relevant effect has been observed.

### 3.5.2. R (T) vs. Vg

Field effect has been proved on R(T) curves first. In Figure 54 the effect of the field is shown: curves obtained for an applied gate voltage of  $-100\text{V}$ ,  $-50\text{V}$ ,  $0\text{V}$ ,  $50\text{V}$  and  $100\text{V}$  are reported. As expected the resistance increases for negative applied voltages and decreases for positive ones, thanks to the repulsion or attraction experienced by the electrons responsible of the conduction by the applied field. Moreover, curves obtained for  $V_g = 50\text{V}$  and  $V_g = -50\text{V}$  don't show relevant difference with the one for  $V_g = 0\text{V}$ , except at very low temperatures. This is expected to the screening effect of the charge carriers, overcome by the great polarization induced at low temperatures due to the increased dielectric constant of the STO substrate (see Figure 53).

It's worth noticing the little flattening shown by the curve at  $V_g = -100\text{V}$  around  $T=80\text{K}$ . The difference between the latter and the others is that the curve at  $V_g = -100\text{V}$  has been obtained by

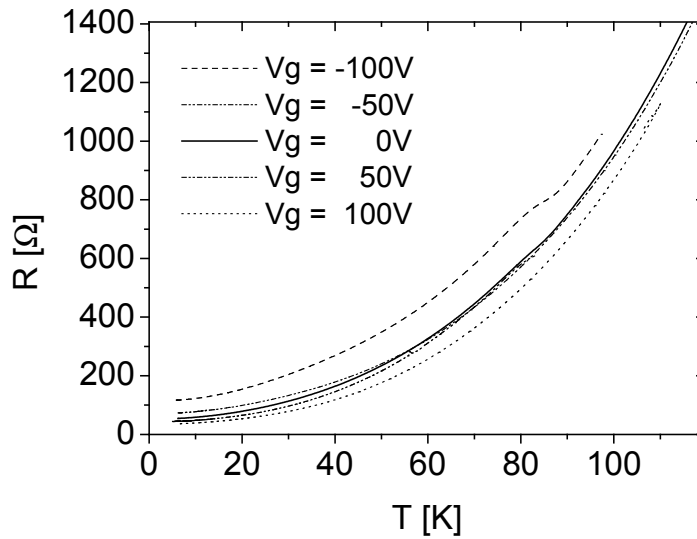


**Figure 54** R(T) curves for different applied gate voltages

warming up the sample after the application of the transversal field, rather than cold down it. This feature has been verified for other R(T) curves, as shown in Figure 55. If any field is not applied to the sample, the R(T) curves obtained by cooling down or warming up the samples are the same. But if any field is applied to the gate electrode, the samples shows a sort of memory effect until a fixed temperature, as shown in Figure 55(a). Even if a different field is applied to force the sample response, no effect is obtained, as shown in Figure 55(b), where the applied gate voltage has been switched between 0V and 100V during the measurement. In addition, the effect disappears at fixed temperatures, i.e. at  $T \approx 83\text{K}$  and  $T \approx 177\text{K}$  (the latter observed only for  $V_g = 0\text{V}$  curves).

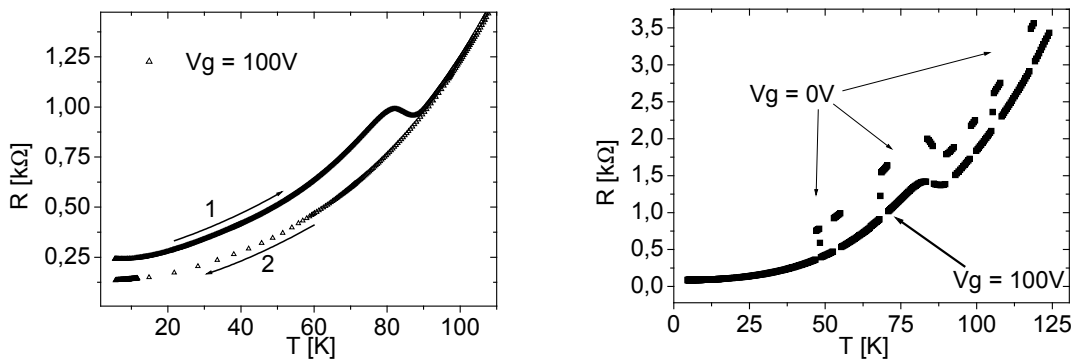


**Figure 55** The memory effect in the R(T) curves

### 3.5.3. R vs. Vg at low temperatures

The effect of the field on the transport features of our samples has been studied at the minimum temperature achievable with the system, i.e. at  $T=5\text{K}$ . In this way, the STO substrate great dielectric constant is exploited in order to induce a bigger carrier modulation at a fixed applied gate voltage.

In Figure 56 a typical resistance modulation obtained is shown. The measurement has been performed starting with  $V_g=0\text{V}$  and increasing the gate voltage until  $100\text{V}$ , then decreasing it from  $100\text{V}$  until  $-100\text{V}$  and finally reincreasing it from  $-100\text{V}$  until  $0\text{V}$ . The reported data show some common feature of the plasma reduced system response to the transverse field that are discussed in the following.

For positive gate voltages, after a first little decrease, the resistance seems not to experience any applied field and it saves the same value until the maximum applied field is reached (1); but when the gate voltage is decreased down to  $-100\text{V}$ , the effect of the transverse field is visible and the resistance increases as expected (2); finally the same behaviour is followed when the gate voltage comes back to  $0\text{V}$ , even if a memory effect is present and the measured resistance values are a little bigger, as more evident at  $V_g=0\text{V}$ . This memory effect is related to the one observed on  $R(T)$  curves measured for different applied transverse field discussed in the previous section (see Figure 55).

Now, if the same kind of measurement is repeated, with the same maximum  $V_g$ , the saturation effect for positive gate voltages is not present anymore, as shown in

Figure 57(a), and, except for the memory effect already mentioned, the resistance follows the same curve as a function of the applied gate voltage.

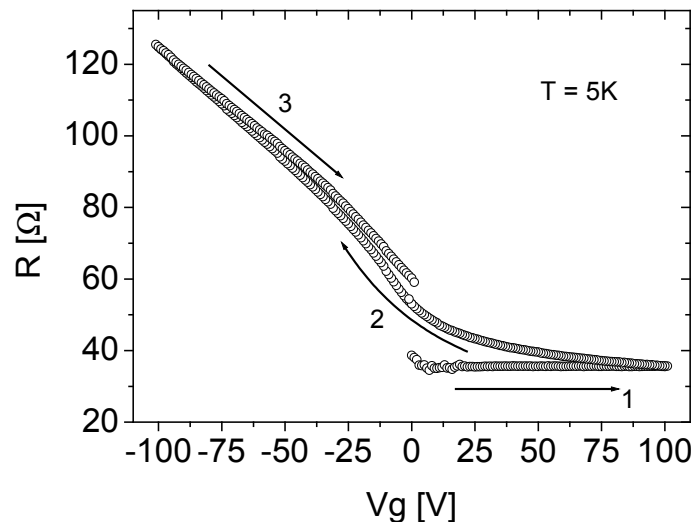


**Figure 56** The field effect on the resistance at  $T=5\text{K}$

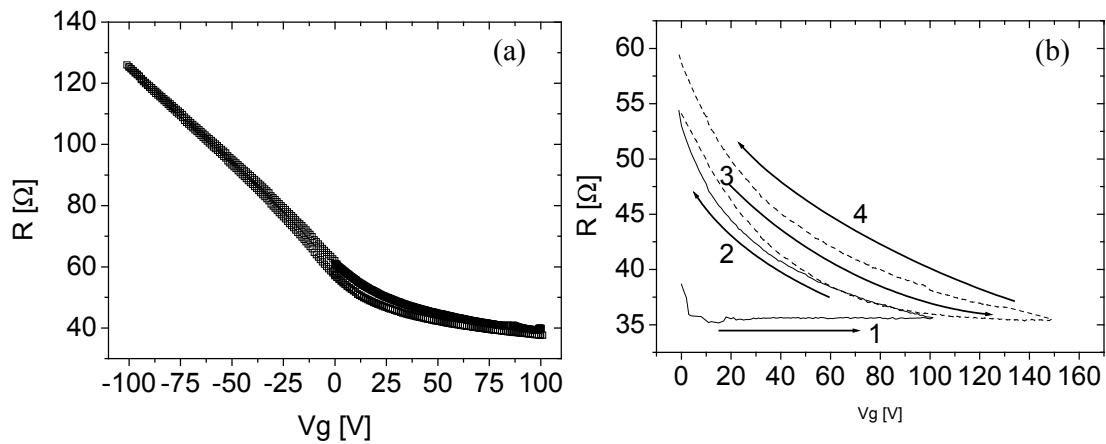


**Figure 57** The saturation effect observed for positive  $V_g$  disappears if the measurement is repeated between the same gate voltages (a), while if a bigger positive gate voltage is applied, it is present again.

Moreover, if now the  $R(V_g)$  measurement is repeated reaching an applied gate voltage greater than the maximum  $V_g$  already applied to the sample, let's call it  $V_g'$ , the saturation effect is visible again for  $V_g > V_g'$ , i.e. the resistance doesn't reach values smaller than the one reached while the gate voltage was applied for the first time, as shown in Figure 57(b). In addition, if the sample is warmed up to one of the "special temperatures" mentioned in previous section about the disappearance of the  $R(T)$  memory effect, when it is cooled down it presents again the first saturation discussed in Figure 56.

The field effect was also verified on the IV curves. The results are reported in Figure 58.

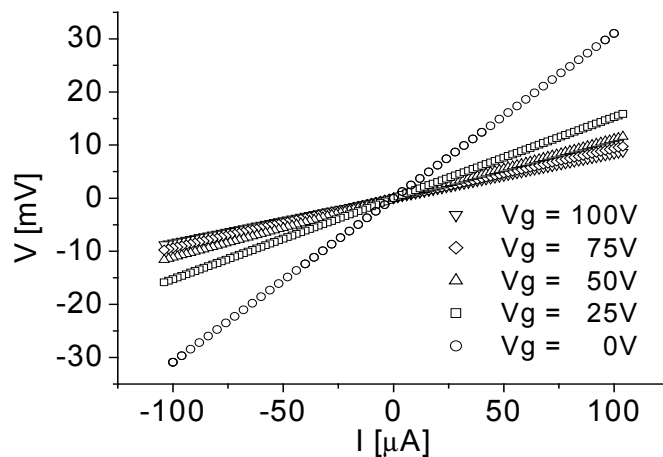


**Figure 58** Field effect on IV curves at  $T=5K$

### 3.6. Hall effect and field effect

In order to better understand the actual effect of the applied transverse field on the  $\text{STO}_{3-\delta}$  surface layers transport features, Hall effect measurements were executed during the appliance of gate voltages. This measurements were performed in the Hall system described in 3.1.1 with the addition of the Keithley source meter: in this way the appliance of the gate voltages and the monitoring of the eventual leakage currents were possible. The results were carried out by combining the procedures already described in previous sections, i.e. by scanning the transverse field and, for every single gate voltage, Hall effect measurement was performed by scanning the magnetic field reaching a maximum of 1T.

In Figure 59(a) the obtained resistance modulation versus the applied gate voltage is reported. Here again,  $V_g$  was scanned in three steps: (1) starting from 0V, reaching a first maximum value  $V_{g'}$ , then decreasing  $V_g$  until  $-V_{g'}$  and finally coming back to  $V_g=0V$ ; (2) the same scanning procedure was repeated; (3) the procedure is repeted again, but reaching a new maximum gate voltage  $V_{g''} > V_{g'}$ . So the saturation effect for the first gate voltage appliance and the memory effect, both discussed in the previous section, can be studied.

The related Hall effect results are reported in Figure 59(b) as a function of  $V_g$ , in the same thickness normalised form used in section 3.4.4. The modulation of the Hall coefficient is evident, as expected. It's interesting noticing the increasing values carried out for the three curves, probably due to the variation of the “equivalent thickness” time variation highlighted in section 3.4.5.

Starting from these data, the same analysis described in section 3.4.5 about the carrier mobility  $\mu$ , the carrier concentration  $n$  and the equivalent thickness  $d$  was performed to obtain information about the variation of these quantity as a function of the applied transverse field.

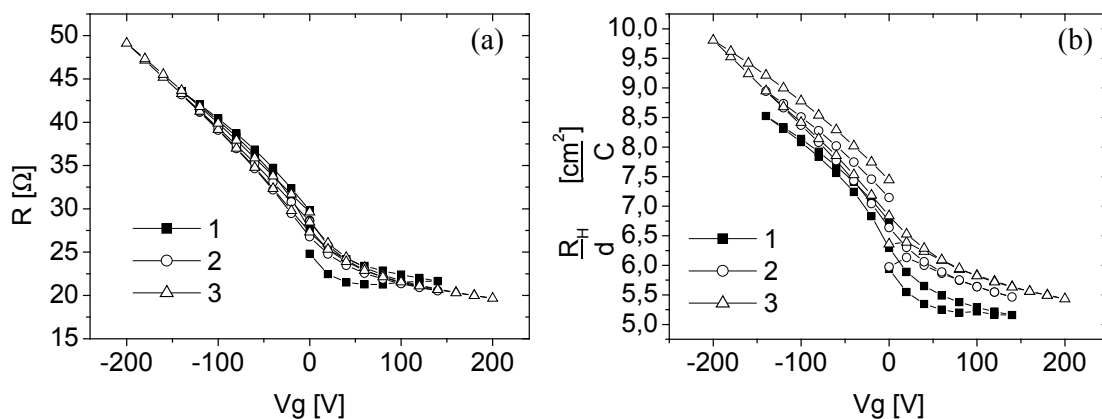
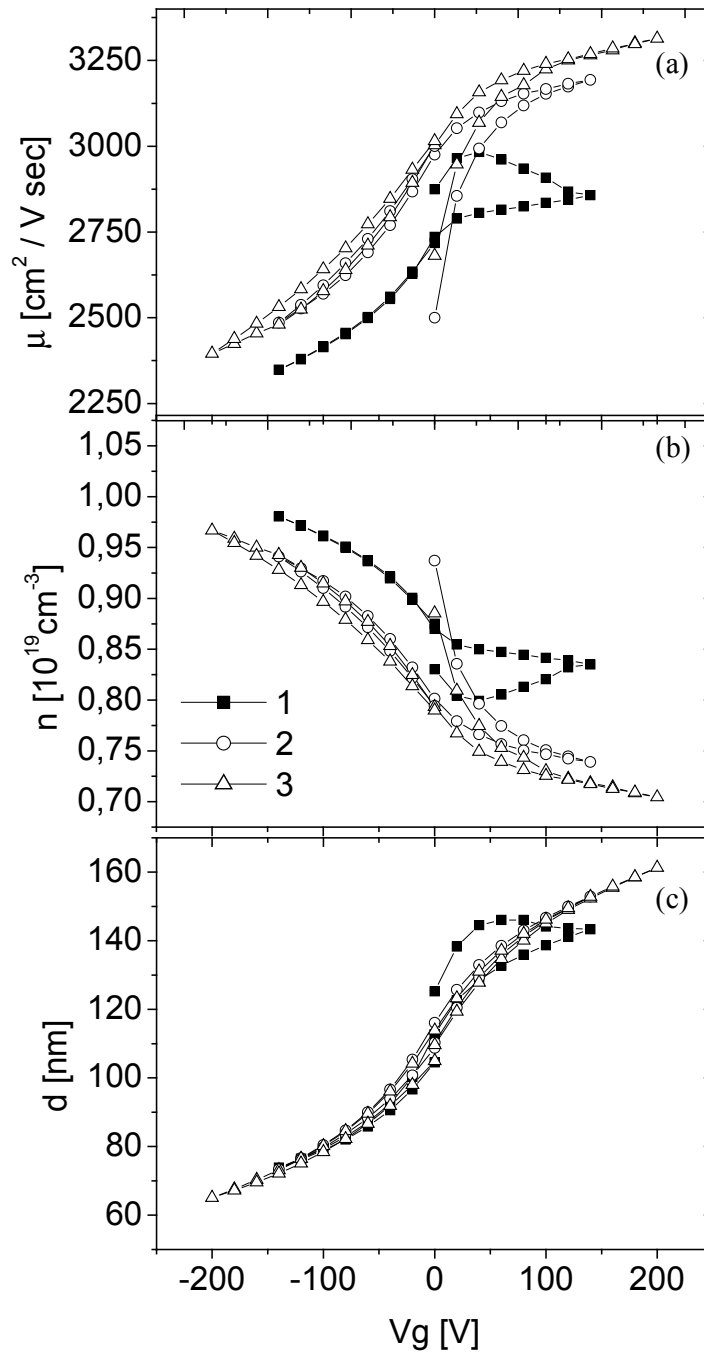


Figure 59 (a) Field effect measurements at  $T=5K$  and (b) related Hal effect results reported

In Figure 60 the results carried out by such an analysis are reported. The mobility variation as a function of the applied gate follows more or less the resistance behaviour, but shows two interesting features (Figure 60(a)). First, as long as the resistance stands fixed at the saturation value during the first  $V_g$  scan, the mobility shows a variation, but in the opposite way of the one expected. As a matter of fact, the appliance of a positive gate voltage should enhance the transport feature in an electron based system; at least in our case, since the resistance doesn't vary on this branch of the curve, the same constant behaviour is expected for the mobility, whereas it decreases. This could be explained by considering an oxygen vacancies response to the electric field, but the opposite response should be present for opposite fields, and that's not. In second place it's worth noticing the "transient-like behaviour of the mobility at the start of the two subsequent scannings. This could be thought due to a very big time constant of the system, but the switching measurement reported in Figure 55(b) doesn't agree with this explanation.

Figure 60(b) the carrier concentration  $n$  derived as described in section 3.4.5 is reported as a function of  $V_g$  too. From these data the system seems to act in the opposite way than expected, with a decrease of the carrier concentration for positive voltages and vice versa. In our opinion these data don't describe the real phenomenon and can be thought as an artefact due to the way they were deduced. In fact, the carrier concentrations were evaluated starting from the mobility values thanks to the relationship reported in literature. Evidently the applied method doesn't stand any more when a transverse field is applied to the system.

Finally, the evaluated "equivalent thickness"  $d$  is also reported in Figure 60(c). As stressed in section xxx, the obtained value is an estimate of the order of the extent of the doping inside the STO substrate, but its variations are necessarily related to the ones observed for the Hall coefficient.



**Figure 60** Transport features modulation as a function of the applied gate voltage  $g$ : (a) the carrier mobility; (b) the carrier concentration; (c) the equivalent reduced layer thickness



# Chapter 4

## Field-effect experiments on NdBCO thin films

In this chapter the field-effect experiments results on NdBCO thin films are reported. After the description of the device realization technique (sect. 4.1), the experimental apparatus used in these experiments is described (sect. 4.2). The obtained results are reported in the rest of the chapter, where electrostatic modulation of the  $R(T)$  behaviour on both insulating and superconducting thin films are reported. In the latter case, the field-effect on the IV curves and the role of the current flowing in the channel are also investigated.

### 4.1. Device realization

A completely in situ technique has been employed to realize the NBCO field effect devices. In this way the atmosphere exposure of the thin film surface is avoided and so no surface degradation is expected.

As already mentioned in chapter 2, the thin films under test were deposited on STO substrates, with which they present a good lattice matching.

The deposition equipment allows both the possible solutions illustrated in sect. 1.x are present in the same device, i.e. both the STO substrate and an  $Al_2O_3$  thin layer can be used as gate insulator. Hence, the device realization procedure consisted in the following steps, sketched in :

1. NBCO thin film deposition on the STO substrate
2. gold contacts for measurements deposition on the NBCO channel
3.  $Al_2O_3$  thin layer deposition in the center region of the sample, overlapping the four contacts internal edges
4. two gold contacts as gateelectrod on the  $Al_2O_3$  layer and on the back of the STO substrate

The details of the NBCO thin films deposition, their structural properties and transport features have already been reported in sect. 2.x. The NBCO were deposited in the main chamber of the deposition system. This chamber is connected to two secondary chambers. In this way all the mentioned steps required for the device realization are allowed to be performed with no vacuum breaking and consequently with no channel surface degradation.

In a secondary chamber a Joule effect evaporator allows the deposition of thin gold layers. A little tungsten bar containing gold pellets is warmed by Joule effect, i.e. by a high current

flowing in it (about 250A). By this means the four gold contacts needed for the four probes measurement technique were deposited on the NBCO surface (Figure 61(b)). Stencil masks

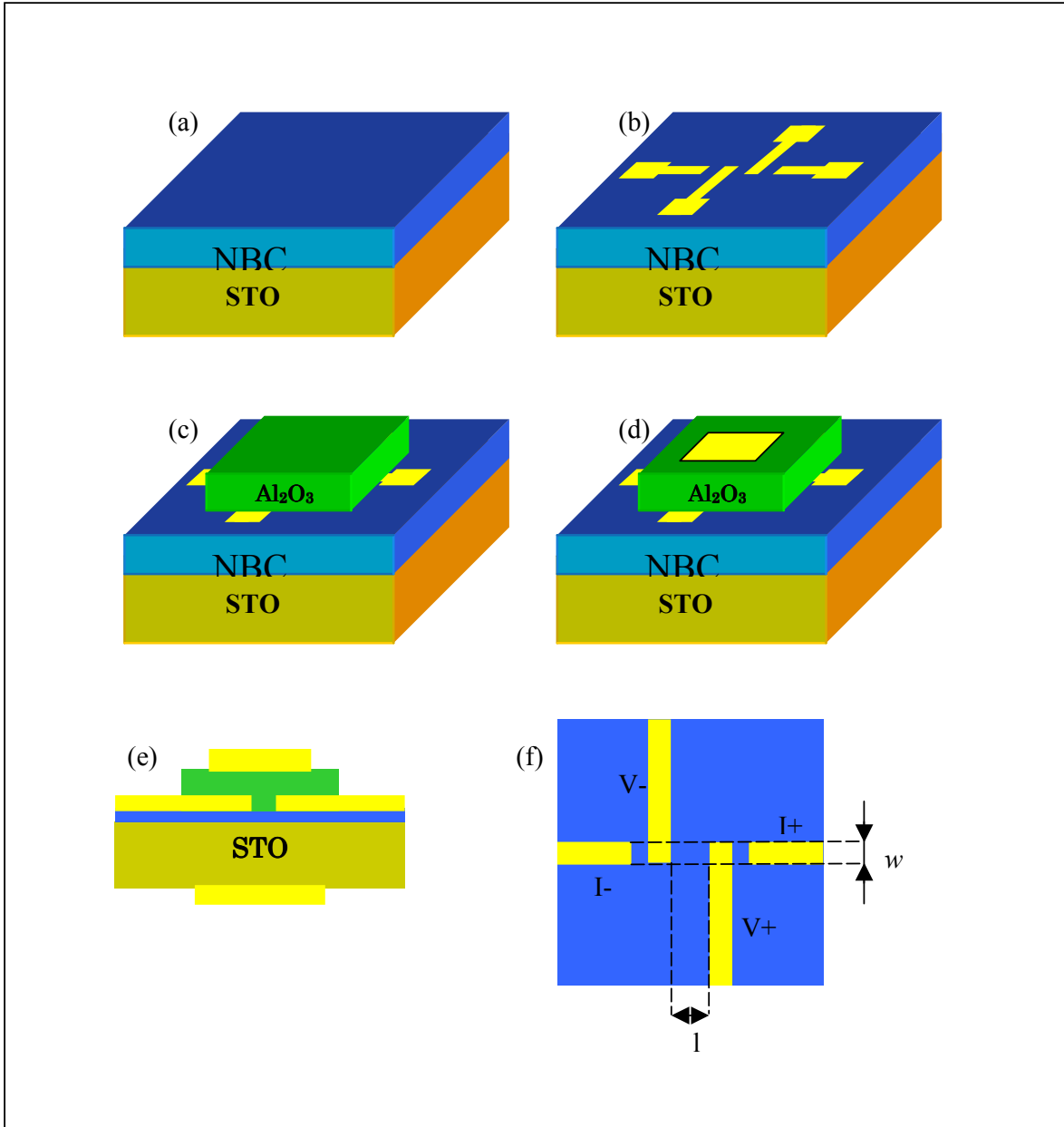


**Figure 61** Schematic representation of the device realization procedure: (a) NBCO thin film deposition on the STO substrate; (b) gold contacts deposition; (c) Al<sub>2</sub>O<sub>3</sub> insulating layer deposition; (d) gate electrodes deposition; (e) cross sectional view of the final device; (f) gold contacts layout on the NBCO thin film

allowed to obtain the desired shape for the contacts, sketched in Figure 61(f). The distances between the gold contacts are  $l=25\mu\text{m}$ , i.e. the channel length, and the pads width, i.e. the channel width, is  $w=50\mu\text{m}$ . The contacts are 15 nm thick.

$\text{Al}_2\text{O}_3$  was deposited by d.c. magnetron sputtering technique. A magnetic field acting on the gas mix (Ar- $\text{O}_2$ ) ensures a greater efficiency in the sputtering rate and so lower pressures could be used during the process. A high purity Al target was used and the presence of an Ar- $\text{O}_2$  atmosphere ensures the  $\text{Al}_2\text{O}_3$  deposition. It's worth mentioning the influence of the  $\text{O}_2$  pressure in the chamber on the deposition process: if a too high oxygen flux is setted in the chamber, the Al target results completely oxidized. This could be avoided by knowing the so-called calibration curve, i.e. an hysteresis curve representing the voltage on the target as a function of the oxygen flux. As reported in Figure 62, in our case a maximum oxygen flux of about 3,9 sccm has been found before the Al target results oxidised, i.e. the voltage on the target decreases abruptly in the calibration curve. Hence Ar and  $\text{O}_2$  fluxes of 50sccm and 4sccm, respectively, were used to create the gas mix in the chamber. The other parameters values employed during the deposition are reported in literature (see for example [53]). The layer was deposited in the central region of the device and covered the four gold contacts edges as depicted in Figure 61(c). The  $\text{Al}_2\text{O}_3$  dielectric constant is about 10, so thin layers and greater applied gate voltages are needed in order to obtain substantial carrier modulations, as already stressed in the first chapter. 150 nm thick  $\text{Al}_2\text{O}_3$  layers have been used in present work.

Finally, by the Joule effect evaporator already described, two gold gate electrodes were deposited both on the back of the STO substrate and on the  $\text{Al}_2\text{O}_3$  layer (Figure 61(d)).

Following the described procedure, devices with 4-10 $\mu\text{m}$  thick NBCO channels were realised.

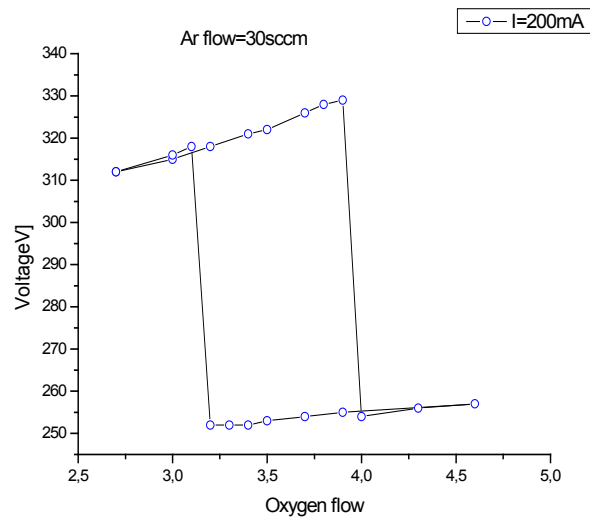


**Figure 62** Calibration curve for the  $\text{Al}_2\text{O}_3$  layer: voltage represents the target voltage.

The obtained devices were placed on a plastic chip on which gold contacts are available for the electrical connections. In case of I and V contacts, the connections were realised by wire-bonding Au wires between the gold pads on the chip and the gold contacts deposited on the device, whereas the gate electrodes were connected by thicker Cu wires glued on the gate electrodes by silver paint.

## **4.2. Experimental apparatus in Naples**

The instrumental apparatus in Naples consists of a voltmeter (Keithley 2001), a Keithley 2400 source-meter and a picoammeter (Keithley 487). The source-meter can act as both voltage and current source and it can simultaneously perform measurements as ammeter or voltmeter. The picoammeter allowed measuring currents with high precision down to about tens of picoampere. Moreover it contains a voltage source too, capable of providing voltages up to 500V in both the polarities.

By employing the available instrumentation, both traditional four probes and even two probes resistance measurements are allowed. As well known, the four probes technique allows eliminating measurements errors due to leads and even contacts resistances; moreover the current inversion has been used in order to eliminate spurious thermoelectric effects on the voltage signals. In this kind of measurements the source-meter was used as current source and the voltage was measured by the 6871-voltmeter. Usually currents of  $10\mu\text{A}$  or  $1\mu\text{A}$  were setted flowing in the channel between I+ and I- contacts. The possibility of measuring the actual current flowing in the sample offered by the source-meter combined to the overflow signal displayed on the voltmeter allowed to monitor if a too high resistance was present at the instrument interface, i.e. if the measured resistance was higher than the internal resistance of the voltmeter. In this case the two probe arrangement was needed. The latter was performed by applying a fixed voltage, usually 1V or 10V, between two among the available contacts on the sample (preferably the closest ones) and measuring the resulting flowing current. Both the functions were performed by the picoammeter, whose mentioned characteristics allowed resistance values up to the order of  $\text{G}\Omega$  were measured. In particular, the two probe technique was employed to measure the resistance in thinner insulating channels, i.e. on 4u.c. thick NBCO films: in this case the introduced error due to the contacts or leads resistances is negligible in respect of the measured resistance value.

Field effect experiments were performed by applying a voltage on one of the two available gate electrodes, i.e. exploiting the STO substrate or the Al<sub>2</sub>O<sub>3</sub> thin layer as gate insulator. In samples in which four probe measurements were possible, the gate voltage was applied by the voltage source provided in the picoammeter, while in two probes measurements the voltage source of the source-meter was exploited. In the first case, the picoammeter was also employed in order to monitor the current flowing through the insulator, ensuring no artefact effects on the measured channel resistance due to eventual leakage across the dielectric. Maximum leakage currents on the order of 10nA (two order of magnitude lower than the measurement current) were thought don't affect the field effect results. Yet, when the source-meter was employed to apply the gate voltages, even if the applicable voltage is limited to "only" 200V, substantial effects are yet expected thanks to the thinnest films lower carrier concentration (see sect. 1.x and 2.y).

In order to perform low temperatures measurements, the chips with the realised device were placed on a sample holder at the end of a bar which can be dipped in a dewar containing liquid helium. It's worth highlighting that since, as mentioned above, very high voltages were applied, very low currents needed to be monitored and high resistance had to be measured, a great attention was paid in verifying the insulation between the contacts on the sample holder, within the bar itself and at the interface between the bar and the instrumentation. The non-trivial requirement of an insulation of the order of about 100GΩ was respected.

The sample temperature was monitored by a Cernox sensor, i.e. a semiconductor whose resistance increases as long as the temperature decreases. Good thermal contact between temperature sensor and sample holder as well as between the holder and the sample itself was ensured by a subtle resin layer, characterised by both very good thermal conduction and electrical insulation.

Although all the measurements were performed in 'remote' control employing LabView procedures, these were designed with a great flexibility and with the possibility the operator can intervent during the measurements.

Employing the described instrumentation, resistivity versus temperature measurements as a function of different applied gate voltages were performed. Also the effect of the transverse field on the IV curves was investigated. The resistivity data were obtained starting from the resistance versus temperature measurements by employing the well known formula:

$$\rho = R \frac{wd}{l}$$

where  $R$  is the measured resistance and  $w$ ,  $l$  and  $d$  are the width, the length and the thickness of the sample under test, i.e.  $w$  and  $l$  are the width and the distance between the internal gold contacts

deposited on the sample.

The sheet resistance, defined as the surface resistance of material, can be evaluated as:

$$R_{\square} = R \frac{W}{l}$$

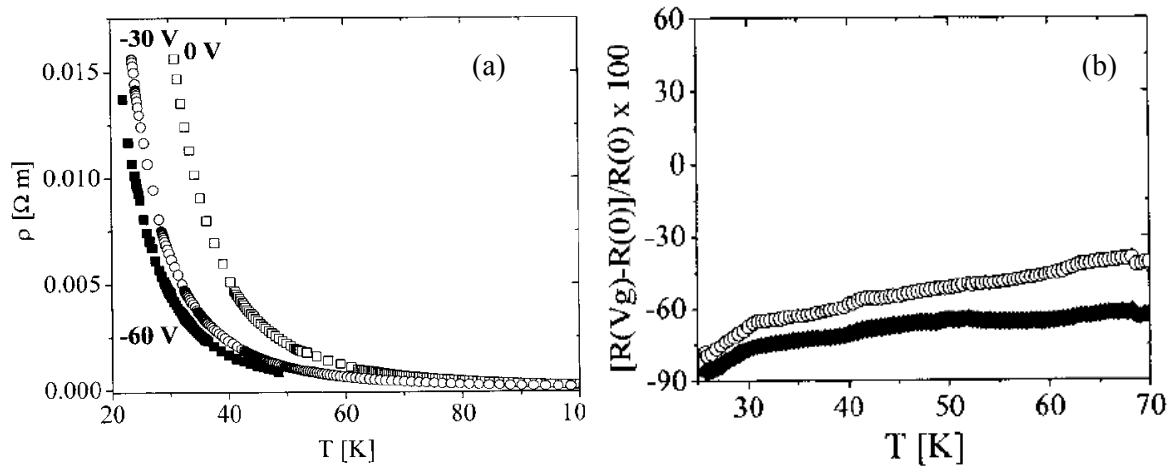
### 4.3. Field effect on resistivity vs. temperature behaviour

Field effect measurements on very thin  $\text{NdBa}_2\text{C}_3\text{O}_{7-\delta}$  films were performed by Matthey and co-workers [54]. In this case superconducting 2u.c. thick NBCO films transport properties were modulated by applying the transverse field across a thinned STO substrate (about  $110\mu\text{m}$ ).

As already stressed in chapter two, the NBCO films used as channels in this work are clearly underdoped, i.e. their carrier concentration lays on the left side on the phase diagram. Moreover their carrier concentration diminishes as long as the film thickness is reduced. This latter feature was exploited performing field effect experiments on both insulating (4u.c. and 8u.c. thick films) and superconducting (10u.c. thick) samples. In this section the effect of the transverse field on the resistivity vs. temperature were reported, while in the next section its effect on the IV curves is discussed. It's worth remembering that during each measurement the leakage current through the  $\text{Al}_2\text{O}_3$  layer was always at least two orders of magnitude lower than the current between source and drain (typically  $1\mu\text{A}$ ), and in any case at low temperature it was never found to be higher than 10 nA.

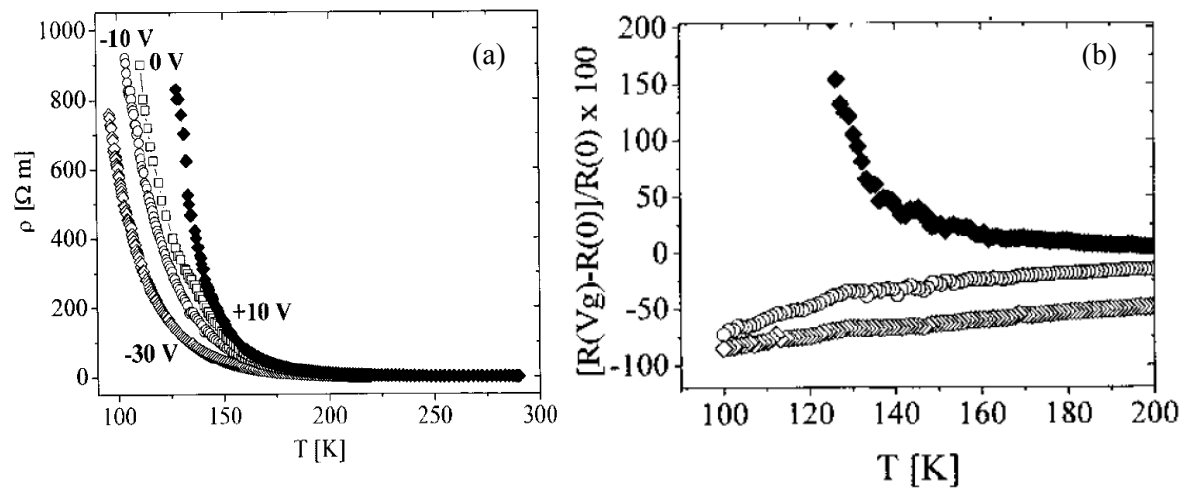
The insulating channel devices have been characterized first, employing both the STO substrate and the  $\text{Al}_2\text{O}_3$  layer as gate insulators. The results obtained in the up-gated configuration are discussed first. In this case, a 10V applied gate voltage corresponds to an applied field of about  $0,7\text{MV}/\text{cm}$ . The corresponding injected surface carrier density is expected to be in the range of  $4 \times 10^{12} \text{ cm}^{-2}$ .

Figure 63(a) the modulation of the resistivity versus temperature curves for a 8u.c. thick channel exploiting the up-gated configuration are reported. In Figure 63(b) the relative per cent variation of the resistance is reported as a function of the temperature for both the applied fields: a maximum variation of about the 90% was evaluated in case of an applied gate voltage of  $-60\text{V}$ . In this case, even if the sample showed a clear insulating behaviour, the low temperature resistance values still allowed the use of the four probe measurements technique. Applying negative gate voltages results in a decrease of the resistivity confirming that the charge carriers of these films are holes, as expected. The modulation of the carrier density can be evaluated and a variation  $\Delta n \approx 1,7 \times 10^{20} \text{ cm}^{-3}$  was found for an applied gate voltage of  $-30\text{V}$ .



**Figure 63** (a) Resistivity vs temperature curves at different gate voltages for 8u.c. thick NBCO channel in the up-gated configuration; (b) per cent variation of the resistance for the same sample.

In Figure 64, the results obtained on a 4u.c. thick NBCO channel in the same up gated configuration are reported. The two probe arrangement was needed to measure the channel resistance in these devices, due to the high resistance values measured, mainly at low temperature. In this case a maximum variation of about the 150% was observed for a gate voltage of 10V (Figure 64(b)). It's worth highlighting that an asymmetry was observed in the modulation of  $R(T)$  curves if gate voltages of +10V and -10V are applied to the same sample, which suggest different material responses in case of holes are added or removed at the interface by field effect doping.



**Figure 64** (a) Resistivity vs temperature curves at different gate voltages for 4u.c. thick NBCO channel in the up-gated configuration; (b) per cent variation of the resistance for the same sample.

In both the sets of results presented, there is a clear evidence that the change of resistivity by field effect in these samples is temperature dependent. As shown in Figure 63(b) and in Figure 64(b), the relative variation of the channel resistance, measured at different gate voltages, increases significantly at low temperature. In the framework of a VRH transport mechanism, this effect can be explained with a change of the characteristic temperature  $T_0$  (see sect. 2.2.1), that is found to decrease by increasing the density of holes injected [55].

The field modulation is more effective when the film thickness is decreased from 8 to 4 u.c. Indeed in the case of 8u.c. FET a higher gate voltage and/or a lower temperature is needed to see a substantial change in the resistivity, accordingly with the reduced charge carrier concentration in thinner films and with the role of the intrinsic carrier density discussed in chapter 1.

It's worth mentioning that all the measurements are reversible upon changes of the value and sign of the applied gate voltage, as will be shown in the following.

Field effect on superconducting samples was also tested, in both up-gate and back-gate configuration, as reported in Figure 65(a) and Figure 65(b), respectively. Even if in optimally doped NBCO thin films the field effect modulation of the normal transport features and even the shift of the transition temperature was clearly observed by Matthey and coworkers [54], in our devices no substantial effect but a maximum 3% of variation in the resistance value and no  $T_c$  shift was observed.

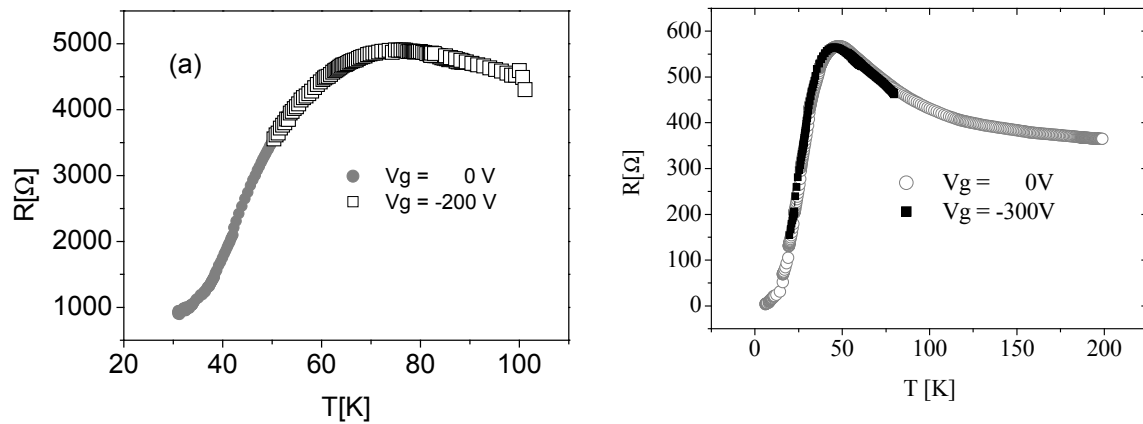


**Figure 65** Field effect on 10u.c. thick superconducting NBCO film in (a) up-gate and (b) back-gate configuration

Also in 8u.c. channel devices, the resistivity versus temperature curves were modulated by exploiting the STO substrate as gate insulator, i.e. in the back gate configuration. Employing a 500 $\mu$ m thick STO single crystal, The results obtained with a 500 $\mu$ m thick STO substrate are reported in Figure 66, where the curves obtained with applied gate voltages of 500V and -500V are

reported and compared with the one at  $V_g=0V$ . In this experiments, performed again employing the four probe technique, the gate voltage was switched between the two values in order to verify the reversibility of the effect observed. The switch is visible at  $T\approx 30K$ .

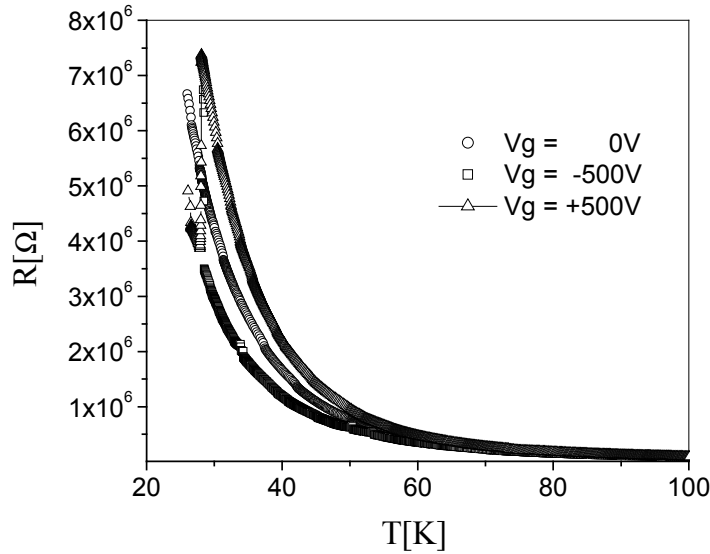


**Figure 66** Field effect on  $R(T)$  curve on a 8u.c. thick NBCO film in the back gate configuration; the reversibility of the experiments is shown too.

It's interesting to compare the resistance variations observed in the back gate lay out with the ones observed in the up gate lay out, as reported in Figure 67, where the results reported in Figure 63(b) are compared with the ones obtained starting from data reported in Figure 66. Even if the STO substrate in principle ensures a greater carrier modulation in respect of the  $Al_2O_3$  thanks to its huge dielectric constant, in this case the gate insulator layer thickness plays a major role in determining the surface polarization. Moreover, the variation of the STO dielectric constant as a function of the applied field and of the temperature has to be considered too.

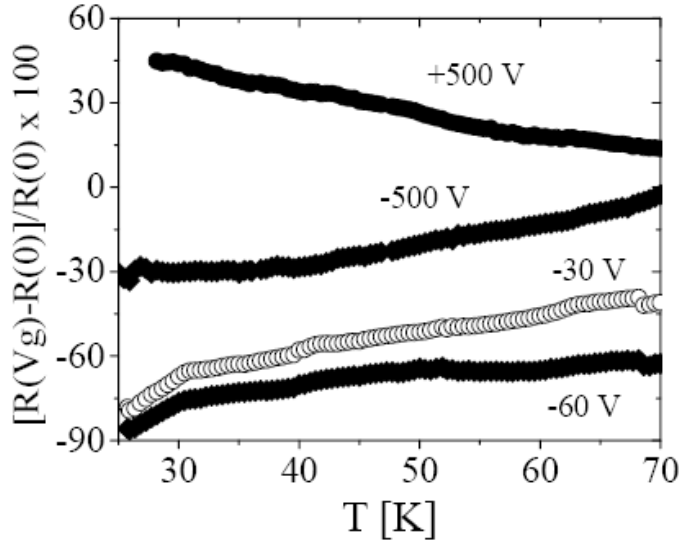


**Figure 67** Comparison between the per cent resistance variations observed in case of up-gated and back-gated field effect devices with an 8u.c. channel.

On a 8u.c. thick sample the role played by the flowing current value was studied. In

Figure 68(a) the resistance values obtained at 5 K are reported as a function of  $V_g$ . The measurements are performed for different  $I_{DS}$  values ranging from 5 nA to 200 nA. Even if the absolute values of the channel resistance are very different for different currents, the curves roughly overlap if normalized at the zero gate resistance value (

Figure 68(b)) and show an almost symmetric behaviour respect to positive or negative applied gate voltages. These normalized values present a strong modulation for  $|V_g| < 200$  V followed by an almost linear dependence. This dependence is more clear in

Figure 68(c) where the derivative of the curves are shown. For clarity only the curves obtained with the higher  $I_{ds}$  current values are shown. It should be stressed, however, that the observed behaviour is the same for  $I=5$ nA and  $I=10$ nA. They present a Gaussian like shape, showing a saturation effects at higher gate voltages for both positive and negative values. It's worth to notice that these curves are not symmetric in respect to the  $V_g=0$  V, but they present maximums for negative voltages ( $V_{gmax} = -40$ V for  $I=100$  nA,  $V_{gmax} = -50$  V for  $I=200$  nA). This maximum represents the gate voltage for which the effect is more evident, i.e. is more efficient in modulating the film behaviour. It should be observed that a similar asymmetric behaviour respect to the zero value is also reported in ref [7] in the analysis of the field effect device capacitance as a function of the applied gate voltage and is ascribed to a built-in polarization of the STO substrate.

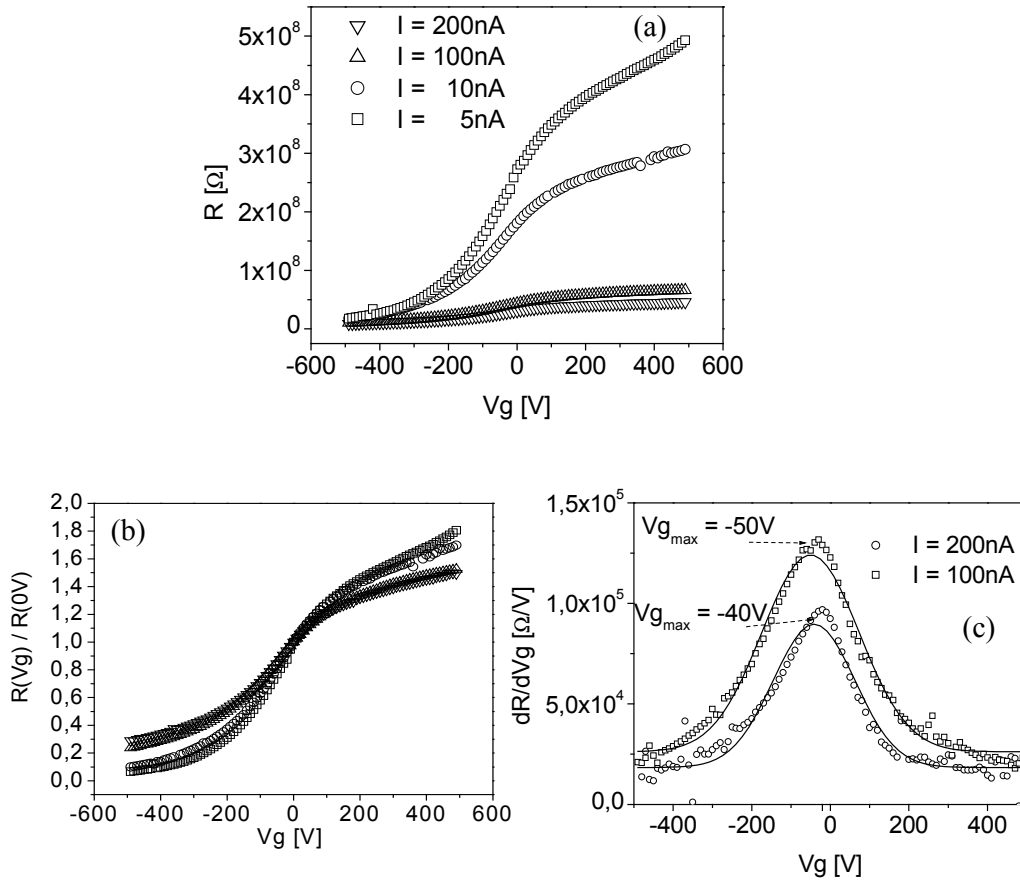


**Figure 68** (a) Resistance measured at 5 K for different  $I$  values as a function of the gate voltage in back-gate configuration on a 8 u.c film; (b) resistance values normalized to the  $V_g=0$  values for the corresponding  $I$  values; (c) derivative of the resistance measurements reported in (a) for two different  $I$ s values.

Finally, it's worth mentioning that in only one 8u.c. sample a field effect induced insulator-superconductor transition was observed, as reported in Figure 69. This result was obtained applying the gate voltage across the  $Al_2O_3$  layer. The four probe technique was used. As in the case of the other measured 8 u.c. FET, the field effect is negligible at temperature higher than 50 K and low gate voltages. At  $V_g=30$  V a resistive drop is observed at  $T=13.6$  K, but below 10 K the resistance increases again. By applying a gate voltage of 34 V a complete superconducting transition with  $T_c=18$  K is obtained. A transition to the insulating state is reversibly obtained by switching off the gate voltage. Interestingly, the transition observed at  $V_g = -34V$  occurred when the normal state resistance value was lower than the quantum resistance  $R_Q = h/4e^2 = 6,45k\Omega$ , as also reported in Figure 69(b). The occurrence of the electric field induced superconducting transition appears to be

very critical and was not observed in other nominally equivalent 8 u.c. devices possibly due to a slight degradation of the surface layer which avoids the formation of a superconducting path.

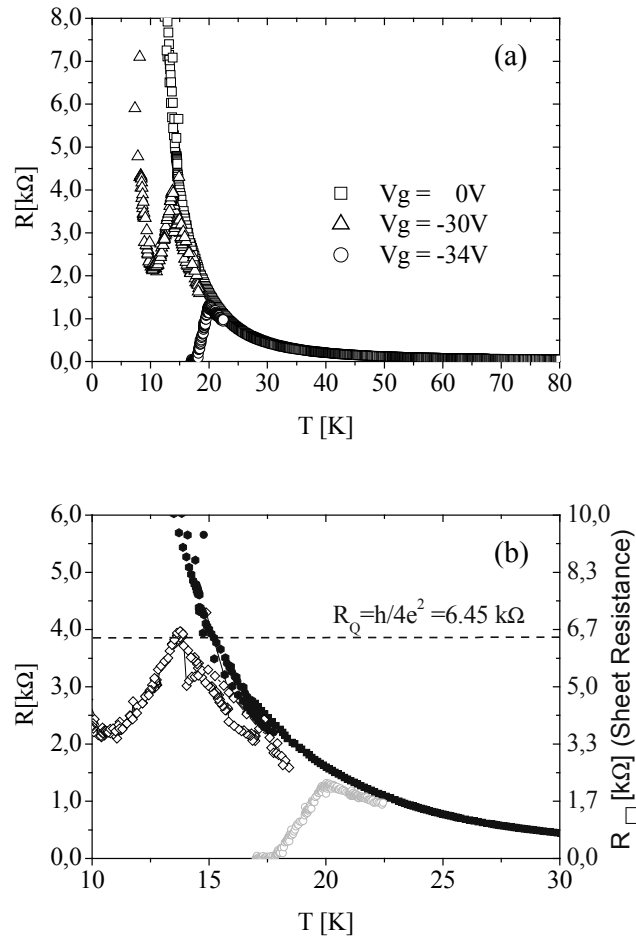


**Figure 69** field effect induced insulator-superconductor transition on a 8u.c. thick NBCO channel: (a)  $R(T)$  data and (b) sheet resistance values compared with the quantum resistance

In insulating NBCO channels, i.e. on 4 and 8 u.c. thin films, the field effect doping was also verified on the IV curves.

On 4u.c. thick channels, because of the high resistance values these devices presented at low temperature, the IV curves were carried out at room temperature applying the gate voltage across the  $\text{Al}_2\text{O}_3$  layer. In this case the curves were obtained applying an increasing voltage between the internal gold contacts and measuring the resulting flowing current by the picoammeter. The gate voltage was applied by the source-meter. The obtained results are reported in Figure 70. No relevant effect is observable until the drain-source voltages is less than about 30V and in addition a light

effect is only visible for a negative applied gate voltage of  $-10\text{V}$ , while  $V_g = 10\text{V}$  doesn't affect the IV behaviour of the sample.

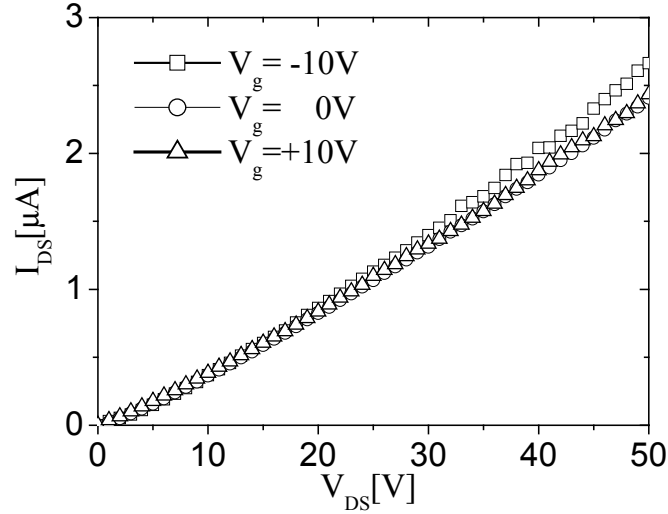


**Figure 70** Field effect on IV curves on a 4 u.c. thick film at room temperature in the up-gated configuration

The same kind of measurements, in the same configuration and with the same instrumental arrangement, were performed even on an 8u.c. thick sample (Figure 71). Here an evident asymmetry in the device responses for positive and negative applied gate voltages was observed too. But in this case a greater effect is visible even at  $V_{ds} = 50\text{V}$ .

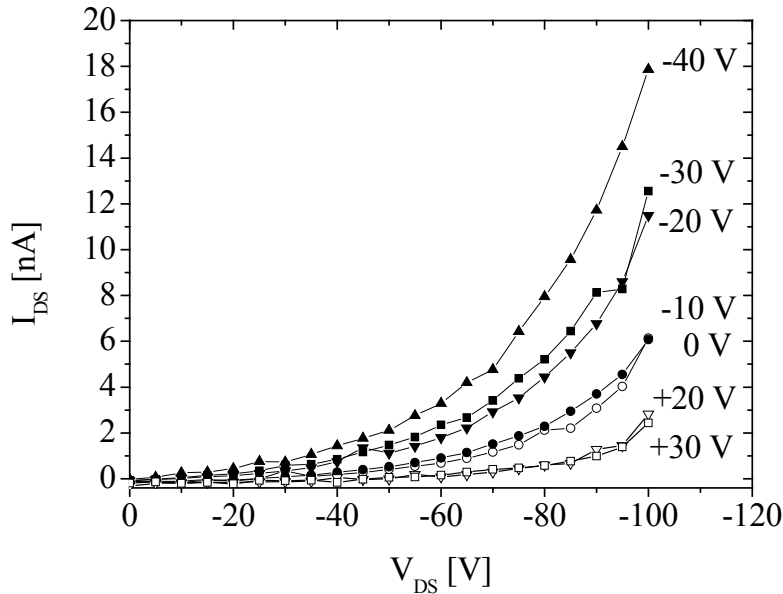


**Figure 71** Field effect on IV curves on an 8 u.c. thick film at room temperature in the up-gated configuration

The effect of the electrostatic doping on the IV curves in an 8u.c. thick channel was also observed at low temperature (5K) exploiting the back-gated configuration, i.e applying the gate voltage across the STO substrate. In this case a 100 $\mu$ m thick crystal was used as substrate and the experiments were performed by injecting an increasing current within the channel, provided by the source-meter, and measuring the resulting voltage drop between the voltage contacts. The curves obtained for  $V_g = 490V, 0V, -490V$  are reported in Figure 72.

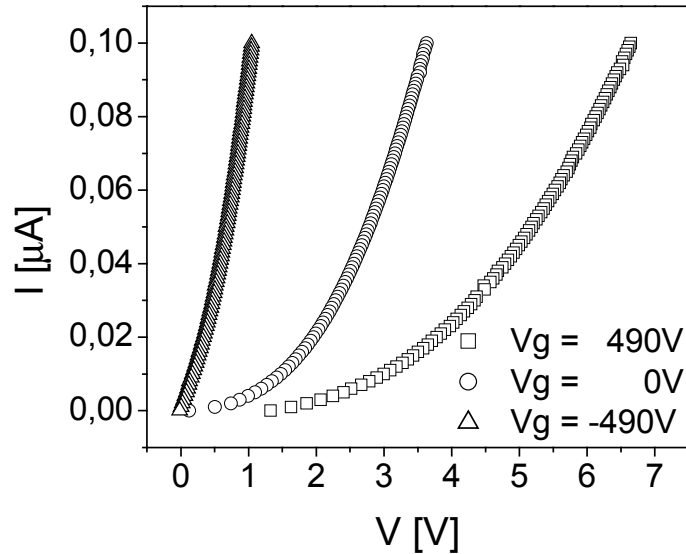


**Figure 72** IV curves for different applied gate voltages at low temperature on an 8u.c. NBCO thin channel in the back-gate configuration

#### 4.4. Conclusions

In this chapter the results of field effect experiments on high quality NBCO thin films were reported. The devices realised allowed the gate voltages could be applied across both a thin  $Al_2O_3$  layer deposited on the films and the STO crystal employed as substrate. Thanks to the completely in-situ deposition technique used no surface degradation affected the thin films transport properties. The realised arrangement of the instrumental apparatus available in Naples allowed to study the electrostatic doping of both superconducting and insulating NBCO thin films transport features. Substantial effects were observed on insulating samples, reaching a maximum modulation of the low temperature resistance on the order of 150% on 4u.c. thin films, whereas no relevant effect was observed on 10u.c. thick superconducting samples. In only

one case, even an induced insulator-superconductor transition was observed on an 8u.c. thick channel. The role of the channel current on the field-effect modulation was studied too, revealing an almost identical relative variation of the resistance for different current values. The effect of the electrostatic doping on room temperature IV curves was also investigated in insulating channels, yet in both the possible configuration. On 8u.c. thick samples, the low temperature IV behaviour was also studied. All the performed experiments results, both on R(T) curves and on IV curves, reveal an asymmetry in the channels response for positive or negative voltages, that can be ascribed to built-in charge of the dielectric materials.

## Conclusions

In this work the results of field effect experiments on superconducting thin films have been presented. The attention was focused on two different materials, reduced STO surfaces and underdoped NBCO thin films, both of them characterized by a strong dependence of their electronic transport behaviour on the charge carrier concentration.

The reduced STO surfaces were obtained by employing a new technique, consisting in a hydrogen plasma reduction procedure. By this mean, the oxygen content of a STO crystal surface was modified, i.e. an  $\text{STO}_{3-\delta}$  thin layer was created on its surface. The transport properties of such layers were studied in terms of resistance vs. temperature behaviour, magnetoresistance and Hall effect. The samples all showed a typical metallic behaviour as expected and magnetoresistance measurements showed a relevant effect at low temperature. Unfortunately, the actual thickness of the doped region was a priori unknown, hence resistivity and Hall effect data were available only in a thickness normalised way. Indeed, the carrier mobility was evaluated by combining the resistance and Hall effect results and exploiting an experimental relationship between carrier mobility and carrier density found for thermally reduced samples, the latter could be evaluated. Then, employing the Hall effect collected data, an estimation of the average thickness of the doped layer was carried out. The obtained layer thickness are always less than 100nm. Obtained Hall coefficients are in good quantitative agreement with those reported in literature for thermally reduced samples. Unfortunately, the obtained reduced regions show an increasing of the resistance as long as time flows, probably due to the diffusion of the introduced oxygen vacancies toward the STO substrate.

Exploiting the dielectric properties of the undoped STO substrates, field effect experiments were performed on this very thin metallic layer at low temperature. A great resistance modulation, with a maximum of about 300%, was observed. But a sort of saturation effect at the beginning of each measurement suggest a non trivial role of the introduced oxygen vacancies in determining the response of the system under test to the field effect. In order to verify the actual carrier concentration modulation, Hall effect and field effect measurements were performed simultaneously. The data were analysed following the same approach mentioned above. Surprisingly the results showed an increasing of the mobility, but a decreasing of the carrier concentration for positive applied gate voltages, i.e. for decreasing resistance values, and viceversa. Either the complex role of the oxygen vacancies distribution, whose profile is unknown, or the attempt to analyse this material by a simple single band metal model was at the origin of this artefact is still unclear.

Underdoped NBCO very thin films were studied by field effect too. Exploiting the dependence of the electronic transport on the films thickness these thin films have shown, both insulating and superconducting samples were studied. The former has been possible thanks to an instrumentation set up designed for this purpose. Almost no effect was observed in the superconducting case where only a few per cent normal state resistance modulation was achieved. Indeed, in insulating samples a maximum resistance variation of about 150% was observed in a 4u.c. thick film by employing a thin  $\text{Al}_2\text{O}_3$  layer as gate insulator. The combination of both the reduced thickness and the consequent reduced carrier density this compound present take count of the great effect observed. Moreover, in only one 8u.c. sample a field effect induced insulator-superconductor transition was observed. The role of the transverse applied field on IV curves was studied too, but no saturation was observed. The role of the measure current in field effect experiments was also investigated, but the same resistive relative modulated changes have been found. Finally, simultaneous Hall effect and field effect measurements were performed on few samples. Even if the modulating effect achieved seems to be related to the variation of the carrier concentration, the measurements are affected by a great uncertainty due to instrumental set-up employed, which was not conceived for measurements on high resistivity samples.



## References

---

- [1] Tokura, *Correlated electrons: science to technology*, JSAP International, No. 2, 2000
- [2] E. Dagotto, *Complexity in Strongly Correlated Electronic Systems*, Science, vol. 309, pag. 257, 2005
- [3] <http://www.ims.tnw.utwente.nl/thiox/science/>
- [4] <http://www.motorola.com>
- [5] I. H. Inoue, *Electrostatic carrier doping to perovskite transition-metal oxides*, Semic. Sc. and Tec., vol. 20, pag. S112, 2005
- [6] C. H. Ahn, K. M. Rabe and J.-M. Triscone, *Ferroelectricity at the Nanoscale: Local Polarization in Oxide Thin Films and Heterostructures*, Science, vol. 303, pag. 488 (2004)
- [7] M. Dawber, K.M. Rabe and J.F. Scott, *Physics of thin-film ferroelectric oxides*
- [8] M. B. Salamon and M. Jaime, *The physics of manganites: Structure and transport*, Rev. Mod. Phys., Vol. 73, pag. 583, 2001
- [9] S. A. Wolf, D. D. Awschalom, R. A. Buhrman, J. M. Daughton, S. von Molna, M. L. Roukes, A. Y. Chtchelkanova, D. M. Treger, *Spintronics: A Spin-Based Electronics Vision for the Future*, Science, vol. 294 pag 1488, 2001
- [10] N. Hur, S. Park, P. A. Sharma, J. S. Ahn, S. Guha & S-W. Cheong, *Electric polarization reversal and memory in a multiferroic material induced by magnetic fields*, Nature, vol.429, pag.392, 2004
- [11] J. Mannhart, *High-Tc transistors*, Sup. Sci. Technol., vol. 9, pag. 49, 1996
- [12] N. Mott, *Metal-Insulator Transitions* (Taylor and Francis, London, 1990).
- [13] D. M. Newns, J. A. Misewich, C. C. Tsuei, A. Gupta, B. A. Scott and A. Schrott, *Mott transition field effect transistor*, Appl. Phys. Lett., vol. 73, pag. 780, 1998
- [14] A. Bhattacharya, M. Eblen-Zayas, N. E. Staley, W. H. Huber and A. M. Goldman, *Micromachined SrTiO<sub>3</sub> single crystals as dielectrics for electrostatic doping of thin films*, Appl. Phys. Lett., vol. 85, pag. 997, 2004
- [15] C. H. Ahn, J.-M. Triscone and J. Mannhart, *Electric field effect in correlated oxide systems*, Nature, vol. 424, pag. 1015, 2003
- [16] C. H. Ahn, S. Gariglio, P. Paruch, T. Tybell, L. Antognazza, J.-M. Triscone, *Electrostatic Modulation of Superconductivity in Ultrathin GdBa<sub>2</sub>Cu<sub>3</sub>O<sub>7-x</sub> Films*, Science, vol. 284, pag. 1152, 1999
- [17] R. E. Glover and M. D. Sherrill, Phys. Rev. Lett., vol. 5, pag. 248, 1960

- 
- [18] J. Mannhart *et al.*, Phys. Rev. Lett., vol. **67**, pag. 2099, 1991
- [19] X. X. Xi *et al.*, Phys. Rev. Lett., vol. 68, pag.1240, 1992
- [20] T. Frey, J. Mannhart, J. G. Bdnorz and E. J. Williams, *Mechanism of the electric field effect in the high-Tc cuprates*, Phys. Rev. B, vol. 51, pag. 3257, 1995
- [21] D. Matthey, S. Gariglio, C. H. Ahn and J.-M Triscone, *Electrostatic modulation of the superconducting transition in thin NdBa<sub>2</sub>Cu<sub>3</sub>O<sub>7-d</sub> films: The role of classical fluctuations*, Physica C, vol. 372, pag. 583, 2002
- [22] K. A. Parendo, K. H. Sarwa, B. Tan, A. Bhattacharya, M. Eblen-Zayas, N. E. Staley, and A. M. Goldman, *Electrostatic Tuning of the Superconductor-Insulator Transition in Two Dimensions*, Phys. Rev. Lett., Vol. 94, 197004 (2005)
- [23] S. Gariglio, C. H. Ahn, D. Matthey and J.-M. Triscone, *Electrostatic Tuning of the Hole Density in NdBa<sub>2</sub>Cu<sub>3</sub>O<sub>7.2d</sub> Films and its Effect on the Hall Response*, Phys. Rev. Lett., vol.88, 067002, 2002
- [24] N. Shanthi and D. D. Sarma, *Electronic structure of electron doped SrTiO<sub>3</sub>: SrTiO<sub>3</sub>- $\delta$  and Sr<sub>1-x</sub>LaxTiO<sub>3</sub>*, Phys. Rev. B, vol. 57, pag. 2153, 1998
- [25] K. A. Muller and H. Burkard, Phys. Rev. B, vol. 19, pag. 3593, 1979
- [26] M. A. Saifi and L. E. Cross, *Dielectric properties of strontium titanate at low temperature*, Phys. Rev. B, vol. 2, pag. 677 , 1970
- [27] H.-M. Christen, J. Mannhart, E. J. Williams and Ch. Gerber, *Dielectric properties os sputtered SrTiO<sub>3</sub> films*, Phys. Rev. B, vol. 49, pag 12095, 1994
- [28] D. Fuchs, C. W. Schneider, R. Schneider and H. Rietschel, *High dielectric constant and tunability of epitaxial SrTiO<sub>3</sub> thin film capacitors*, Journ. Of Appl. Phys., vol. 85, pag. 7362, 1999
- [29] A. Battacharya, M. Ebleden-Zayas, N. E. Staley, W. H. Huber and A. M. Goldman, *Micromachined SrTiO<sub>3</sub> single crystals as dielectric for electrostatic doping of thin films*, Appl. Phys. Lett., vol. 85, pag. 997, 2004
- [30] K. Nakajima, K. Yokota, H. Myoren, J. Che and T. Yamashita, Appl. Phys. Lett., vol. 63, pag. 684, 1993
- [31] D. Matthey, S. Gariglio and J.-M. Triscone, *Field-effect experiments in NdBa<sub>2</sub>Cu<sub>3</sub>O<sub>7-d</sub> ultrathin films using a SrTiO<sub>3</sub> single-crystal gate insulator*, Appl. Phys. Lett., vol. 83, pag. 3758, 2003
- [32] K. Szot, W. Speier, R. Carius, U. Zastrow and W. Beyer, *Localized metallic conductivity and self-healing during thermal reduction of SrTiO<sub>3</sub>*, Phys. Rev. Lett., vol. 88, pag. 075508, 2002

- 
- [33] C. Lee, J. Destry and J. Brebner, *Optical absorption and transport in semiconducting SrTiO<sub>3</sub>*, Phys. Rev. B, vol. 11, pag 2299, 1975
- [34] H. P. R. Frederikse, W. R. Hosler and W. R. Thurber, Phys. Rev. , vol. 143, pag. 648, 1966
- [35] O. N. Tufte and P. W. Chapman, *Electron mobility in semiconducting strontium titanate*, Phys. Rev., vol. 155, pag. 796, 1967
- [36] J. F. Schooley, W. R. Hosler and M. L. Cohen, *Superconductivity in semiconducting SrTiO<sub>3</sub>*, Phys. Rev. Lett., vol. 12, pag. 474, 1964
- [37] J. F. Schooley, W. R. Hosler, E. Ambler, J. H. Becker, M. L. Cohen and C. S. Koonce, *Dependence of the superconducting transition temperature on carrier concentration in semiconducting SrTiO<sub>3</sub>*, Phys. Rev. Lett., vol. 14, pag. 305, 1965
- [38] C. S. Koonce, M. L. Cohen, J. F. Schooley, W. R. Hosler and E. R. Pfeiffer, *Superconducting transition temperatures of semiconducting SrTiO<sub>3</sub>*, Phys. Rev., vol. 163, pag. 380, 1967
- [39] K. Szot and W. Speier, *Surfaces of reduced and oxidized SrTiO<sub>3</sub> from atomic force microscopy*, Phys. Rev. B, vol. 60, pag. 5909, 1999
- [40] Arciprete, Appl. Phys. Lett. 71, 959 (1997)
- [41] C. Ahn et al, Nature
- [42] Kabasawa et al, J Appl. Phys. **79** 7849 (1996)
- [43] N. Korner, E. Beck, A. Dommann, N. Onda and J. Ramm, *Hydrogen plasma chemical cleaning of metallic substrates and silicon wafers*, Surf. and Coat. Tech., vol. 76, pag. 731, 1995
- [44] J. F. Scott, S. A. T. Redfern, Ming Zhang and M. Dawber, *Polarons, oxygen vacancies and hydrogen in Ba<sub>x</sub>Sr<sub>1-x</sub>TiO<sub>3</sub>*, J. of European Ceram. Soc., vol. 21, pag 1629, 2001
- [45] K. Szot and W. Speier, *Surfaces of reduced and oxidized SrTiO<sub>3</sub> from atomic force microscopy*, Phys. Rev. B, vol. 60, pag. 5909, 1999
- [46] K. S. Takahashi, D. Matthey, D. Jaccard and J.-M. Triscone, *Transport properties of reduced SrTiO<sub>3</sub> single crystal "thin films"*, Ann. Phys., vol. 13, pag. 68, 2004
- [47] O. N. Tufte and P. W. Chapman, *Electron mobility in semiconducting strontium titanate*, Phys. Rev., vol. 155, pag. 796, 1967
- [48] C. Lee, J. Destry and J. L. Brebner, *Optical absorption and transport in semiconducting SrTiO<sub>3</sub>*, Phys. Rev. B, vol. 11, pag. 2299, 1975
- [49] H. P. R. Frederikse, W. R. Hosler and W. R. Thurber, *Magnetoresistance of semiconducting SrTiO<sub>3</sub>*, Phys. Rev., vol. 143, pag. 648, 1966
- [50] C. S. Koonce, M. L. Cohen, J. F. Schooley, W. R. Hosler and E. R. Pfeiffer, *Superconducting transition temperatures of semiconducting SrTiO<sub>3</sub>*, Phys. Rev., vol. 163, pag. 380, 1967

- 
- [51] N. Shanthi and D. D. Sarma, *Electronic structure of electron doped SrTiO<sub>3</sub>: SrTiO<sub>3</sub>- $\delta$  and Sr<sub>1-x</sub>LaxTiO<sub>3</sub>*, Phys. Rev. B, vol. 57, pag. 2153, 1998
- [52] M. A. Saifi and L. E. Cross, *Dielectric properties of strontium titanate at low temperature*, Phys. Rev. B, vol. 2, pag. 677, 1970
- 53 Kharrazi Olsson M., Macak K., Helmersson U., Hjörvarsson B., High-rate reactive dc magnetron sputter deposition of Al<sub>2</sub>O<sub>3</sub> films, J. Vac. Sci. Technol. A16, 639-643 (1998)
- 54 D. Matthey, S. Gariglio, and J.-M. Triscone Field-effect experiments in NdBa<sub>2</sub>Cu<sub>3</sub>O<sub>7</sub>- $\delta$  ultrathin films using a SrTiO<sub>3</sub> single-crystal gate insulator, Appl. Phys. Lett. vol. 83, pag. 3758, 2003
- 55 M. R. Mohammadzadeh and M. Akhavan, Eur. Phys. J. B **33**, 381 (2003)